Effect of the nature of nanoparticles on the photophysicochemical properties and photodynamic antimicrobial chemotherapy of phthalocyanines

A thesis submitted in fulfilment of the requirements for the degree of

Master Of Science

Of

RHODES UNIVERSITY

By

Aviwe Magadla

February 2019

ACKNOWLEDGEMENTS

My sincere and wholehearted appreciation to my supervisor, **Prof. Nyokong**. Thank you so much for your patience, guidance and the opportunity to work in your research lab. I would like to thank Dr Mack, Dr Britton, Ms. Gail and Papa Francis for their assistance throughout my studies. To my family, thank you for your prayers and being there, you've been an ever present source of joy and support.

I would like to thank the past and present members of S22 research group, especially Drs David and Edward thank you for your assistance in running my experiments and your support. I also acknowledge financial support National Research Foundation (NRF), Chemistry Department of Rhodes University, all staff members and all the postgraduate students.

ABSTRACT

In this work, the syntheses and characterisation of Zn monocaffeic acid tri–*tert*–butyl phthalocyanine (**1**), Zn monocarboxyphenoxy tri–*tert*–butylphenoxyl phthalocyanine (**2**), tetrakis phenoxy *N,N*-dimethyl-4-(methylimino) phthalocyanine indium (III) chloride (**3**) and tetrakis *N,N*-dimethyl-4-(methylimino) phthalocyanine indium (III) chloride (**5**) are presented. Complexes **3** and **5** were further quartenised with 1,3-propanesultone to form corresponding complexes (**4**) and (**6**), respectively. Complexes **1** and **2** were covalently linked to amino functionalised nanoparticles (NPs). Complexes **3**, **4**, **5** and **6** where linked to oleic acid/oleylamine capped (OLA/OLM) silver-iron dimers (Ag-Fe_3O_4 OLA/OLM) and silver-iron core shell (Ag@Fe_3O_4 OLA/OLM) NPs via interaction between the nanoparticles and the imino group on the phthalocyanines. The phthalocyanine-NP conjugates afforded an increase in triplet quantum yields with a corresponding decrease in fluorescence quantum yield as compared to the phthalocyanine complexes alone. Complexes **3**, **4** and their conjugates were then used for photodynamic antimicrobial chemotherapy on *E. coli*. The zwitterionic photosensitiser **4** and its conjugates showed better efficiency for photodynamic antimicrobial chemotherapy compared to their neutral counterparts.

TABLE OF CONTENTS

LIST OF ABBREVIATIONS

ADMA	**Tetrasodium α,α–(anthracene–9,10–diyl) dimethylmalonate**
APTES	**3–Aminopropyl triethoxysilane**
CFU	**Colony Forming Unit**
DBU	**1,8–Diazabicyclo–[5.4.0]–undec–7–ene**
DCC	**Dicyclohexylcarbodiimide**
DMAP	**Dimethylaminopyridine**
DMF	**Dimethylformamide**
DMSO	**Dimethyl Sulfoxide**
DMSO-d_6	**Deuterated Dimethylsulfoxide**
DPBF	**1,3–Diphenylisobenzofuran**
DPE	**Diphenyl Ether**
ET	**Energy Transfer**
EPR	**Enhanced Permeability and Retention**
FT–IR	**Fourier Transform Infrared**
GSH	**Glutathione**
HOMO	**Highest Occupied Molecular Orbital**
IC	**Internal Conversion**
ISC	**Intersystem Crossing**
LUMO	**Lowest Unoccupied Molecular Orbital**
MALDI	**Matrix–Assisted Laser Desorption/Ionization**
MNPs	**Magnetic Nanoparticles**
MPA	**Mercaptopropionic Acid**

MPcs	**Metallophthalocyanines**
MS	**Mass Spectrometer**
Nd–YAG	**Neodymium–doped Yttrium Aluminium Garnet**
NLO	**Nonlinear Optics**
NPs	**Nanoparticles**
OLA	**Oleic Acid**
OLM	**Oleylamine**
PACT	**Photodynamic Antimicrobial Chemotherapy**
PBS	**Phosphate-buffered saline**
Pcs	**Phthalocyanines**
PDT	**Photodynamic Therapy**
PET	**Photo-induced Energy Transfer**
P	**Phosphorescence**
^{1}H NMR	**Proton Nuclear Magnetic Resonance**
ROS	**Reactive Oxygen Species**
RT	**Room temperature**
SiNPs	**Silica Nanoparticles**
SubPc	**Subphthalocyanine**
TCSPC	**Time Correlated Single Photon Counting**
TEM	**Transmission Electron Microscope**
TEOS	**Tetraethyl orthosilicate**
UV–Vis	**Ultraviolet–Visible**
XRD	**X–ray Diffractometer**

LIST OF SYMBOLS

Φ_{Δ}	Singlet Oxygen Quantum Yield
Φ_{f}	Fluorescence Quantum Yield
Φ_{T}	Triplet Quantum Yield
$^{1}O_{2}$	Singlet Oxygen
$^{3}O_{2}$	Molecular Oxygen
S_{0}	Singlet ground state
S_{1}	Singlet excited state
T_{1}	Triplet excited state
β	Peripheral Position
τ_{F}	Fluorescence Lifetime
τ_{T}	Triplet Lifetime
α	Non–peripheral Position
ΔAS	Change in singlet state absorbance
ΔAT	Change in triplet state absorbance
A/abs	Absorbance

Chapter 1
Introduction

1. Introduction

Recent studies have shown that the conjugation of nanomaterial with photosensitisers (in this case, metallophthalocyanines (MPcs)) often affords improved photophysicochemical behaviour of the latter [1,2]. Enhanced photophysical properties of MPc in the nano composites are of importance in medical applications such as photodynamic therapy (PDT) and photodynamic antimicrobial chemotherapy (PACT) [3–6].

This thesis reports on the physicochemical properties and PACT activities of phthalocyanines in the presence of nanomaterials. Synopsis on their syntheses and applications are presented in the following subsections.

1.1 Nanoparticles

Materials in the nanometer range have been produced for several decades due to their interesting physicochemical characteristics which affords diverse applicability such as in medicine, photonics, fluorescence sensing, bioimaging and theranostics [7–10]. Of high importance among the nanomaterials that are often employed for different applications are the nanoparticles (NPs). NPs are materials that have a size dimension of 100 nm or less and have distinct characteristics. NPs are known for their applicability in PACT, PDT, drug delivery, bioimaging, nonlinear optics and catalysis [11–16] amongst many other applications. NPs have a large surface area and a flexible surface which can be modified with bifunctional ligands to ease their linkage with other molecules via covalent or non–covalent interaction [17–19]. In this work, the effects of NPs on the photophysicochemical properties and PACT activity of MPcs when in

conjugates are studied. The NPs employed in this work are silver nanoparticles (AgNPs), silver-iron oxide core shell NPs (Ag@Fe_3O_4), silver-iron oxide core shell passivated with silica NPs (Ag@Fe_3O_4-SiNPs), silver-iron dimer NPs (Ag-Fe_3O_4) and silica NPs (SiNPs). (Note: core shell is represented with "@" and dimer with "–"). These NPs will be discussed in the following subsections:

1.1.1 Silver NPs (AgNPs), silver-iron oxide core shell NPs (Ag@Fe_3O_4) and silver-iron oxide dimer NPs (Ag-Fe_3O_4).

AgNPs and Fe_3O_4 magnetic nanoparticles (MNPs) have been extensively used in diverse biomedical applications due to their unique characteristics in terms of physical, optical, electrical, chemical and magnetic properties [20,21]. AgNPs and Fe_3O_4 MNPs have been demonstrated to be efficient in drug delivery through enhanced permeability and retention effect (EPR). MNPs also possess magnetic properties and are an attractive platform as contrast agents for magnetic resonance imaging (MRI) [22–27]. AgNPs have also been used as antibacterial agents but this decreased with the discovery and popularity of antibiotics. However, the antibiotic-resistant pathogens have brought a revival in AgNPs-based medications [28,29]. AgNPs exhibit antimicrobial action against Gram-positive and Gram-negative bacteria; and fungi. Thus combining AgNPs with Pc (PACT agents) in this work will enhance PACT activity by synergistic effect [28–30]. MNPs have been reported to enhance the antibacterial activity of AgNPs hence the two are combined in this work [31,32]. The effects of AgNPs and MNPs when combined as core-shell or as dimers on the PACT activity and photophysics

of MPcs will be evaluated. Additionally, Ag and Fe_3O_4 based NPs were employed in view of the fact that they have the ability to promote spin orbit coupling (also known as heavy atom effect) which often encourages improved triplet state population, hence improved singlet oxygen generation [33,34]. High singlet oxygen production is essential for PACT activities. In this work the surfaces of the AgNPs and Ag@Fe_3O_4 were functionalised with glutathione (GSH) and represented as AgNPs-GSH and Ag@Fe_3O_4-GSH respectively, **Fig. 1.1 A, B** to enable the NH_2 moiety of the GSH capped NPs to link with the COOH substituted Pc via an amide bond formation. Ag@Fe_3O_4 and Ag-Fe_3O_4 were stabilised with oleic acid (OLA) and oleylamine (OLM) prior to phase transfer for the former (as shown in **Fig. 1.1 C** and **D**). Linkage of the Pcs to OLA/OLM capped NPs was carried out via metal (in this case, Ag) to sulfur or nitrogen interactions. The sulfur or nitrogen act as donors, while the Ag metal acts as an acceptor [35,36].

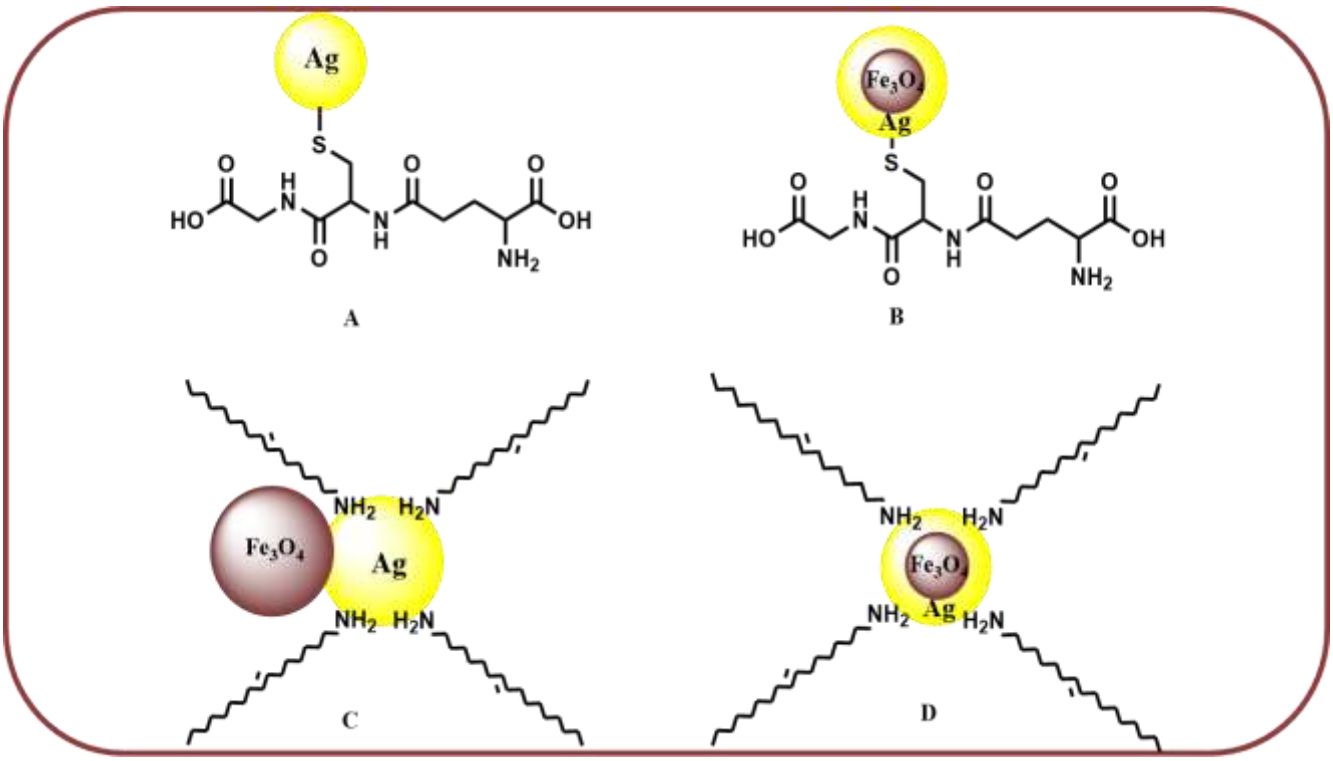

Figure 1.1: Representation AgNPs-GSH (A), Ag@Fe_3O_4-GSH (B), Ag-Fe_3O_4 OLA/OLM NPs (C) and Ag@Fe_3O_4 OLA/OLM NPs (D).

1.1.2 SiNPs and Ag@Fe_3O_4-SiNPs.

Silica nanoparticles (SiNPs) have found large-scale applications in various fields such as bioimaging, drug delivery, PACT/PDT and sensing amongst other applications [37–39]. SiNPs are favourable for biological applications owing to their excellent physicochemical properties, biocompatibility, low toxicity, thermal stability, facile synthetic route and the possibility of large-scale production [40]. Due to their porous interior and large surface area SiNPs can be used as reservoirs to encapsulate or link them with other

molecules to allow for passive targeting [41–43]. The tuneable mesoporous nature and modifiable surface of SiNPs enables encapsulation of other composites such as Ag@Fe_3O_4 to form Ag@Fe_3O_4-SiNPs employed in this thesis. This improves specificity, solubility and drug efficacy [37,39,44–46].

In this work, the effects of amino functionalised SiNPs and Ag@Fe_3O_4-SiNPs **Fig. 1.2** on the photophysicochemical behaviour of MPcs when conjugated, will be evaluated. The SiNPs-APTES and Ag@Fe_3O_4-SiNPs-APTES used were conjugated to a COOH substituted Pc via covalent linkage [47]. Thus Ag@Fe_3O_4 will be studied alone and when combined with SiNPs in Ag@Fe_3O_4-SiNPs-APTES for the effects on the photophysicochemical parameters of MPcs.

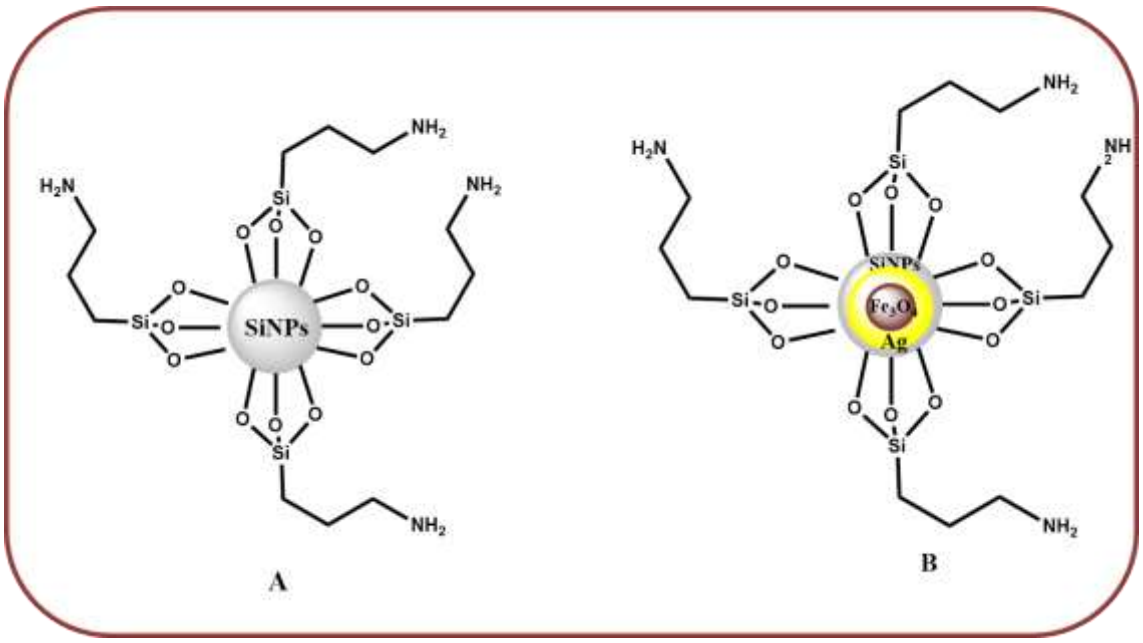

Figure 1.2: Representation of amino functionalised SiNPs-APTES (A) and Ag@Fe_3O_4-SiNPs-APTES (B).

1.2 Metallophthalocyanines (MPc)

MPcs are intense blue-green (depending on the absorption wavelength) synthetic pigments comprising of an 18π electron conjugated ring system [48–50]. The central cavity of phthalocyanines is capable of accommodating more than 70 metals and metalloids. Pcs possess D_{4h} geometry, while their unmetallated (H_2Pc) counterparts have D_{2h} symmetry as shown in **Fig. 1.3 A** and **B**, respectively. Pcs/MPcs have exceptional physical and chemical properties originating from their central metals, ring substituents either on the periphery (β) or the non-periphery (α) positions as shown in **Fig. 1.3A**. MPcs have found extensive use in PDT, PACT, electrocatalysis and nonlinear optics [51–55] amongst an array of other applications. MPcs can be modified to give either symmetrical or asymmetrical structures. In this research work, symmetrical, asymmetrical MPcs and their conjugates with NPs are employed.

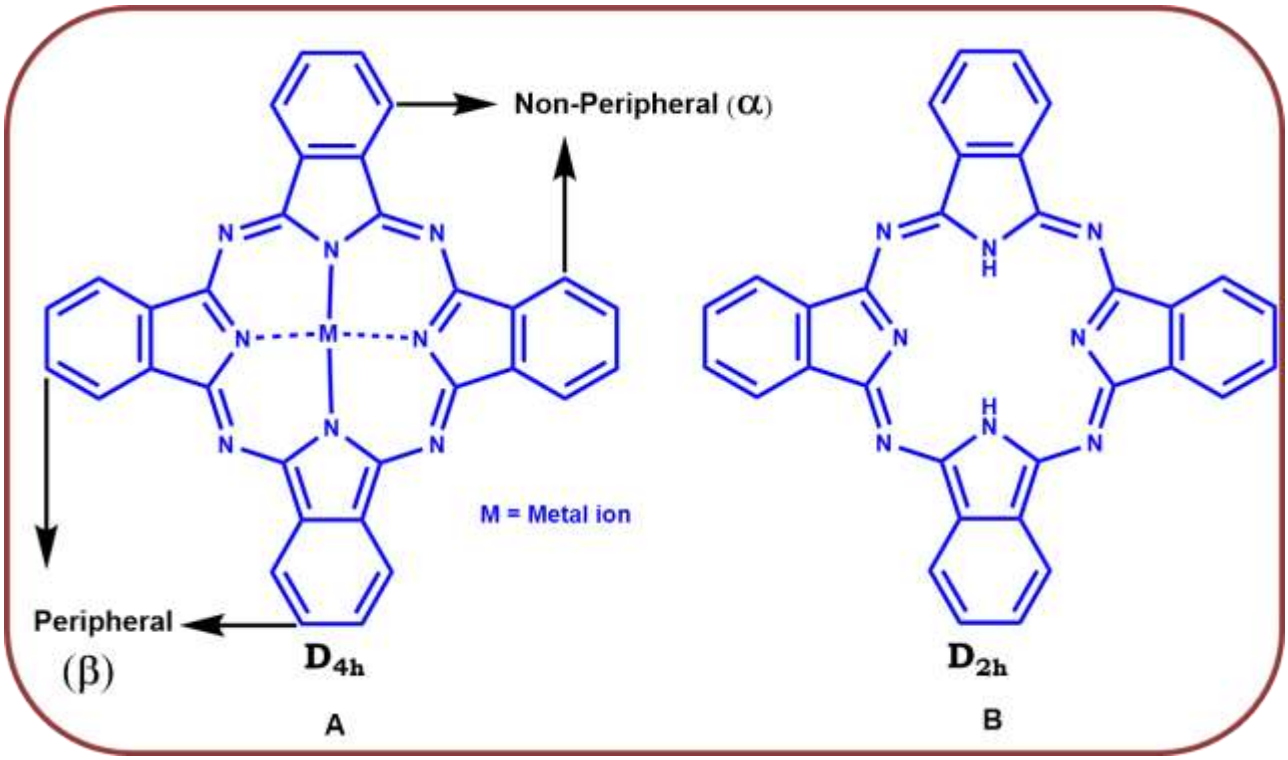

Figure 1.3: Molecular structure of Pc showing α- and β- positions with their geometrical confirmation: (A) MPc, D_{4h} and (B) H_2Pc, D_{2h}.

1.2.1 General synthesis of symmetrical and asymmetric phthalocyanines

Several methods using different precursors as starting material have been developed for the synthesis of unsubstituted Pcs. This is generally achieved using cyclotetramerization reaction of phthalonitrile, 1, 3-diimino isoindol, phthalamide, phthalic anhydride, o-dibromobenzene or o-cyanobenzamide derivatives in high-boiling solvents in the presence of strong base such 1,8-diazabicyclo[5.4.0]undec-7-ene (DBU), with or without a metal salt (MX) as shown in **Scheme 1.1** [53,56]. However, there are disadvantages associated with unsubstituted Pcs such as the lack of applicability where specific binding or coordination with other molecules is required.

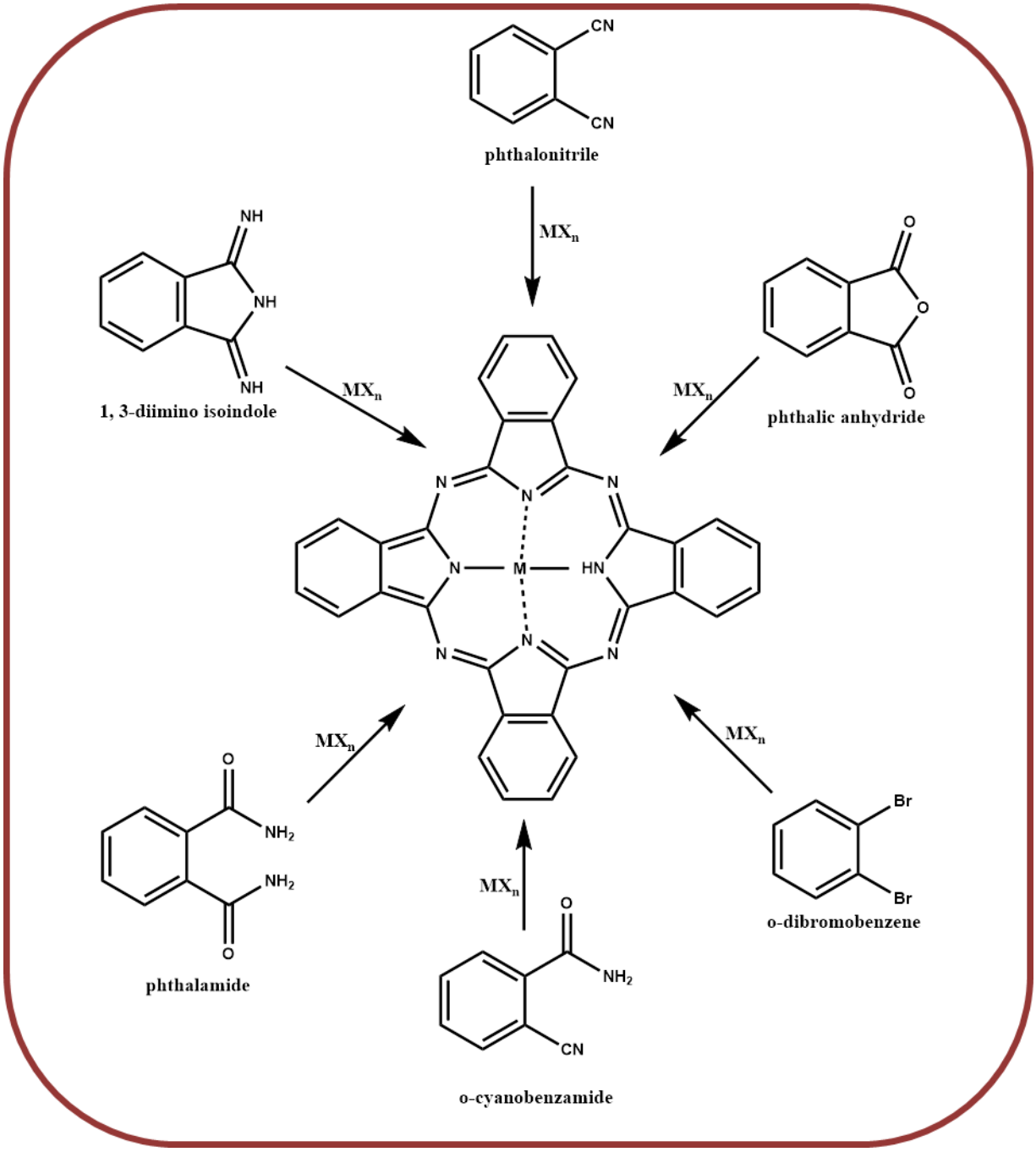

Scheme 1.1: Synthesis of Phthalocyanines from different precursors.

Phthalonitrile is the most commonly used out of the aforementioned precursors, this is because phthalonitriles allow for milder reaction conditions and they afford facile and good yield with high purity [57]. For the synthesis of symmetrically ring tetra substituted Pcs, substituted phthalonitriles are used **Scheme 1.2**.

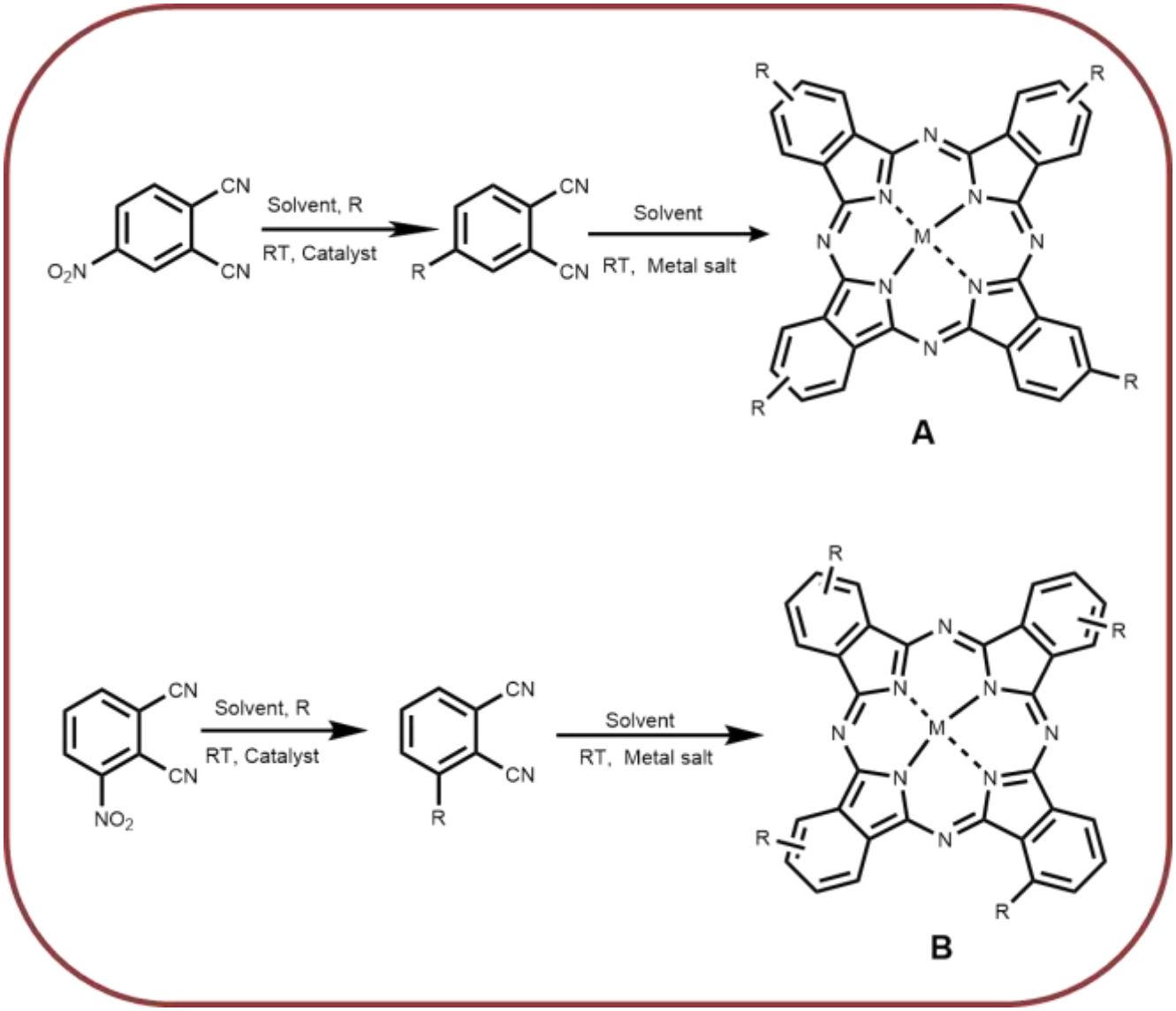

Scheme 1.2: Syntheses of peripheral A and non-peripheral B tetra substituted MPcs from a mono-substituted phthalonitrile. R = substituents, RT = Room temperature.

Asymmetric Pcs such as A_3B are largely synthesised using any of these approaches; subphthalocyanine (SubPc) ring expansion reaction, polymer supports or the use of two different phthalonitrile precursors as shown in **Scheme 1.3**. The latter method upon cyclization gives a mixture of six possible compounds [58,59]. In order to minimise the formation of the undesired by–products such as A_2B_2, AB_3, A_4 and B_4 ratios such as 3:1 (A to B) or higher ratios such as 9:1 (A to B) have been recommended and successfully used by several research groups. Separation of the compound of interest which is A_3B from the mixtures can be achieved by using extensive chromatography [60–62].

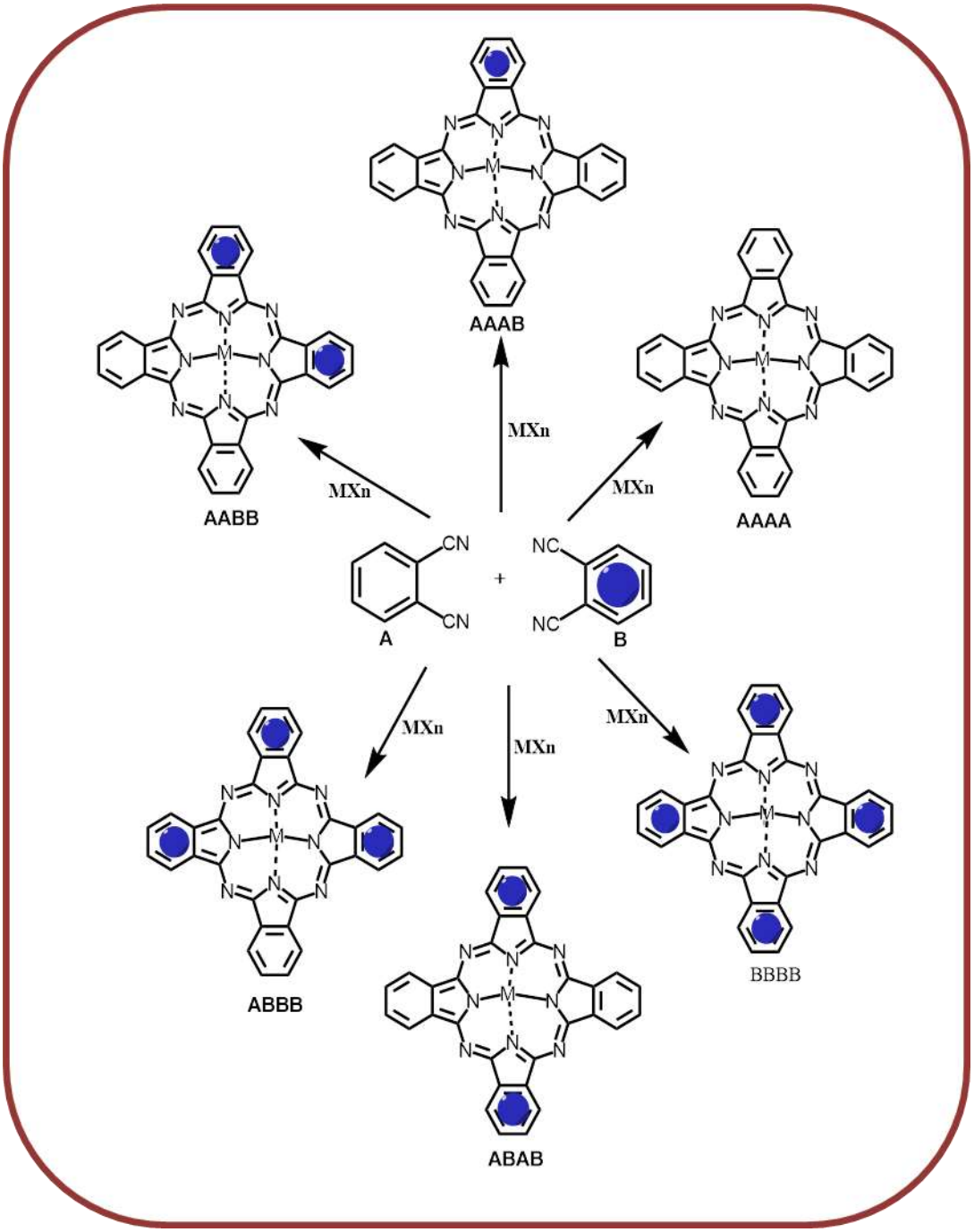

Scheme 1.3: Mixed synthesis of asymmetrical MPcs by the statistical condensation method.

1.2.2 MPcs employed as photosensitizers in this work

This work reports on the use of symmetrical and asymmetric phthalocyanines as photosensitisers for PACT. **Table 1.1** shows some examples of Pcs which have been linked to NPs of interest in this work [63–71].

Table 1.1: Examples of Pcs and their conjugates and their applications

Molecular structure	Phthalocyanine	NPs and bond formed with Pc	Studies	Ref
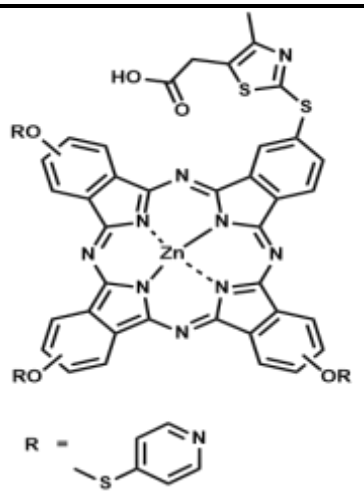	tris[(4-(pyridin-4-ylthio)-2-thio-4-methylthiazol-5-yl) acetic acid phthalocyaninato] zinc (II)	Linked to SiNPs via amide bond and doping	Photophysics	**[63]**
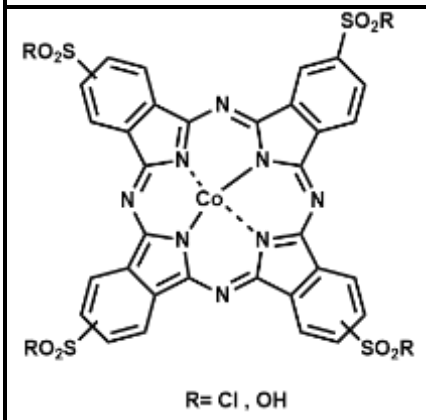	Sulfonated Co(II) phthalocyanine	Linked to Fe_3O_4-SiNPs via sulfonamide bond	Catalysis	**[64]**

Molecular structure	Phthalocyanine	NPs and bond formed with Pc	Studies	Ref
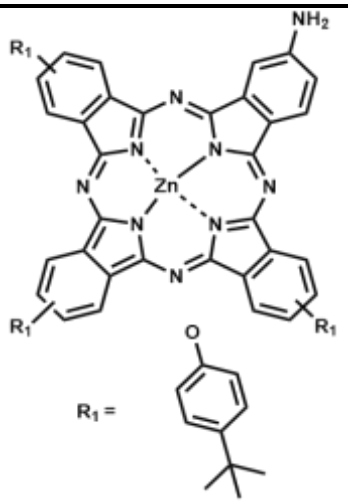	2-amino-9(10),16(17),23(24)-trikis-(4-tert-butylphenoxy) phthalocyaninato zinc(II)	Linked to Ag@ Fe_3O_4-MPA and Ag-Fe_3O_4-MPA via amide bond	Photophysics and Non Linear Optics	**[65]**
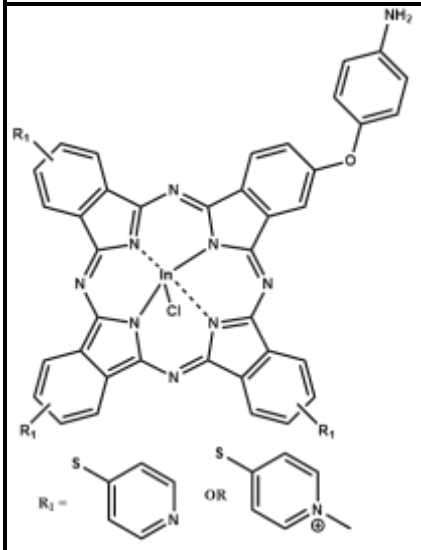	9(10),16(17),23(24)-Tri-4-pyridylsulfanyl-2(3)-(4-aminophenoxy) phthalocyaninato chloroindium(III) Cationic 9(10),16(17),23(24)-tri-N-methyl-4-pyridylsulfanyl-2(3)-(4-aminophenoxy)phthalocyaninato chloroindium(III) triiodide	Linked to Fe_3O_4@SiNPs-COOH via amide bond	Photophysics and PACT	**[66]**

Molecular structure	Phthalocyanine	NPs and bond formed with Pc	Studies	Ref
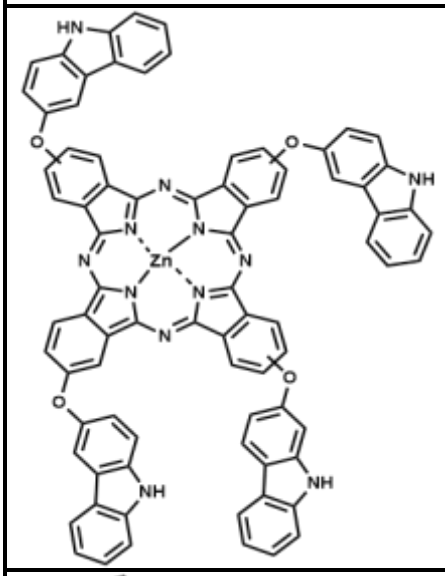	1,(4)-tetra(carbazol-2-yloxy)phthalocyaninato-zinc(II)	Linked to AgNPs via metal (Ag) to nitrogen	Photophysics and photo catalysis	**[67]**
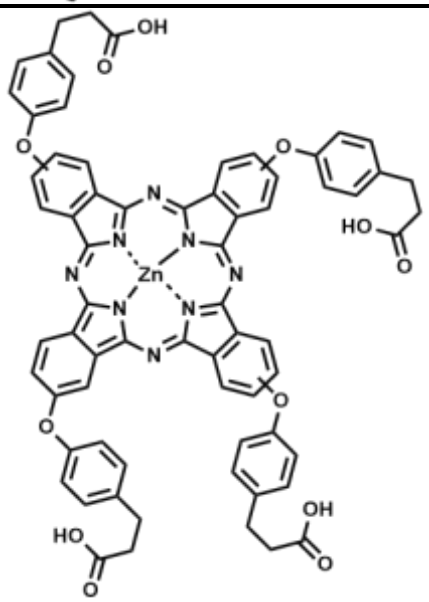	Zinc(II) tetra–[3–(4–phenoxy)(propanoic acid) phthalocyanine]	Linked to AgNPs and AgAu NPs via amide bond	Photophysics	**[68]**

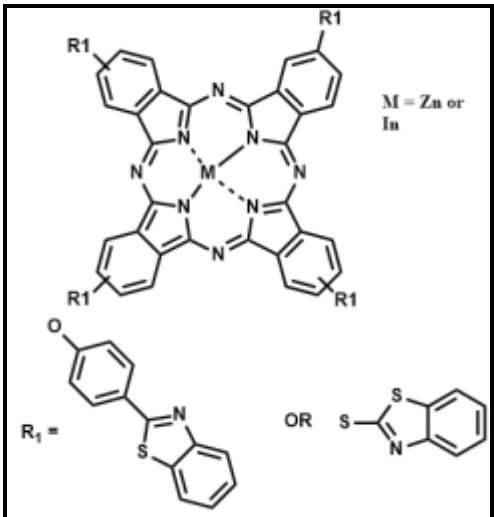	Tetrakis[(benzo[d]thiazol-2-ylphenoxy)phthalocyaninato] indium (III) chloride (1) and Tetrakis[(benzo[d]thiazol-2-ylthio)phthalocyaninato] Indium (III) chloride (2)	Linked to AgNPs via metal (Ag) to sulfur	Photophysics and Non Linear Optics	**[69]**
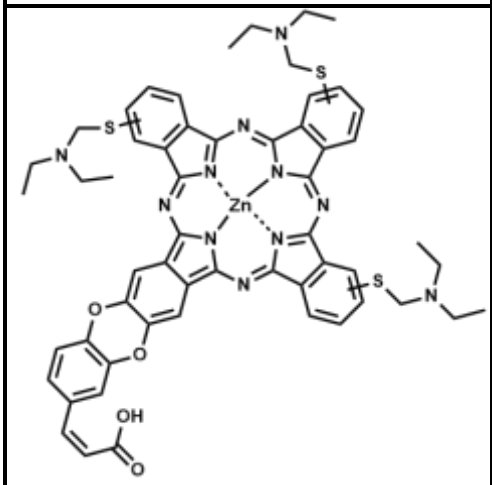	tris{11,19,27-(1,2-diethylaminoethylthiol)-1,2(caffeic acid) Pc Zinc (II)	Linked to AgNPs via amide bond	Photophysics and PACT	**[70]**
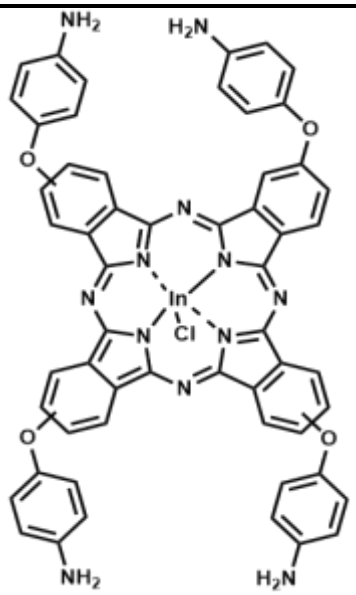	2(3),9(10),16(17),23(24)-tetrakis-(4-aminophenoxy) phthalocyaninato indium(III) chloride (InPc)	Linked to Fe_3O_4-SiNPs and SiNPs via amide bond	Photophysics and NLO	**[71]**

MPc used in this work are shown in **Table 1.2**. They include neutral and zwitterionic complexes. As **Table 1.1** shows there are still very few asymmetrical Pc used for PACT [66,70]. Asymmetry improves triplet state population of Pcs [72]. There is only one example of cationic Pc [66] with MNPs used for PACT hence cationic Pcs are employed in this work. In addition, a combination of AgNPs with MNPs has not been employed in the presence of MPcs for PACT. The combination of AgNPs, MNPs and SiNPs is also employed for the first time. No zwitterionic Pcs have ever been employed for PACT alone or with NPs and are subject of this thesis. Cationic photosensitizers are reported to have more antimicrobial activity than their anionic and neutral counterparts towards Gram negative bacteria, such as *E. coli* [73–76]. Cationic MPc derivatives also have enhanced photosensitizing ability due to improved solubility in aqueous media [77,78]. Zwitterionic compounds display different charges on one molecule [79]. Microbial adhesion onto surfaces and subsequent formation of biofilm are critical issues for many biomedical applications. Therefore, one of the most effective practises in preventing the formation of biofilm is to avoid or reduce the initial adhesion of bacteria to a surface [80,81]. Zwitterionic surfaces are known to inhibit bacterial adhesion and prevent biofilm formation hence zwitterionic MPcs derivatives are employed in this work for PACT. Zn and In were chosen as central metals for the MPcs due to their heavy–atom effect which encourages intersystem crossing to the triplet state leading to enhanced triplet state, and singlet quantum yields as well as improved PACT activity. This work reports for the first time on the linkage of symmetrical zwitterionic MPcs to Ag-Fe_3O_4 OLA/OLM NPs and Ag@Fe_3O_4 OLA/OLM NPs.

Subsequently, their antimicrobial PACT activity was investigated for the first time in this work. Neutral asymmetric Pc complexes were studied in the presence of NPs for photophysicochemical properties and not for PACT. Pc complexes **1**, **3**-**6** are new, **2** has been reported before [82].

Table 1.2: Synthesised Pcs and their conjugates with NPs, nanoparticles (AgNPs), silver-iron core shell NPs (Ag@Fe_3O_4), silver-iron dimer NPs (Ag-Fe_3O_4), Silica NPs (SiNPs) and AgFe_3O_4@SiNPs

Molecular structure	Phthalocyanine	NPs and bond formed with Pc	Studies	R
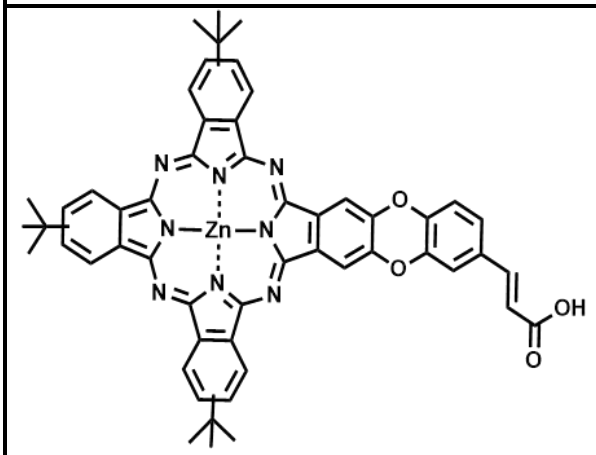	Monocaffeic acid tri–tert–butyl phthalocyanine zinc (II)	Linked to AgNPs-GSH SiNPs-APTES, Ag@Fe_3O_4-GSH and Ag@Fe_3O_4-SiNPs-APTES via amide bond	Photophysics	(N

	Monocarboxyphenoxy tri–tert–butylphenoxyl phthalocyanine zinc (II)	Linked to AgNPs SiNPs-APTES, Ag@Fe_3O_4-GSH and Ag@Fe_3O_4-SiNPs-APTES via amide bond	Photophysics	[8
	Tetrakis phenoxy *N,N*-dimethyl-4-(methylimino) phthalocyanine indium (III) chloride	Linked to Ag-Fe_3O_4 OA/OLA and Ag@Fe_3O_4 OA/OLA Via ligand exchange	Photophysics and PACT	3 (N
	Tetrakis phenoxy N, N-dimethyl-(3-sulfopropyl)ammonium) propyl]-4-((methylimino) indium (III) chloride	Linked to Ag-Fe_3O_4 OA/OLA and Ag@Fe_3O_4 OA/OLA Via ligand exchange	Photophysics and PACT	4 (N

	TetrakisN,N-dimethyl-4(methylimino) indium (III) chloride phthalocyanine	Linked to Ag-Fe_3O_4 OA/OLA and Ag@Fe_3O_4 OA/OLA Via ligand exchange	Photophysics	5 (N
	Tetrakis N,N-dimethyl-(3-sulfopropyl)ammonium)propyl]4-(methylimino) indium (III) chloride phthalocyanine	Linked to Ag-Fe_3O_4 OA/OLA and Ag@Fe_3O_4 OA/OLA Via ligand exchange	Photophysics	(N

1.2.3 Electronic absorption spectra of MPcs

The absorption spectra of MPcs are usually characterised by two absorption bands namely, the B–band and Q–band. These bands are usually located around 300-400 nm and 650-900 nm, respectively, as shown in **Fig. 1.4**. The ground state electronic absorption resulting from π-π transitions of MPcs is influenced by the nature of central metal, the ring substituents and the point of substitution (β or α).

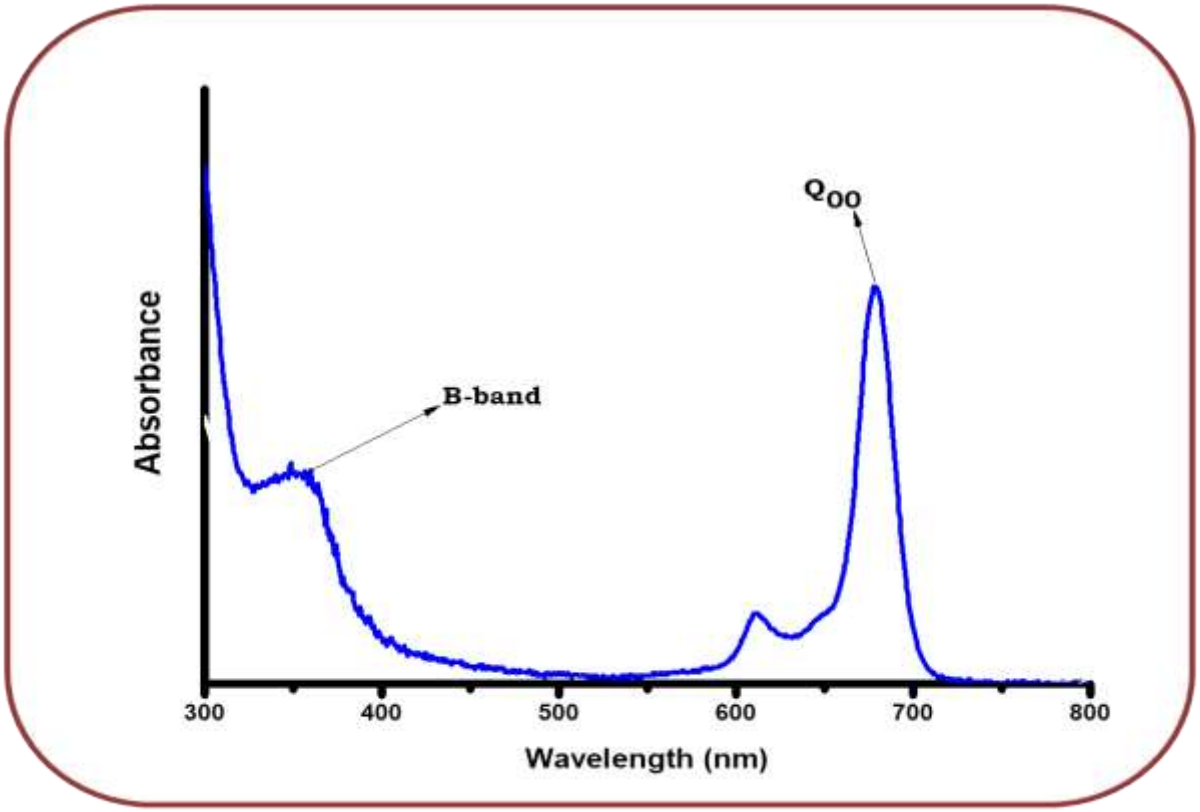

Figure 1.4: Typical absorption spectrum of metallated Pc, unpublished work.

The symmetrical Q-band of MPcs is a result of transitions between the ground state a_{1u} of the highest occupied molecular orbital (HOMO) to e_g of the lowest unoccupied molecular orbital (LUMO), a weak vibronic band

centered around 620 nm also accompany the Q-band, The B band originates from the a_{2u} or b_{2u} to eg transitions **Fig. 1.5** [83–85].

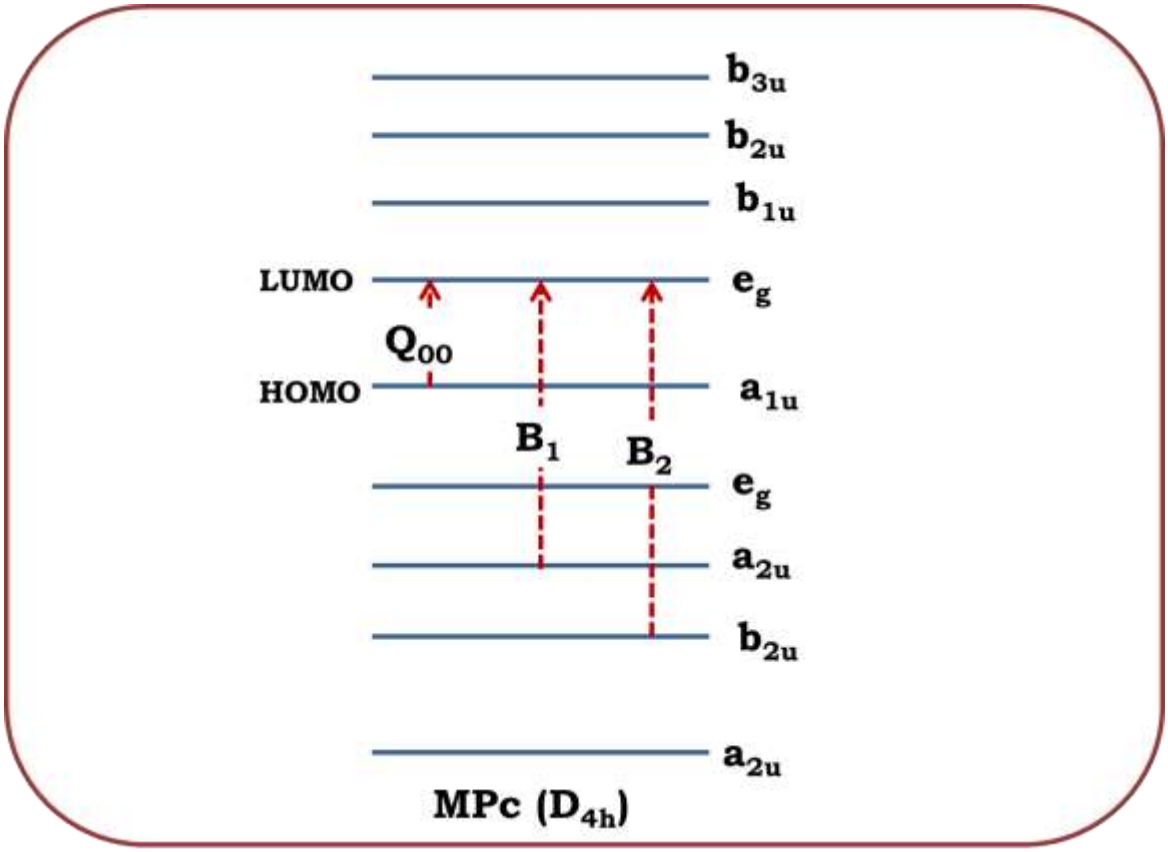

Figure 1.5: Electronic transitions in metallated Pcs showing the origin of the Q_{00}, B_1 and B_2 absorption bands.

1.3 Photodynamic Antimicrobial Chemotherapy (PACT)

PACT involves the use of light of appropriate wavelength in combination with a photosensitiser (PS). This interaction generally results in the release of singlet oxygen and other reactive oxygen species (ROS) that are lethal to the target pathogen [86,87]. PACT has emerged as a hopeful treatment for treating drug resistant pathogens. Gram-negative bacteria such as *Escherichia-coli (E-coli)* are known to cause various diseases, including pneumonia, urinary tract infections, and diarrhoea. *E-coli* have an outer membrane in the cell wall structure that can serve as a protective barrier to control the influx and efflux of solutes, thus making it more difficult to treat [88,89]. Of interest in this thesis is the use of selected Pcs and their conjugates (with NPs) as photosensitizers in PACT. Photophysicochemical parameters such as increased singlet oxygen quantum yield make Pcs and their conjugates suitable photosensitisers for PACT. In this work selected neutral, zwitterionic MPcs and their conjugates are used to treat bacteria (*E-coli).*

1.4 Photophysical and photochemical properties of MPcs

The photophysicochemical properties of Pcs may be described using a modified Jablonski diagram, **Fig. 1.6** [90]. MPcs absorb photon energy in the ground state (S_0) and get excited to the singlet excited state (S_1) where they either undergo intersystem crossing to the first triplet state or undergo fluorescence in the process. In the triplet state phosphorescence or energy transfer from the triplet state to molecular oxygen ($^3O_2$) to generate singlet oxygen ($^1O_2$) or other reactive oxygen species (ROS) occurs. Singlet oxygen

and other ROS are highly toxic upon interaction with living organisms due to induction of oxidative damage to the DNA, biological membranes which results in mortality of the micro-organism, this is of importance for PACT. Photophysical/chemical parameters determined in this work are fluorescence (Φ_F), triplet (Φ_T) and singlet oxygen (Φ_Δ) quantum yields and they are described next.

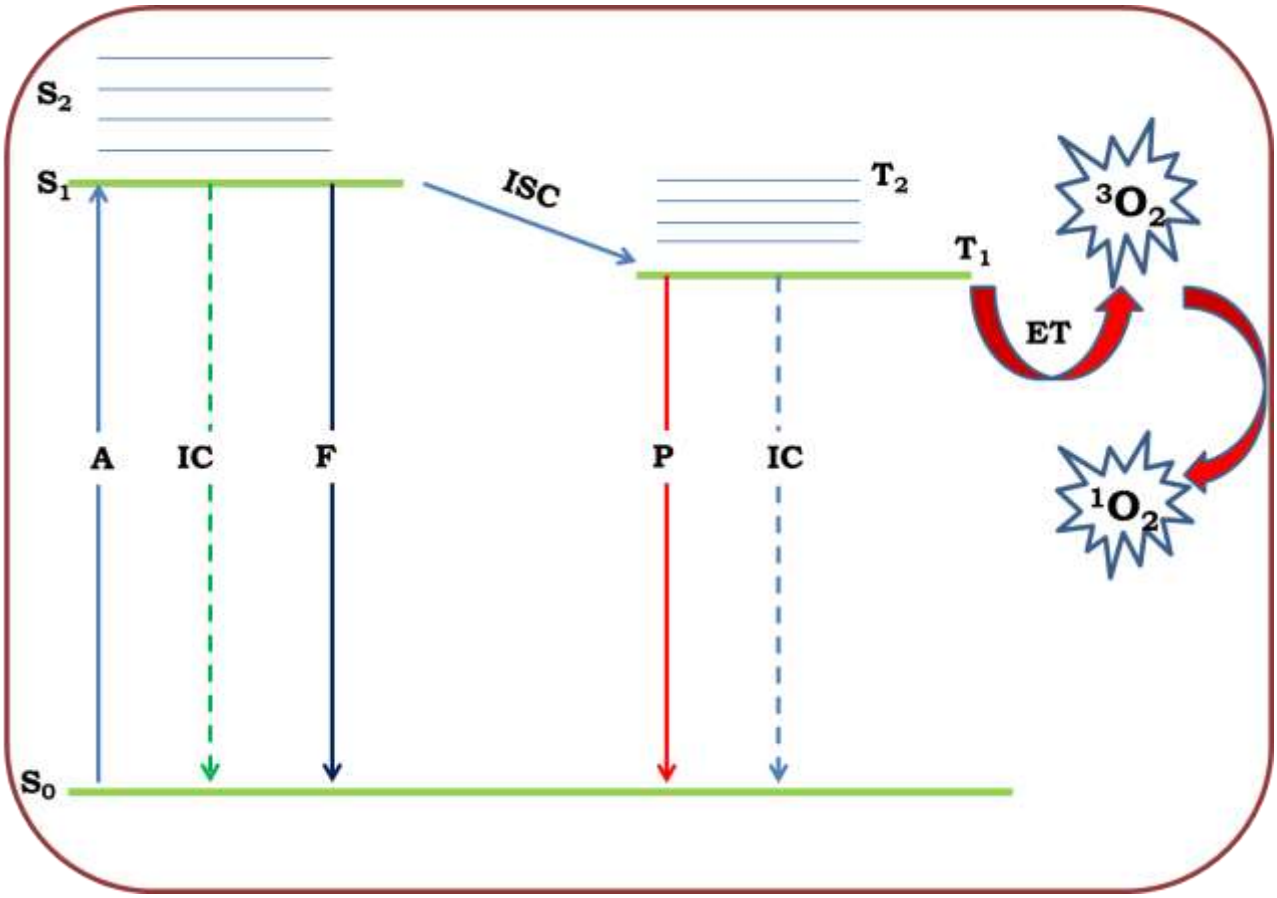

Figure 1.6: A modified Jablonski diagram: A = Absorbance, S_0 = Ground singlet state, S_1 = First singlet excited state, S_2 = Second singlet excited state, IC = Internal conversion, F = Fluorescence, ISC = Intersystem crossing, P = Phosphorescence, ET =Energy transfer, T_1 =

First triplet state, T_2 = Second Triplet state, $^3O_2$ = ground state oxygen, $^1O_2$ = Singlet oxygen.

1.4.1 Fluorescence quantum yields (Φ_F) and lifetimes (τ_f)

Fluorescence quantum yield denoted as Φ_F is the direct measure of the efficiency of the conversion of absorbed photons into emitted photons [91]. Fluorescence quantum yields of Pcs are influenced by several factors which include, atomic mass of the central metal, the nature of the ring substituents and the point of substitution on the Pc, nature of the solvent, photo-induced energy transfer (PET), temperature and concentration of the measured solution as well as the presence of NPs [92–94]. NPs conjugated to MPcs with heavy metals in their central cavity have been reported to quench fluorescence due to the spin orbit coupling, (the heavy atom effect) [95,96]. In this thesis a comparative approach was followed using the Φ_F of a known unsubstituted zinc phthalocyanine (ZnPc) as a standard. In this work ZnPc in dimethyl sulfoxide (DMSO) with (Φ_F) = 0.20 [97] was employed. The Φ_F was determined using equation (1.1).

$$\Phi_F = \Phi_F^{std} \frac{F\ A^{std} n^2}{F^{std} A\ n^{2\ std}} \qquad \textbf{(1.1)}$$

where Φ_F and Φ_F^{std} are the fluorescence quantum yield of the sample and the standard respectively. F and F^{std} are the sum of areas under the fluorescence emission curves of the sample and the standard, respectively. A and A^{std} are the absorbances of the sample and the standard at the excitation wavelength respectively. n and n^{std} are the refractive indices of the solvents used for the sample and the standard preparation, respectively.

Fluorescence lifetimes (τ_f) is defined as the average time a molecule spends in its excited singlet state S_1 before spontaneous emission. The τ_f measurements were determined using the Time Correlated Single Proton (TCSPC) technique in this work.

1.4.2 Triplet quantum yields (Φ_T) and lifetimes (τ_T)

The Φ_T is used to measure the efficiency of Pc molecules to populate the triplet state. The lifetime of the triplet state can be described as the time taken by Pc molecule in the excited triplet state T_1. There are several techniques used to determine Φ_T, these include flash photolysis, triplet sensitized isomerization, photo-oxidation, delayed fluorescence analysis, absorption recovery studies, spatially separated triplet excitation and detection, laser gain studies, double-pulse transmission measurements, and electron spin resonance analysis [98]. In this work, the laser flash photolysis technique was employed; this involves the use of a known standard such as ZnPc. The measurements were done using equation (1.2) [99].

$$\Phi_T = \Phi_T^{std} \frac{\Delta A_T \, \varepsilon_T^{std}}{\Delta A_T^{std} . \varepsilon_T} \qquad \textbf{(1.2)}$$

where Φ_T^{std} is the triplet quantum ZnPc standard Φ_T^{std}= 0.65 DMSO [100]. ΔA_T^{std} and ΔA_T are the changes in the triplet state absorbance of the standard and the measured sample, respectively. ε_T^{std} and ε_T represent the state molar extinction coefficients of the standard and sample, respectively. ε_T^{std} and ε_T were determined using equations (1.3a) and (1.3b) respectively.

$$\varepsilon_T = \varepsilon_S \frac{\Delta A_T}{\Delta A_s} \qquad \textbf{(1.3a)}$$

$$\varepsilon_T^{std} = \frac{\Delta A_T^{std}}{\Delta A_S^{std}} \qquad \textbf{(1.3b)}$$

where ε_S is the singlet state molar extinction coefficient of the sample or standard. ΔA_s^{std} and ΔA_s are the changes in the singlet state absorbances of the standard and the measured sample, respectively.

1.4.3 Singlet oxygen (Φ_Δ) quantum yield

When there is interaction between excited triplet state of MPcs with ground state molecular oxygen ($^3O_2$), singlet oxygen ($^1O_2$) is formed which is responsible for bacteria mortality in PACT. Singlet oxygen quantum yield may be measured by two methods, through the use of chemical quenchers [101] or by the $^1O_2$ luminescence emitted at 1270 nm [102]. The chemical method was employed in this work. This method requires the use of a singlet oxygen scavengers such as 1,3 diphenylisobenzofuran (DPBF) in organic media or anthracene-9,10-bismethylmalonate (ADMA) in aqueous media that will react with singlet oxygen once it is produced in the oxygenated solution. Spectroscopic methods are employed to monitor the degradation of the singlet oxygen scavenger [103,104], **Fig. 1.7**.

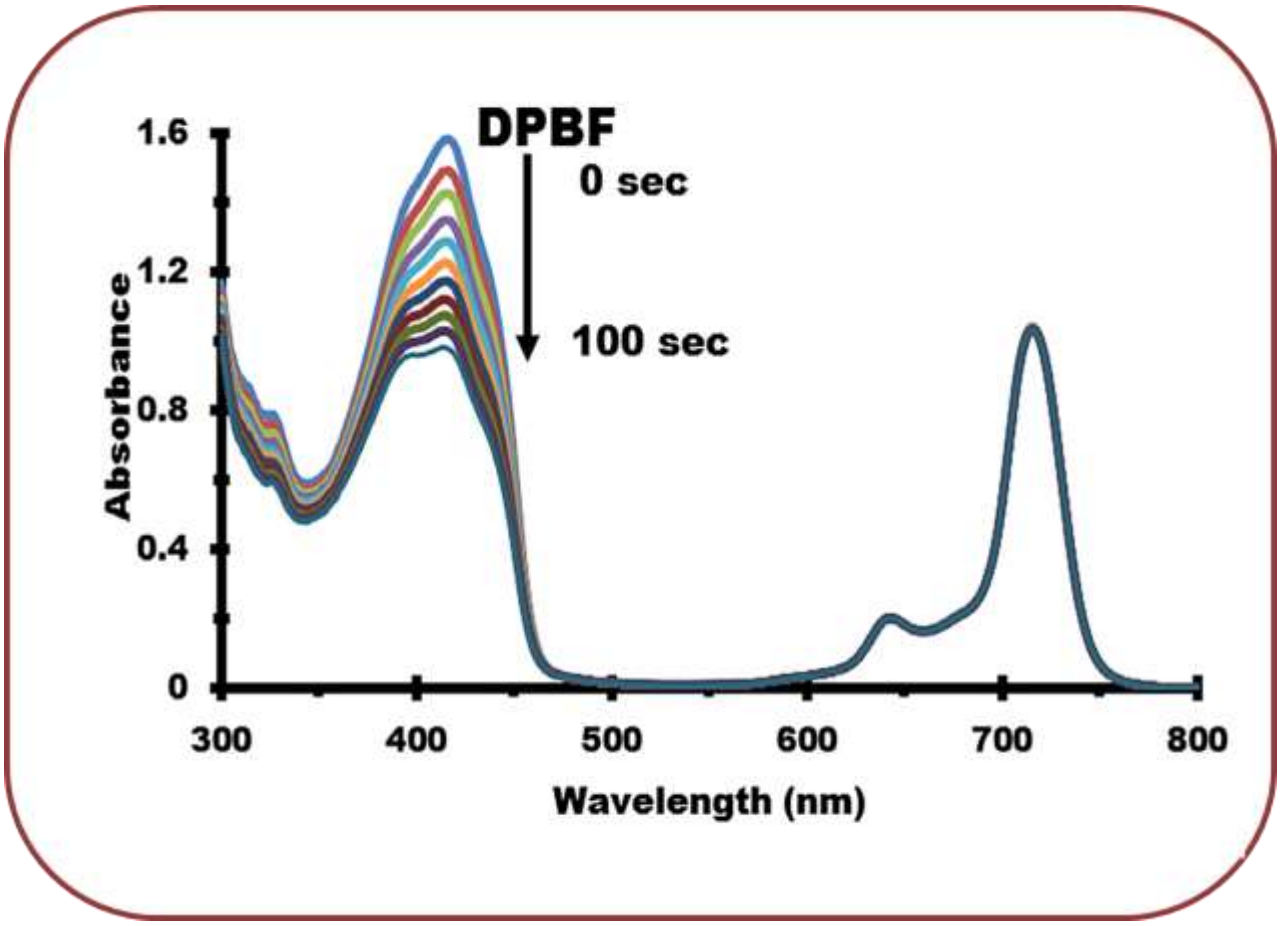

Figure.1.7 Photodegradation of DPBF with MPc as the photosensitizer.

Equation (1.4) was used to quantify the singlet oxygen quantum yield.

$$\Phi_{\Delta} = \Phi_{\Delta}^{std} \frac{R \,.\, I_{Abs}^{std}}{R^{std} \,.\, I_{Abs}} \qquad \textbf{(1.4)}$$

where Φ_{Δ}^{std} is the singlet oxygen quantum yield of the standard (ZnPc, Φ_{Δ}^{std} = 0.67 in DMSO [105]). R^{std} and R are the photobleaching rates of ADMA or DPBF in the presence of the standard and the measured sample respectively. I_{Abs} and I_{Abs}^{std} are the respective rates of light absorption by the MPcs and the standard. I_{Abs} and I_{Abs}^{std} are quantified using equation (1.5a) and (1.5b) respectively.

$$I_{Abs} = \frac{\alpha.A.I}{N_A} \qquad \textbf{(1.5a)}$$

$$I_{Abs}^{std} = \frac{\alpha.A.I}{N_A} \qquad \textbf{(1.5b)}$$

where $\alpha = 1 - 10^{-A(\lambda)}$, $A(\lambda)$ is the absorbance of sensitizer at the excitation wavelength, I is the intensity of light expressed as photons (cm^{-2} s^{-1}) and N_A is the Avogadro's constant.

1.5 Summary of aims of thesis

1. Syntheses and functionalisation of silver nanoparticles (AgNPs), silver-iron core shell NPs (Ag@Fe_3O_4), silver-iron dimer NPs (Ag-Fe_3O_4), Silica NPs (SiNPs) and Ag@Fe_3O_4-SiNPs.
2. Syntheses and characterisation of symmetrical and asymmetric MPcs
3. Linkage of nanoparticles to metallophthalocyanines using covalent linkage and phase transfer.
4. Comparative studies of the photophysicochemical properties of the phthalocyanine complexes and their conjugates in solution.
5. Photodynamic antimicrobial chemotherapy of selected metallophthalocyanines and their conjugates.

Chapter 2

Experimental

2.1 Materials.

Zinc acetate $(ZnOAc)_2$, spectroscopic grade dimethyl sulfoxide (DMSO), glutathione (GSH), deuterated chloroform ($CDCl_3$), deuterated dimethyl sulfoxide (DMSO-d_6), 4-dimethylamino benzaldehyde, 1,3-propanesultone, tetrahydrofuran (THF), dimethylformamide (DMF), 4-dimethylaminopyridine (DMAP), ethanol, methanol, (3-aminopropyl)triethoxysilane (APTES), 1,3-diphenylisobenzofuran (DPBF), dicyclohexylcarbodiimide (DCC), tetraethyl orthosilicate (TEOS), hexane, 1,8-diazabicycloundec-7-ene (DBU), and 1-pentanol were purchased from Sigma–Aldrich. *E. coli* (ATCC 25922) was purchased from Microbiologic USA. Agar bacteriological BBL Muller Hinton broth and nutrient agar were obtained from Merck. Phosphate buffer saline (10 mM PBS) pH 7.4 buffer was prepared using appropriate amounts of Na_2HPO_4, KH_2PO_4 and chloride salts using ultra-pure water, from a Milli-Q Water System (Millipore Corp, Bedford, MA, USA).

Tert-butyl phthalonitrile (**1a**) was purchased from Merck. Caffeic acid phthalonitrile (**1b**) [106], Ag-Fe_3O_4-dimer OLA/OLM NPs [107] and Ag@Fe_3O_4-core shell OLA/OLM NPs [65,108], AgNPs-GSH [109], SiNPs-APTES [110] along with complexes (**3b)** [111], **(5b)** [112] and Zn monocarboxyphenoxy tri–*tert*–butylphenoxyl phthalocyanine (complex-**2**) [82] were synthesized as reported in literature.

2.2 Equipment.

i. Ground state electronic absorption spectra were measured using a Shimadzu UV-2550 spectrophotometer.

ii. Fluorescence excitation and emission spectra were measured on a Varian Eclipse spectrofluorimeter using 360–1100 nm filter. Excitation spectra were recorded using the Q–band of the emission spectra. The Q-band absorbance of the samples and standard were adjusted to ~0.05 to avoid inner filter effects.

iii. Fluorescence lifetimes were measured using a time single photon counting setup (TCSPC) (FluoTime 300, Picoquant GmbH) with a diode laser (LDH-P-670, Picoquant GmbH, 20 MHz repetition rate, 44 ps pulse width), as described in [113].The layout is shown in **Fig. 2.1**

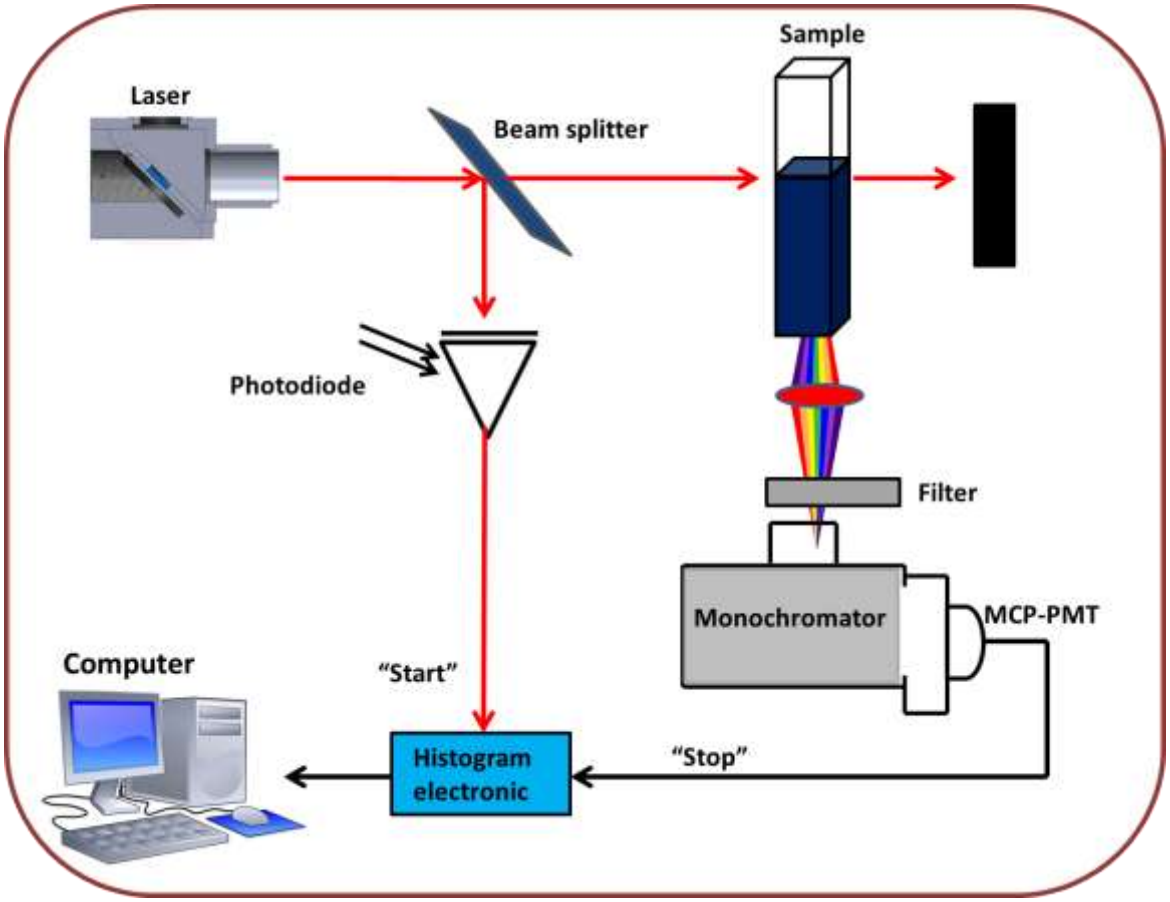

Figure 2.1: Time correlated single photon counting (TCSPC) setup.

iv. Triplet quantum yields were determined using a laser flash photolysis system consisting of a LP980 spectrometer with a PMT-LP detector and an ICCD camera (Andor DH320T-25F03) was used to determine triplet quantum yields. The signal from a PMT detector was recorded on a Tektronix TDS3012C digital storage oscilloscope. The excitation pulses were produced using a tunable laser system consisting of a Nd-YAG laser (355 nm, 135 mJ/4–6 ns) pumping an optical parametric oscillator (OPO, 30 mJ/3–5 ns) with a wavelength range of 420–2300 nm (NT-342B, Ekspla). The detailed procedure of the flash photolysis experiment is as follows: The absorbance of sample solution and the

standard were ~1.5 at Q band. The solution was introduced into a 1 cm path length UV–Visible spectrophotometric cell and deaerated using argon for 30 min. Thereafter the solution was sealed and illuminated using an appropriate excitation wavelength (the crossover wavelength of the sample and the standard, which was ~ 670 nm). The maximum triplet absorption detection wavelength was determined from the transient curve. The triplet lifetimes were determined by exponential fitting of the kinetic curves using OriginPro 8 software.

v. Irradiation for singlet oxygen quantum yield was performed using a general electric quartz lamp (300 W) as described in the literature [114]. An interference filter, 670 nm with a band of 40 nm, was placed just before the sample chamber, **Fig. 2.2**. Light intensity was measured with a POWER MAX 5100 (Molelectron detector incorporated) power meter and was found to be 4.3×10^{15} photons cm^{-2} s^{-1}.

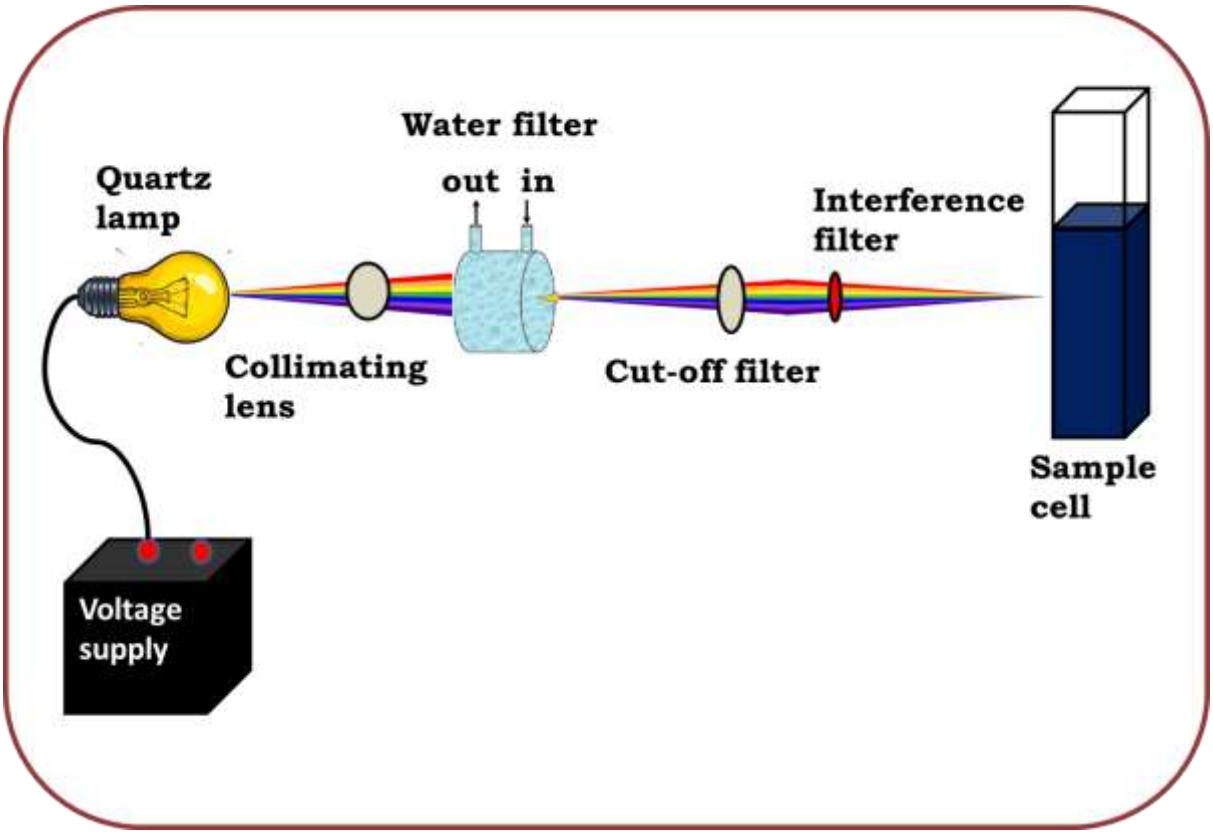

Figure 2.2: Singlet oxygen setup.

vi. X-ray powder diffraction patterns were recorded using a Cu Kα radiation (1.5405˚A, nickel filter), on a Bruker D8 Discover equipped with a proportional counter and the data was processed using the Eva (evaluation curve fitting) software.

vii. Infrared spectra were acquired on a Bruker ALPHA FT–IR spectrometer with universal attenuated total reflectance (ATR) sampling accessory.

viii. Mass spectra data were collected on a Bruker AutoFLEX III Smart-beam TOF/TOF mass spectrometer using α-cyano-4-hydrocinnamic acid as the matrix.

ix. ^{1}H NMR spectra were recorded on a Bruker AVANCE II 600 MHz NMR spectrometer using tetramethylsilane (TMS) as an internal reference.

x. Elemental analyses were performed using a Vario-Elementar Microcube ELIII.

xi. The morphologies of the NPs and their conjugates with Pcs were assessed using a transmission electron microscope (TEM), ZEISS LIBRA model 120 operated at 90 kV and iTEM software was used for TEM micrographs processing.

xii. Elemental compositions of the NPs and the conjugates were qualitatively determined using energy dispersive X-ray spectroscopy (EDX), INCA PENTA FET coupled with the VAGA TESCAM operated at 20 kV accelerating voltage.

xiii. Autoclave RAU-530D was used for the sterilization and autoclaving of nutrient broth, nutrient agar and phosphate buffer and other various apparatus for PACT studies.

xiv. The optical density of the bacteria culture was monitored using the LEDETECT 96 from LABXIM PRODUCTS.

xv. HERMLE Z233M-2 centrifuge was used for the harvesting of the bacteria cells by centrifugation process.

xvi. The homogenization of the bacteria suspension was done using PRO VSM-3 Lab plus Vortex mixer.

xvii. The incubation processes for the photodynamic antimicrobial chemotherapy was done using the thermostatic oven.

xviii. Scan® 500 automatic color colony counter was utilised to determine the colony forming units (CFU)/mL of the bacteria.

xix. Illumination for PACT studies of Pcs and conjugates were performed using a Modulight® Medical Laser system (ML) 7710-680 channel Turnkey laser system coupled with 2 X 3W channels at 680 nm, cylindrical output channels, aiming beam, integrated calibration module, foot/hand switch pedal and fibre sensors (subminiature version A).

2.3 Syntheses.

2.3.1 Mono caffeic acid tri–*tert*–butyl phthalocyanine zinc (II) (complex 1), Scheme 3.1

Caffeic acid phthalonitrile (**1b**) [106] (0.1 g, 0.329 mmol), *tert*-butyl phthalonitrile (**1b**) (0.934 g, 5.07 mmol) and zinc acetate (0.045 g, 0.21 mmol) were weighed into a round bottom flask, then 1-pentanol (3 mL) and DBU (1 mL) were added into the reaction mixture in the presence of argon atmosphere and refluxed at ~140 °C for 12 h. The crude product was precipitated using ethanol under centrifugation and chromatographed over silica gel using hexane: THF (1:1) and THF: methanol (9:1). Yield = 36%: IR (KBr, cm^{-1}): 3460 (OH), 2800-2956 (C-H stretch), 1575-1600 (C=O), 1125 (C-N stretch), 1238-1090 (C-O-C). ^1H NMR (600MHz, $CDCl_3$) ppm: 2.63 (27H, m, butyl–H), 3.02 (2H, s, Alkene–H), 6.59 (3H, s, Phenyl–H), 7.92 – 7.54 (11H, m, Pc aromatic–H). 7.97 (1H, s, OH). UV/vis (DMSO), λ_{max}, nm (log ε): 679 (4.80), 611 (4.05), 356 (4.47). MALDI TOF MS m/z: Calculated: 922.37 Found: 923.02 $[M + H]^+$. Calcd for $C_{53}H_{44}N_8O_4Zn$ = C (69.02), H (4.81), N (12.15) found C (70.58), H (5.02), N (11.75).

2.3.2 Tetrakis phenoxy *N,N*-dimethyl-4-(methylimino) phthalocyanine indium (III) chloride (complex 3), Scheme 3.2

Complex **3** was synthesized as follows [115,116]: a solution of complex **3b** (0.157 g, 0.153 mmol) in 10 mL dry THF was added dropwise to a solution of 4-(dimethyl amino) benzaldehyde (0.091 g, 0.611 mmol) in 15 mL dry THF. The mixture was refluxed under argon for 22 h. The crude product was

separated by filtration as a green solid, this was dissolved in chloroform (5 mL) and complex **3** was precipitated by the dropwise addition of methanol. The precipitate was filtered, successively washed with cold water, methanol and ethanol and air dried in the fumehood to give **3**. Yield= 77%: IR (cm^{-1}): 3329-3186 (C−H aromatic), 3076-2926 (N-CH_3), 1601 (C=N imine), 1473 (aromatic), 1335 (C−N aryl), 1265 (C−O−C), 945, 829, 744, 680 (Pc-ring). ^1H NMR (600 MHz, DMSO-d_6): δ, ppm 1.76-2.38 (m, 24 *H*, N-CH_3), 2.90-3.05 (s, 4*H*, Alkene-H), 6.77-7.19 (m, 22*H*, Aromatic-H), 7.68 (d, 6*H*, Aromatic-H), 8.25 (s, 4*H*, Aromatic-H), 9.67 (s, 6*H*, Pc aromatic H), 10.3 (s, 6*H*, Pc aromatic H). (DMSO), λ_{max}, nm (log ε): 698 (4.4), 629(3.9), 339 (4.1).MALDI TOF MS m/z: Calculated: 1615.96 found 1616.0 $[M + H]^+$. Calcd for $C_{92}H_{72}N_{16}O_4ClIn$ = C (68.49), H (4.64), N (13.74) found C (70.04), H (5.27), N (12.14).

2.3.3 Tetrakis phenoxy *N, N*-dimethyl-(3-sulfopropyl) ammonium) propyl]-4-(methylimino) phthalocyanine indium (III) chloride (complex 4), Scheme 3.2

Synthesis of complex **4** was carried out using the procedure reported in [80] as follows: **3** (0.155 g, 0.073 mmol) and excess 1, 3-propanesultone (1.54 g, 12.6 m mol) were dissolved in DMF (5 mL). The mixture was stirred under argon at 70 ^0C for 22 h; the obtained green product was then cooled to room temperature and precipitated with chloroform using centrifugation. The precipitate was filtered off and washed with acetone to remove unreacted 1,3-propanesultone. The crude product was dissolved in water and re-

filtered. The filtrate was precipitated with acetone to collect the pure product by centrifugation. The product was air dried in fumehood, and the final product is represented as complex **4**. Yield = 73%: IR (cm^{-1}): 3329, 3186 (C-H aromatic), 3076-2926 (N-CH_3) 1600 (C=N imine), 1473 (aromatic), 1335 (C-N aryl), 1265 (C-O-C), 1157 (S=O). ^{1}H NMR (600 MHz, DMSO-d6): δ, ppm 1.55-2.15 (m, 26*H*, Alkane-H), 2.21-2.39 (m, 5*H*, Alkane-H), 2.52-2.85 (m, 17*H*, Alkane-H), 3.06 (s, 2*H*, Alkene-H), 3.25 (s, 2*H*, Alkene-H), 6.73-7.78 (m, 28*H*, Aromatic-H), 8.21 (s, 4*H*, Aromatic-H), 9.72 (s, 12*H*, Pc-Aromatic-H), DMSO), λ_{max}, nm (log ε): 694 (4.3), 626(3.7), 336 (4.1). MALDI TOF MS m/z: Calculated: 2104.55. Found: no signal. Calcd for $C_{104}H_{96}N_{16}O_{12}S_4ClIn$=C (59.56), H (4.62), N (10.58), S (6.06), found C (61.04), H (4.84), N (9.13), S (7.11).

2.3.4 Tetrakis *N,N*-dimethyl-4-(methylimino) phthalocyanine indium (III) chloride (complex 5), Scheme 3.3

Complex **5** was synthesised as outlined for complex 3 except **5b** (0.551 g, 0.762 mmol) and 4-(dimethylamino) benzaldehyde (0.455, 3.052 mmol) were employed. Reaction time was as outlined for 3. Yield = 57%: IR (cm^{-1}): 3329-3186 (C-H aromatic), 2926-2845 (N-CH_3) 1596 (C=N imine), 1455 (C=C aromatic). ^{1}H NMR (600 MHz, DMSO-d_6): δ, ppm 1.02-1.40 (m, 13*H*, Alkane-H), 1.68-2.34 (m, 11*H*, Alkane-H), 2.72 (s, 2*H*, Alkene-H), 2.89 (s, 2*H*, Alkene-H), 6.42-6.90 (m, 10 *H*, Aromatic-H), 7.42 (d, 2*H*, Aromatic-H, 7.68 (d, 2*H*, Aromatic-H), 7.95 (s, 2*H*, Aromatic-H). 8.30-8.45 (m, 6*H* Pc aromatic H), 8.90-9.10 (m, 6*H* Pc-aromatic H). (DMSO, λ_{max}, nm (log ε): 745(4.7), 668(4.4), 348 (4.9).MALDI TOF MS m/z: Calculated: 1246.14, found 1247.6

[M +H]$^+$. $C_{68}H_{56}N_{16}O_{12}ClIn$=C (65.98), H (5.46), N (17.10) found C (65.39), H (6.25), N (17.85).

2.3.5 Tetrakis *N,N*-dimethyl-(3-sulfopropyl) ammonium)propyl]4-(methylimino) phthalocyanine indium (III) chloride (complex 6), Scheme 3.3

Syntheses of complex **6** was as described for complex **4** except complex **5** was used: **5** (0.155 g, 0.124 mmol). The amount of the rest of reagents and solvents as well as purification method is as outlined for complex **4**. Yield 63%: IR (cm^{-1}): 3329-3186 (C-H aromatic), 2926-2845 (N-CH_3) 1600 (C=N imine), 1088 (S=O aromatic). ^{1}H NMR (600 MHz, D_2O): δ, ppm 1.16-1.69 (m, 9*H*, Alkane-H), 1.77-2.31 (m, 8*H*, Alkane-H), 2.69-3.83 (m, 31*H*, Alkane-H), 4.42 (s, 4*H*, Alkene-H), 7.04-8.34 (m, 16*H*, Aromatic-H), 9.16-9.95 (m, 12*H*, Pc aromatic H). λ_{max} DMSO), nm (log ε): 743(4.1), 661(3.8), 343 (4.3). $C_{80}H_{80}N_{16}O_{12}S_4ClIn$ = C (55.35), H (4.64), N (12.91), found C (56.34), H (5.54), N (12.14).

2.3.6 APTES modified Ag@Fe_3O_4-SiNPs Scheme 3.4.

The synthesis of (3-aminopropyl) triethoxysilane (APTES) functionalised Ag@Fe_3O_4-SiNPs-APTES was as follows: OLA/OLM capped $AgFe_3O_4$ NPs (0.26 g) were dispersed in a degassed mixture of absolute ethanol (40 mL) and water (40 mL), followed by ultrasonication of the mixture for 30 min. Then, 5 mL of tetraethyl orthosilicate (TEOS) was added to the mixture and the pH was adjusted to 9 using 25% ammonium hydroxide (0.27 mL). The mixture was stirred in argon environment for 12 h. Then 0.5 mL of APTES was added and the mixture was refluxed in nitrogen atmosphere at ~130 °C

for 24 h. The product was precipitated under centrifugation using ethanol and air-dried in fume-hood; the final product is represented as Ag@Fe_3O_4-SiNPs-APTES.

2.3.7 GSH functionalized Ag@Fe_3O_4 OLA/OLM NPs, Scheme 3.4

The OLA/OLM capped Ag@Fe_3O_4 NPs [47,65] were modified with glutathione (GSH) as follows: a solution containing methanol (20 mL), GSH (0.25 g, 0.81 mmol) and KOH (0.50 g, 8.93 mmol) was added to the colloidal OLA/OLM capped Ag@Fe_3O_4 NPs (0.05 g/mL). The mixture was allowed to stir for 2 h at room temperature. Afterwards, the formed GSH capped NPs were precipitated out of solution under centrifugation using ethanol, the obtained product was further purified with methanol and air dried in the fume-hood to give Ag@Fe_3O_4 NPs-GSH.

2.3.8 Conjugations of complexes 1 and 2 to the NPs-via amide bond, Scheme 3.5

The conjugation of complexes **1** and **2** to NPs were performed as described in the literature [47] as follows. Complexes **1** (0.02g, 0.017 mmol) or **2** (0.03 g, 0.026 mmol) were separately dissolved in 2 mL of dry DMF in the presence of DCC (0.01 g, 0.049 mmol) and DMAP (0.005 g, 0.042 mmol). The mixture was stirred for 48 h. The coupling agents were added to activate the carboxylic acid group of **1** or **2** to allow for their covalent linkage with NPs via amide bond formation. Afterwards, 0.05 g NPs were added to each solution containing either **1** or **2**, and the reaction mixture was stirred for a further 48 h at ambient temperature. The conjugates were isolated out of solution with methanol under centrifugation and air-dried in fume hood.

The conjugates are represented as **Pc**-AgNPs-GSH, **Pc**-SiNPs-APTES, **Pc**-Ag@Fe_3O_4-GSH, and **Pc**-Ag@Fe_3O_4–SiNPs-APTES. The complete list is presented in **Table 3.1**.

2.3.9 Conjugation of complexes 3, 4, 5 and 6 to Ag-Fe_3O_4 OLA/OLM dimer and Ag@Fe_3O_4 OLA/OLM core shell nanoparticles via ligand exchange. Scheme 3.6

Attachment of Pc to Ag-Fe_3O_4 OLA/OLM and Ag@Fe_3O_4 OLA/OLM nanoparticles was carried out using a procedure reported in the literature [69]. Briefly, **3**, **4**, **5** and **6** (5 mg each in 10 mL of DMF) were refluxed followed by addition of 1 mg of the Ag-Fe_3O_4 OLA/OLM or Ag@Fe_3O_4 OLA/OLM NPs in 2 mL $CHCl_3$. The mixture was allowed to reflux for 2 h, cooled to the room temperature while stirring and subsequently left stirring at room temperature for a further 12 h. The mixture was diluted with methanol and the Pc-nanoconjugates were collected by centrifugation at 3000 rpm for 10 min. The products were washed with methanol and ethanol to remove the unreacted Pcs. The conjugates are represented as: **Pc-**Ag-Fe_3O_4 (for dimer), **Pc-**Ag@Fe_3O_4 (for core shell). A complete list is presented in **Table 3.1**.

2.4. Photodynamic Antimicrobial Chemotherapy studies.

2.4.1 Preparation of *E. coli*

E. coli was grown on a nutrient agar plate prepared according to the manufacturer's specifications to obtain an individual colony. The bacteria culture was prepared according to the procedure described in the literature

[117]. Briefly, aliquots of the culture were aseptically transferred to 4 mL of fresh broth and incubated at 37 ^{0}C to mid logarithmic phase (absorbance of 0.6 at 620 nm). The bacteria culture in the logarithmic phase of growth were harvested through the removal of broth culture by centrifugation (3000 RPM for 15 min), washed once with 10 mM of PBS and re-suspended in 4 mL of PBS. The bacteria culture was then diluted to 1/1000 in PBS (working stock solution), corresponding to approximately 10^{8} colony forming units (CFU) per mL.

2.4.2 Photodynamic Antimicrobial chemotherapy activity.

Photodynamic antimicrobial chemotherapy studies of the *E. coli* were performed using methods previously reported in literatures [66,118] using PBS for water soluble complex **4** and 5% DMSO in PBS for complexes **3, 4** and their conjugates. Even though complex **4** is soluble in water, its conjugates are not, hence the need for 5% DMSO.

Publications

The results discussed in the following chapters are based on work contained in the following publications.

1) Aviwe Magadla, David O Oluwole , Jonathan Britton and Tebello Nyokong, Effect of nature of nanoparticles on the photophysicochemical properties of asymmetrically substituted Zn phthalocyanines, Inorganica. Chimica. Acta. 482 (2018) 438-446.
2) Aviwe Magadla David O. Oluwole Muthumuni Managa and Tebello Nyokong, Physicochemical and antimicrobial photodynamic chemotherapy (against *E. Coli*) by indium phthalocyanines in the presence of silver-iron bimetallic nanoparticles, Polyhedron. 162 (2019) 30-38.

Chapter 3

Results and discussion

3.1 Characterisation of Phthalocyanines alone

The syntheses of complex **2** has been reported [82] and will not be discussed in the following subsections. Syntheses and characterisation of complexes **1**,**3**,**4**,**5** and **6** are reported for the first time and will be discussed in the following subsections.

3.1.1 Mono caffeic acid tri–*tert*–butyl phthalocyanine Zn (III), Scheme 3.1

Scheme 3.1 illustrates the synthesis of the asymmetrically substituted complex **1** using the mixed condensation reaction of two phthalonitriles. Low yields are expected in this synthetic approach for the formation of the asymmetrically substituted phthalocyanines due to extensive purification procedures. A yield of 36% was obtained for complex **1** synthesized in this work.

Characterization of the Pc complex **1** was achieved using infrared, ultraviolet–visible, MALDI-TOF mass and ^{1}H NMR spectroscopies, and elemental analyses.

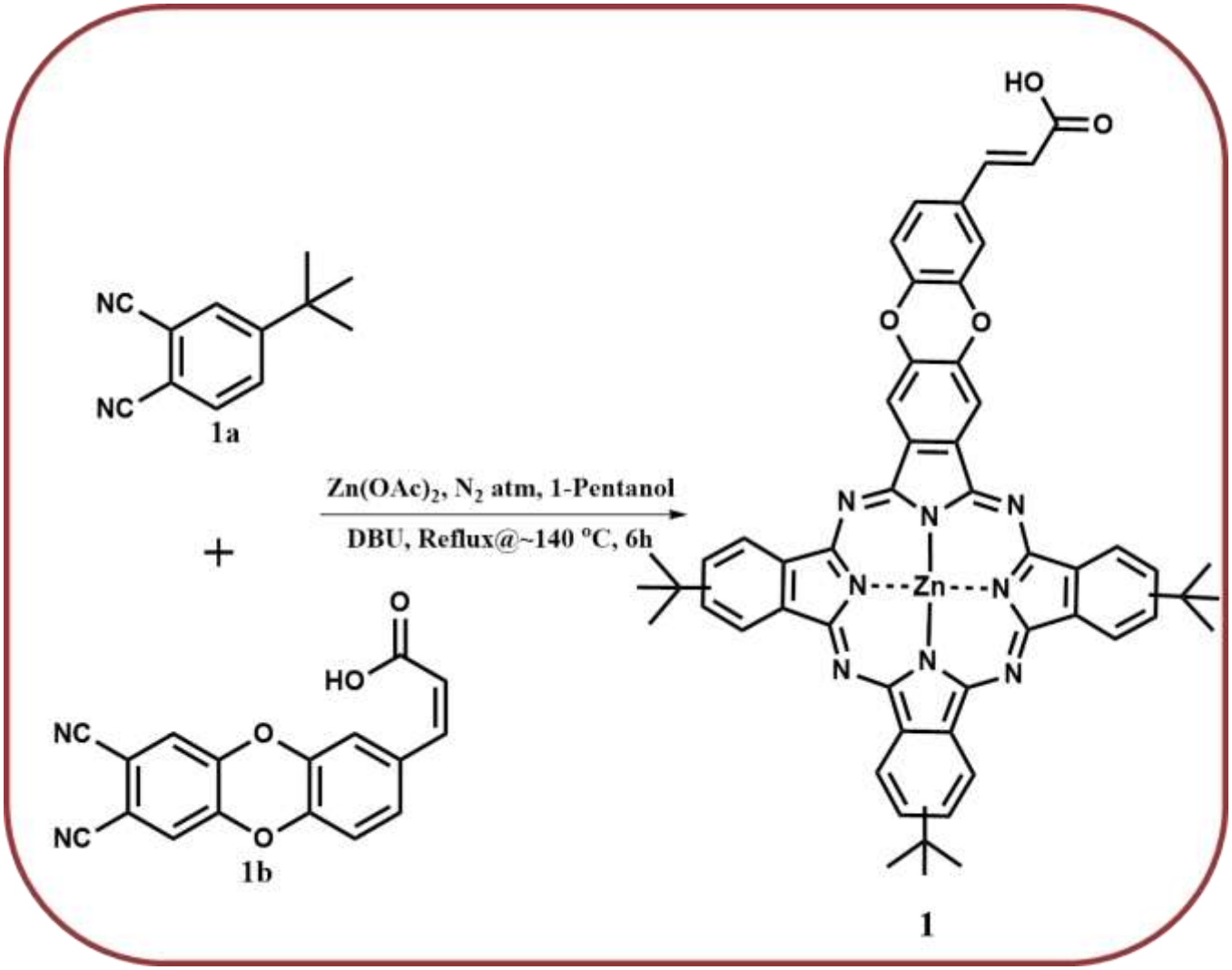

Scheme 3.1: Synthetic pathway for monocaffeic acid tri–tert–butyl phthalocyanine Zinc (II) (1) . N_2 atm = Nitrogen atmosphere, DBU = 1,8–diazabicycloundec–7–ene.

The ^{1}H NMR spectrum of complex **1** showed a singlet with resonance signal at 7.97 ppm affording 1 proton on integration corresponding to alcohol moiety. A multiplet resonating at 7.92–7.54 ppm with 11 protons on integration, corresponds to the Pc aromatic protons, the phenyl ring showed a singlet resonating at 6.59 ppm with 3 protons and the alkene substituents

depicted as a singlet accounting for 2 protons with resonance signal at 3.02 ppm (see **Fig. Appendix 1**). The *tert*-butyl substituents showed multiplet with resonance signal at 2.63 ppm affording 27 protons on integration. The rest of the peaks are due to solvents.

The UV-Vis absorption spectrum of **1** (in DMSO) has maxima at 679 nm, **Fig. 3.1**, **Table 3.1**. The spectra show characteristic narrow Q-band typical of monomeric Pcs. The excitation and absorption spectra were similar and mirror images of the emission spectra, this implies that the nuclear configurations of the ground and excited states are not affected by excitation **Fig. 3.1**.

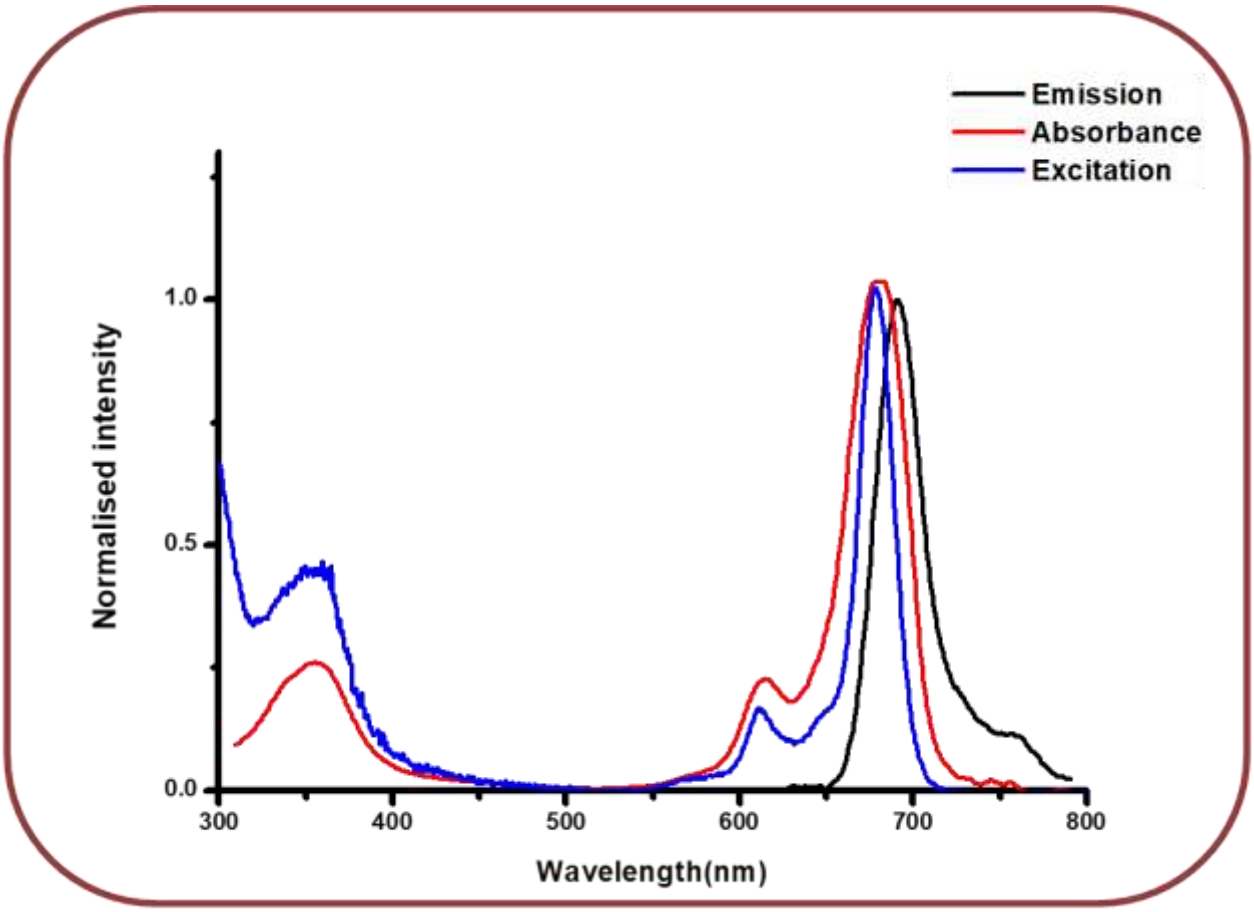

Fig. 3.1: Absorption, emission and excitation spectra of 1 in DMSO.

3.1.2 Schiff base substituted Phthalocyanines (complexes 3-6)

Scheme 3.2 and **3.3** illustrate the synthesis of symmetrically substituted phthalocyanine complexes **3**, **4**, **5** and **6**. The complexes were synthesised using Schiff's base substituents attached directly and through phenyleneoxy-bridges. Characterization of the Pc complexes was achieved using infrared, ultraviolet–visible, MALDI-TOF mass and ^{1}H NMR spectroscopies, and elemental analyses. MALDI-TOF mass spectra could not be recorded for the quarternized complexes **4** and **6**, since they did not ionize.

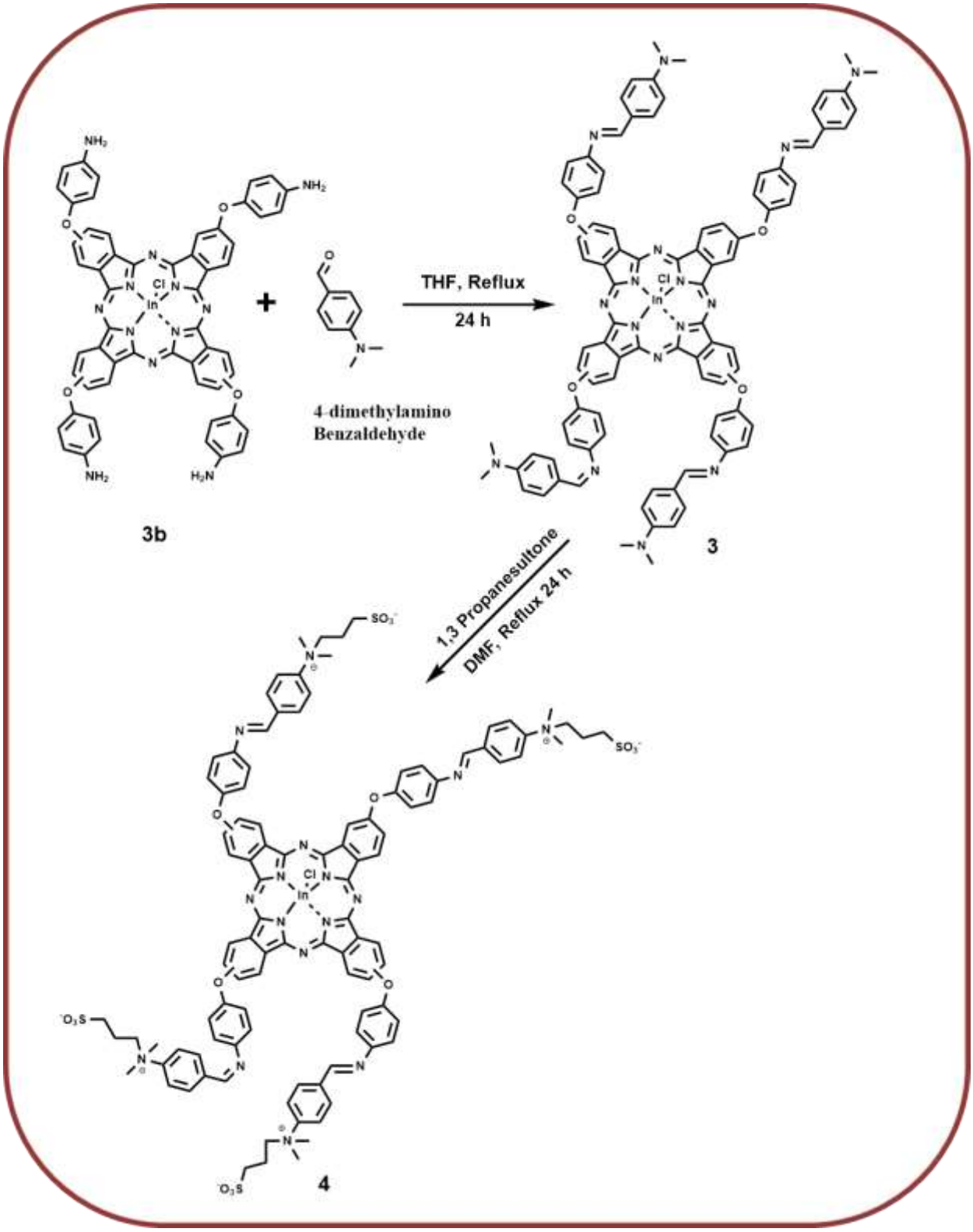

Scheme 3.2: Synthetic pathway for complexes 3 and 4.

The ^{1}H NMR spectrum of complex **3** depicted a multiplet between 1.76-2.38 ppm which gave 24 protons upon integration which correspond to the dimethyl amino group of the Schiff base moiety while the signals of the azomethine were observed as a singlet between 2.90-3.05 and integrated to give 4 protons. The Pc macrocyclic protons were observed between 9.67 and 10.3 ppm and integrated as singlets to give a total 12 protons. Protons resonating between 6.77-7.19 and at 7.68 and 8.25 integrated to give 32 protons which correspond to the phenyl rings. The additional and unintegrated signals are due to the solvent (See **Fig. A2**). For complex **4**, alkane protons (48) from the dimethyl amino group were observed as multiplets resonating between 1.55-2.15 (m, 26*H*, Alkane-H), 2.21-2.39 (m, 5*H*, Alkane-H), 2.52-2.85 (m, 17*H*, Alkane-H) and 4 alkene protons from the azomethine were observed as singlets at 3.06 (s, 2*H*, Alkene-H), 3.25 (s, 2*H*, Alkene-H). Protons resonating as a multiplet and a singlet respectively at 6.73-7.78 (m, 28*H*, Aromatic-H) and 8.21 (s, 4*H*, Aromatic-H) ppm were integrated to give 32 protons. Pc ring 12 protons were observed as a singlet let at 9.72 (s, 12*H*, Pc-Aromatic-H. The additional and unintegrated signals are due to the solvent (See **Fig. A3**).

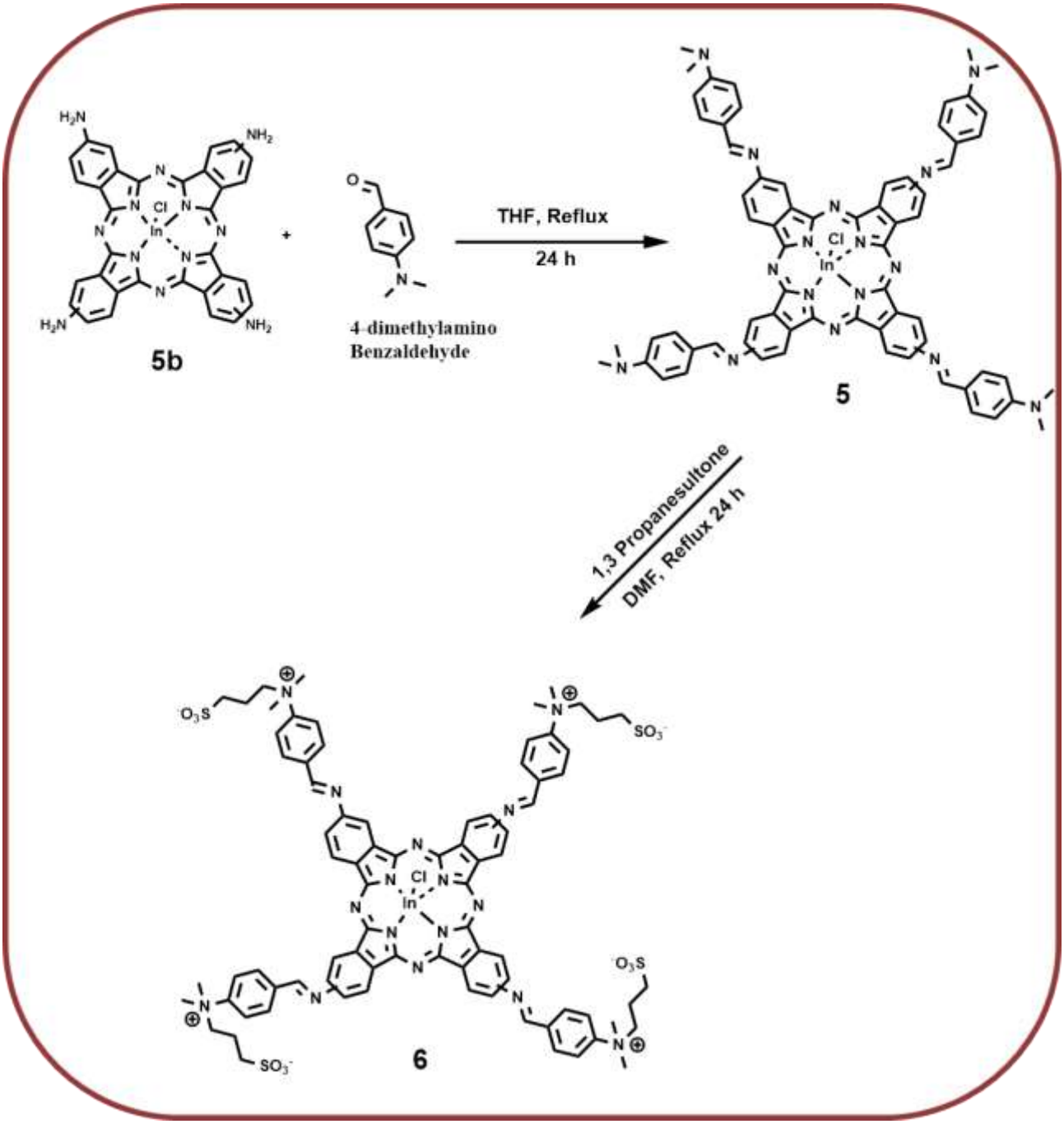

Scheme 3.3: Synthetic pathway for complexes 5 and 6.

The ^{1}H NMR spectrum of complex **5** depicted 24 protons resonating between 1.02-1.40 (m, 13*H*, Alkane-H) and 1.68-2.34 (m, 11*H*, Alkane-H) ppm and are attributed to the dimethyl amino group of the Schiff base moiety, while 4 protons resonating at 2.72 (s, 2*H*, Alkene-H) and 2.89 (s, 2*H*, Alkene-H) ppm as singlets are attributed to the azomethine moiety. For complex **5**, signals resonating between 8.30-8.45 (m, 6*H* Pc aromatic H) and 8.90-9.10 (m, 6*H* Pc-aromatic H) ppm as a multiplets are from Pc macrocyclic ring. Proton signals resonating between 6.42-6.90 (m, 10 *H*, Aromatic-H), 7.42 (d, 2*H*, Aromatic-H, 7.68 (d, 2*H*, Aromatic-H) and 7.95 (s, 2*H*, Aromatic-H) ppm are attributed to the aromatic ring of the Schiff base moiety. The unaccounted and unintegrated signals are due to the solvent (See **Fig. A4**).

Upon quartenization of complex **5** to form complex **6**, ^{1}H NMR spectrum showed additional peaks in the up field region of the spectrum with reference to complex **5**. A total of 48 protons: between 1.16-1.69 (m, 9*H*, Alkane-H), 1.77-2.31 (m, 8*H*, Alkane-H) and 2.69-3.83(m, 31*H*, Alkane-H) as multiplets that correspond to the dimethyl amino group of the Schiff base moiety and the propanesultone chain. Furthermore 4 protons resonating at 2.72 (s, 2*H*, Alkene-H) and 2.89 (s, 2*H*, Alkene-H) ppm as singlets correspond to the azomethine group. For complex **6**, 12 Pc macrocyclic proton signals resonating between 9.16 and 9.95 ppm and 16 aromatic protons, seen as multiplets at 7.04-8.34 were observed (See **Fig. A5**).

The FT-IR spectra of **3**, **4**, **5** and **6** show characteristic Schiff base stretching bands at 1601,1600 and 1594, 1600 cm^{-1}, respectively, **Fig. 3.2A** and **3.2B**. The Ar-CH–C=N stretch range for 4-dimethyl amino benzaldehyde in complexes **3**, **4**, **5** and **6** moved from 2893-2680 cm^{-1} to 3329-3186 cm^{-1} for **6** and **5** and 3076-2926 for **4** and **3** indirectly indicating successful attachment of 4-dimethyl amino-benzaldehyde to the Pc complexes. These bands are characteristic of the azomethine moiety of most Schiff base compounds. The linking is also confirmed by the disappearance of $–NH_2$ functional groups from complexes **3b** and **5b** to form complexes **3** and **5**, respectively, **Fig. 3.2A** and **3.2B**. The absence of the C=O peak from the 4-dimethylamino benzaldehyde that is replaced by a C=N double bond band in complexes **3**, **4**, **5** and **6** indicates that the condensation has occurred.

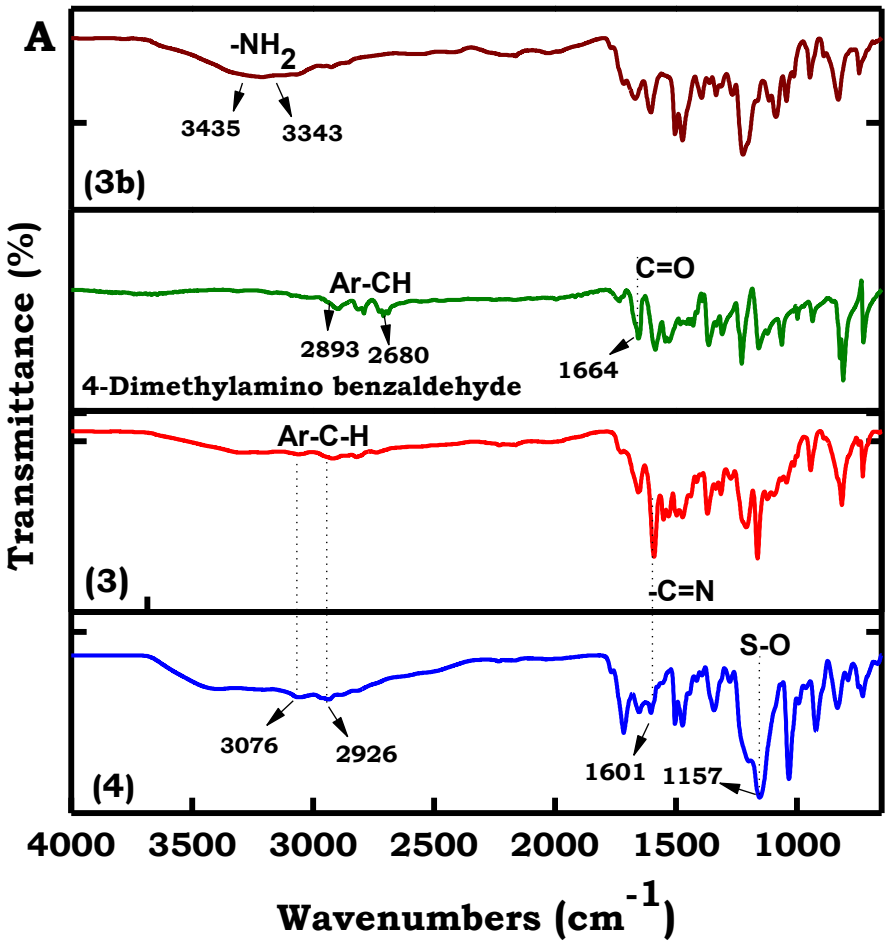

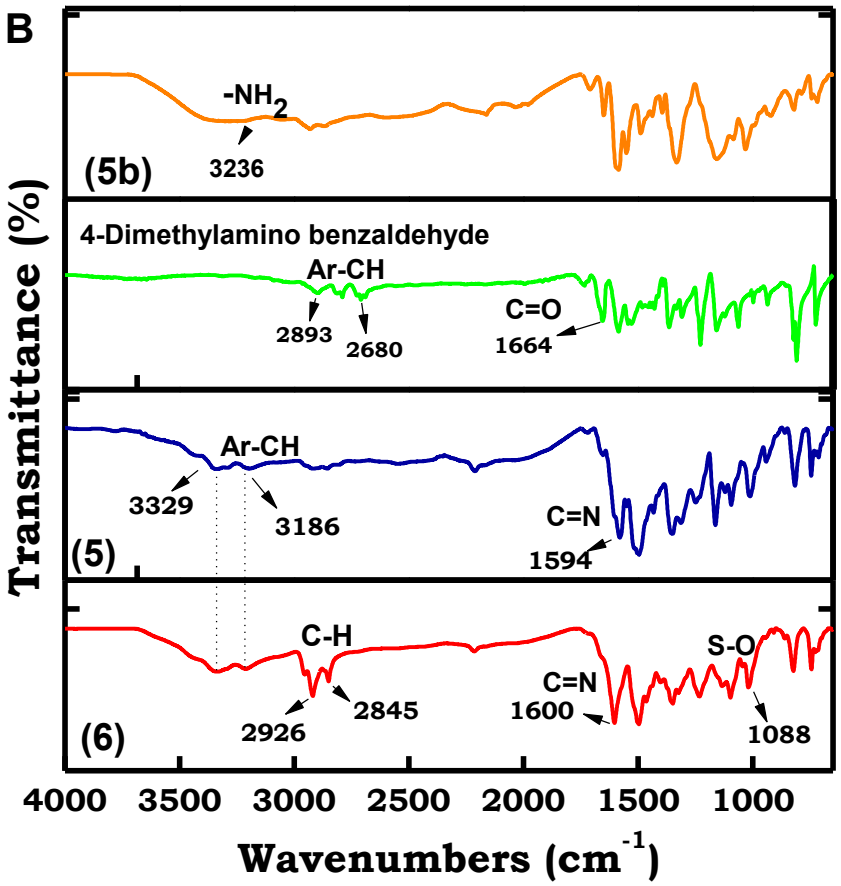

Fig. 3.2: FT–IR spectra of complexes (A) 3b, 3 and 4 and (B) 5b, 5 and 6.

Uv-vis spectra, **Table 3.1** of complexes **3**-**6** have red shifted Q-bands compared to **1** and **2** due to the large central metal InCl compared to Zn [119], the quartenised complexes **4** and **6** have blue shifted Q-band maxima compared to their unquaternised analogues complexes **3** and **5** respectively since nitrogen is engaged in complexes **4** and **6** [119], nitrogen groups are known for red shifting of the Q-band.

Table 3.1 Pcs alone and their conjugates with NPs in DMSO

MPc[a]	loading (mg(Pc)/mg (conjugate))	Q band maxima
1	-	679
1-AgNPs-GSH	0.14	680
1-Ag@Fe_3O_4 NPs-GSH	0.11	679
1-SiNPs-APTES	0.13	679
1-Ag@Fe_3O_4-SiNPs-APTES	0.1	680
2	-	680
2- AgNPs-GSH	0.25	682
2- Ag@Fe_3O_4NPs-GSH	0.17	681
2- SiNPs-APTES	0.09	681
2- Ag@Fe_3O_4-SiNPs-APTES	0.13	681
3		699
3-Ag@Fe_3O_4 NPs	0.31	697
3-Ag-Fe_3O_4 NPs	0.36	696
4		690
4-Ag@Fe_3O_4 NPs	0.67	690
4-Ag-Fe_3O_4 NPs	0.41	690
5		743
5-Ag@Fe_3O_4 NPs	0.20	744
5-Ag-Fe_3O_4 NPs	0.23	744
6		735
6-Ag@Fe_3O_4 NPs	0.32	735
6- Ag-Fe_3O_4 NPs	0.32	738

Note: "@" represents core shell

"-" represents dimer

3.2 Synthesis of NH_2 modified NPs and conjugation to 1 and 2.

The NPs employed in this work are those capped with APTES and GSH (**Tables 3.1** and **3.2**) hence contain NH_2 groups. The syntheses of GSH capped AgNPs [109], SiNPs-APTES [110] and OLA/OLM capped core shell Ag@Fe_3O_4 NPs [65,108] have been reported elsewhere. The presence of the loosely bound OLA/OLM on the surface of Ag@Fe_3O_4 NPs allows for ligand exchange of these capping ligands with molecule such as GSH which have a strong anchoring chemical moiety (thiol) which has a stronger affinity for Ag@Fe_3O_4 NPs surface compared to OLA/OLM, **Scheme 3.4**.

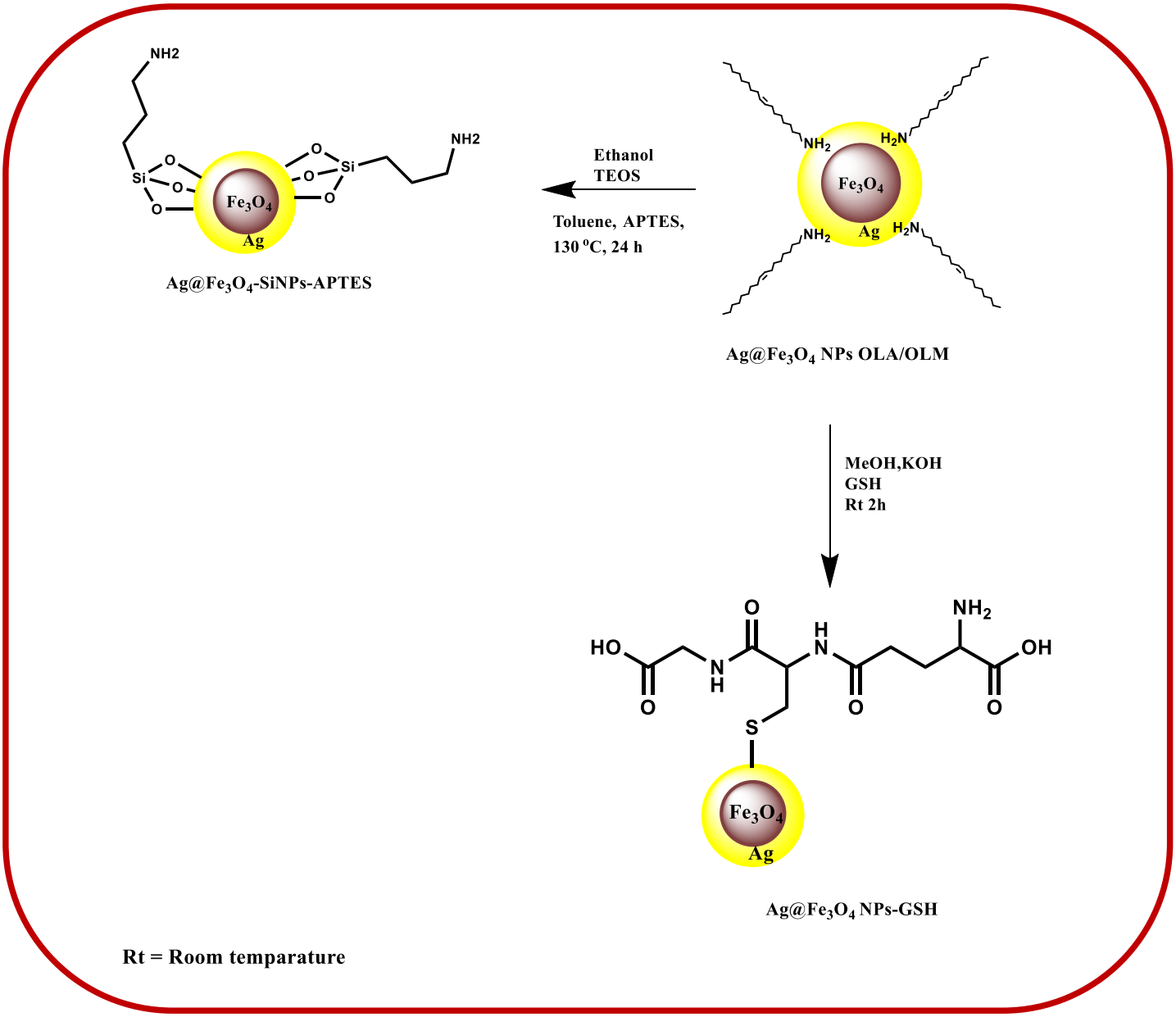

Scheme 3.4: Synthesis of Ag@Fe_3O_4 NPs-GSH and Ag@Fe_3O_4-SiNPs-APTES. APTES = (3-Aminopropyl) triethoxysilane, GSH = Glutathione, TEOS = Tetraethyl orthosilicate.

Silica coating Ag@Fe_3O_4 NPs was performed according to the literature [66] whereby the adsorbed OLA/OLM on Ag@Fe_3O_4 NPs were used as a template for the silica shell synthesis because of the hydrophobicity of TEOS,

Scheme 3.4. The resulting NPs are represented as Ag@Fe_3O_4–SiNPs-APTES. Complexes **1** and **2** were separately linked to NPs using DCC/DMAP as carboxylic acid activator for the former, **Scheme 3.5**. The conjugates are represented as **1**-AgNPs-GSH, **1**-Ag@Fe_3O_4 NPs-GSH, **2**-AgNPs-GSH and **2**-Ag@Fe_3O_4 NPs-GSH for GSH capped and as **1**-SiNPs-APTES, **1**-Ag@Fe_3O_4-SiNPs-APTES, **2**-SiNPs-APTES and **2**-Ag@Fe_3O_4-SiNPs-APTES for APTES capped. The nanoparticles and conjugates obtained were purified and characterised by FT-IR, UV-Vis, XRD and EDX spectroscopy and TEM.

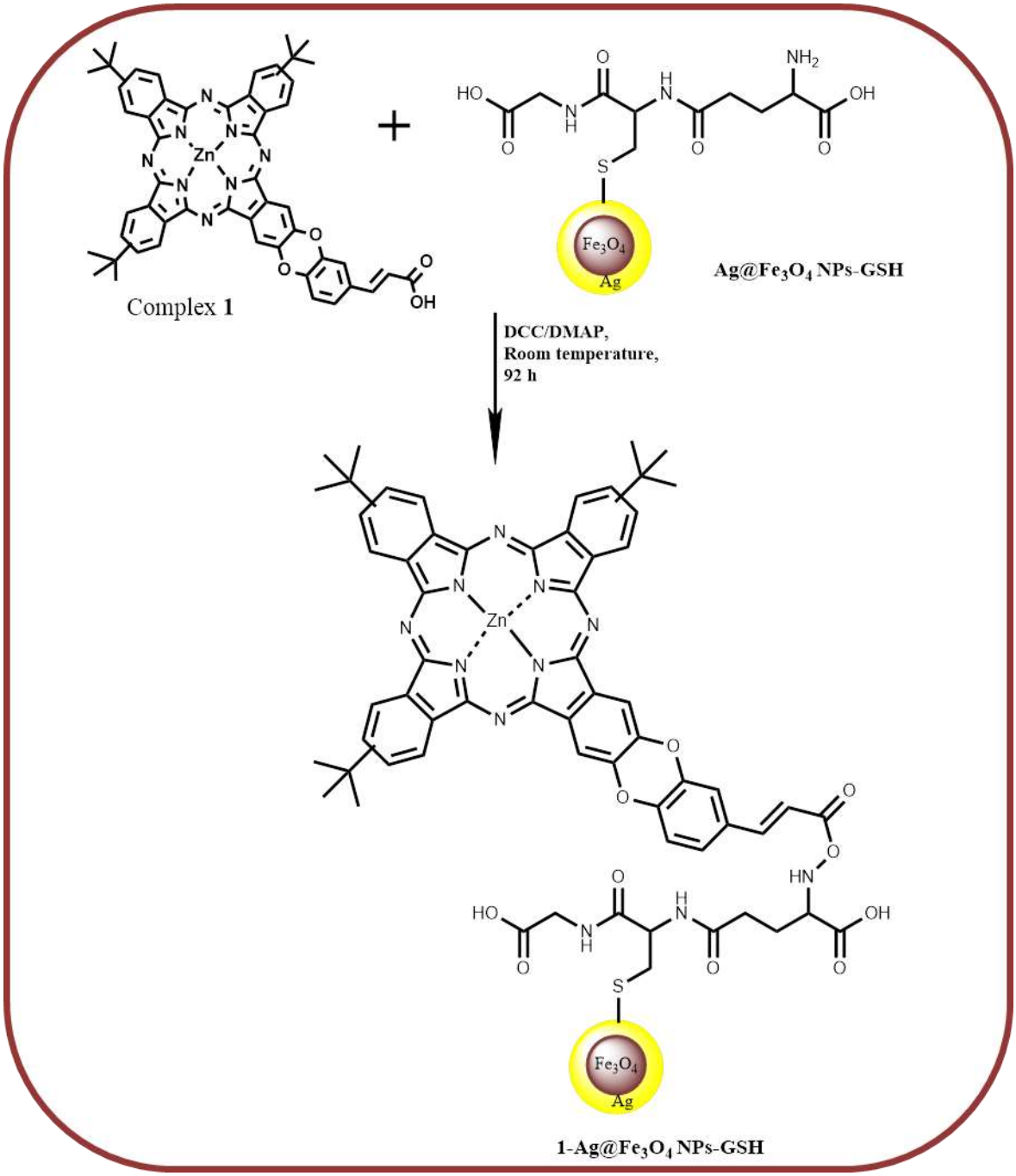

Scheme 3.5: Synthetic pathway for linkage of complex 1 to Ag@Fe_3O_4NPs-GSH. The same method was repeated for the linkage of AgNPs-GSH, Ag@Fe_3O_4-SiNPs-APTES and SiNPs-APTES. DMAP = 4-dimethylaminopyridine (DMAP), DCC = dicyclohexylcarbodiimide.

3.2.1 FT-IR Spectra.

The IR spectrum of complex **1** (as an example) shows the presence O-H at 3500 cm^{-1}, C-H at 2965 cm^{-1}, and (C=O) at 1699 cm^{-1}(**Fig. 3.3**). The carbonyl and the alcohol vibrational bands observed for complex **1** are attributed to the caffeic acid substituent of the Pc and the C-H band is primarily due to the Pc macrocycle. The appearance of siloxane (1053 cm^{-1}) from silica coating in the IR spectrum indicate the successful doping of the Ag@Fe_3O_4 NPs core with SiNPs and the presence of the NH confirms the functionalization of the composites with APTES. Additionally, the appearance of amide HN–C=O- at 1654 cm^{-1} serves as a plausible indication for successful formation of the **1**-Ag@Fe_3O_4-SiNPs-APTES conjugates via amide bond. On the other hand, the GSH capped NPs showed vibrational bands at 1642 cm^{-1} and 1570 cm^{-1} corresponding to amide C=O and N-H respectively while the conjugate of the GSH capped NPs and Pc complexes depicted their amide C=O and N-H at 1727 cm^{-1} and 1630 cm^{-1} using **1**–Ag@Fe_3O_4NPs–GSH, **Fig. 3.3**. Chemical shifts in the IR vibrational bands of complexes confirm structural change or formation of a new compound [120].

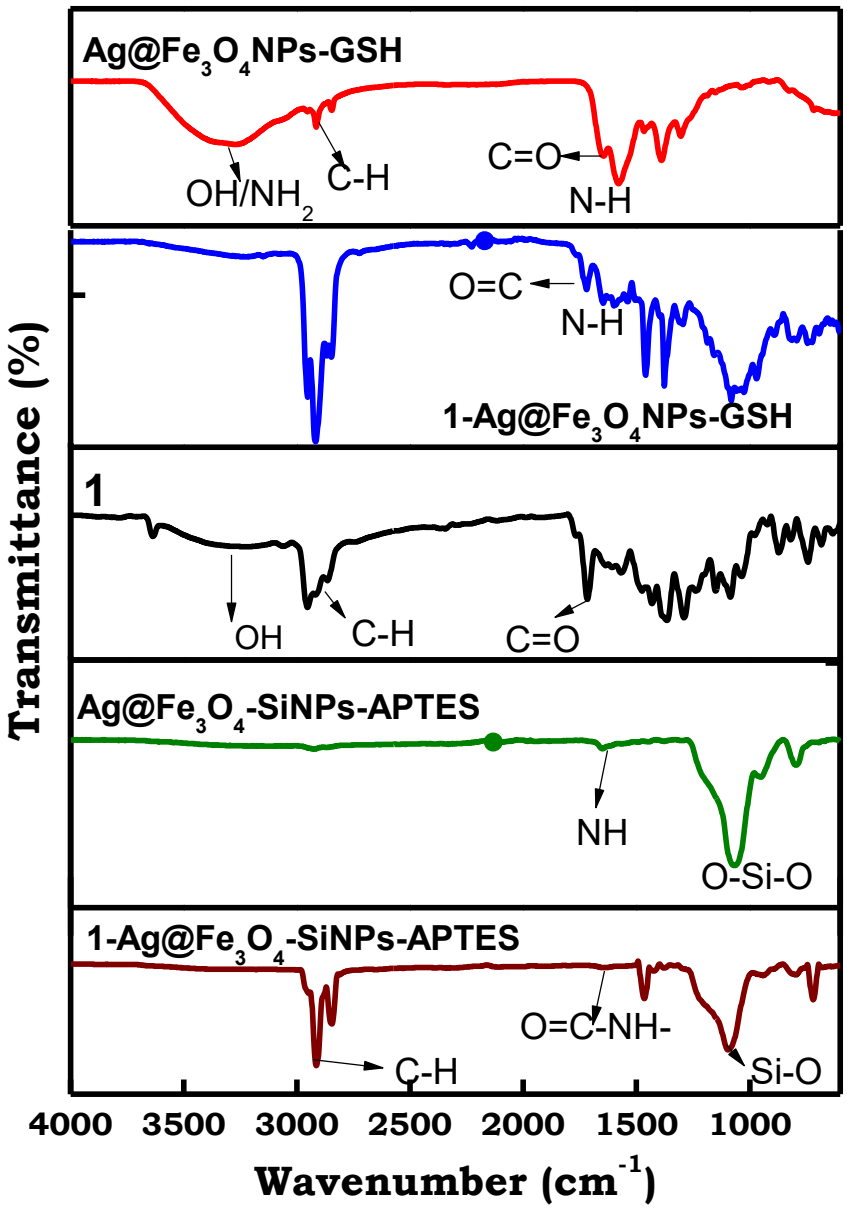

Fig. 3.3: FT–IR spectra of complex 1 and its conjugates with NPs.

3.2.2 UV-Vis spectra.

The normalised UV-visible spectra of Ag@Fe_3O_4NPs-GSH and Ag@Fe_3O_4-SiNPs-APTES measured in ethanol and AgNPs-GSH in water are shown in **Fig. 3.4A**. A clear and intense surface plasmon resonance (SPR) peak of AgNPs-GSH was observed at 421 nm, **Table 3.2**. The UV-vis spectra of Ag@Fe_3O_4-SiNPs-APTES and Ag@Fe_3O_4NPs-GSH showed a broad band at ~380 nm which could be attributed to Fe_3O_4NPs band but no definite SPR band was observed for AgNPs in the composites [121], **Table 3.2**. Upon conjugation of complex **1** (as an example) to the nanoparticles there was no change in the Q band of complexes **1** or **2** alone, **Fig. 3.4B**, **Table 3.1**. However, there was a significant increase in the absorption of the Pc complexes at ≤600 nm on conjugation with NPs especially for **1**-Ag@Fe_3O_4-SiNPs-APTES as an example.

The number of Pc molecules bonded to the NPs were determined as explained before [122], using absorption instead of fluorescence. Equal masses (mg) for Pc and conjugates were weighed and separately dissolved in the same volume of solvent. This was followed by comparing the Q band absorbance intensity of the Pc in the conjugate with that of the initial Pc before the conjugation. The ratios of Pcs to NPs are listed in **Table 3.1**. With the exception of **1**-SiNPs-APTES, there is more loading of **2** than **1** on the corresponding NPs, this could be due to the bulkier nature of the latter that allows less Pcs loading onto the NPs.

Table 3.2 Absorption and size distribution of NPs synthesised in this work.

NPs	Size nm (TEM)	Linked to	Bond type	Solvent	UV-Vis spectrum band (nm)
AgNPs-GSH	17	**1**, **2**	amide	Water	421
Ag@Fe_3O_4 NPs-GSH	21	**1**, **2**	amide	Ethanol	~380
Ag@Fe_3O_4-SiNPs-APTES	22	**1**, **2**	amide	Ethanol	~380
SiNPs-APTES	47	**1**, **2**	amide	Ethanol	No band
Ag-Fe_3O_4 OLA/OLM	31	**3-6**	Ag to N	Chloroform	426
Ag@Fe_3O_4 OLA/OLM	9	**3-6**	Ag to N	Chloroform	421

Note: "@" represents core shell

"-" represents dimer

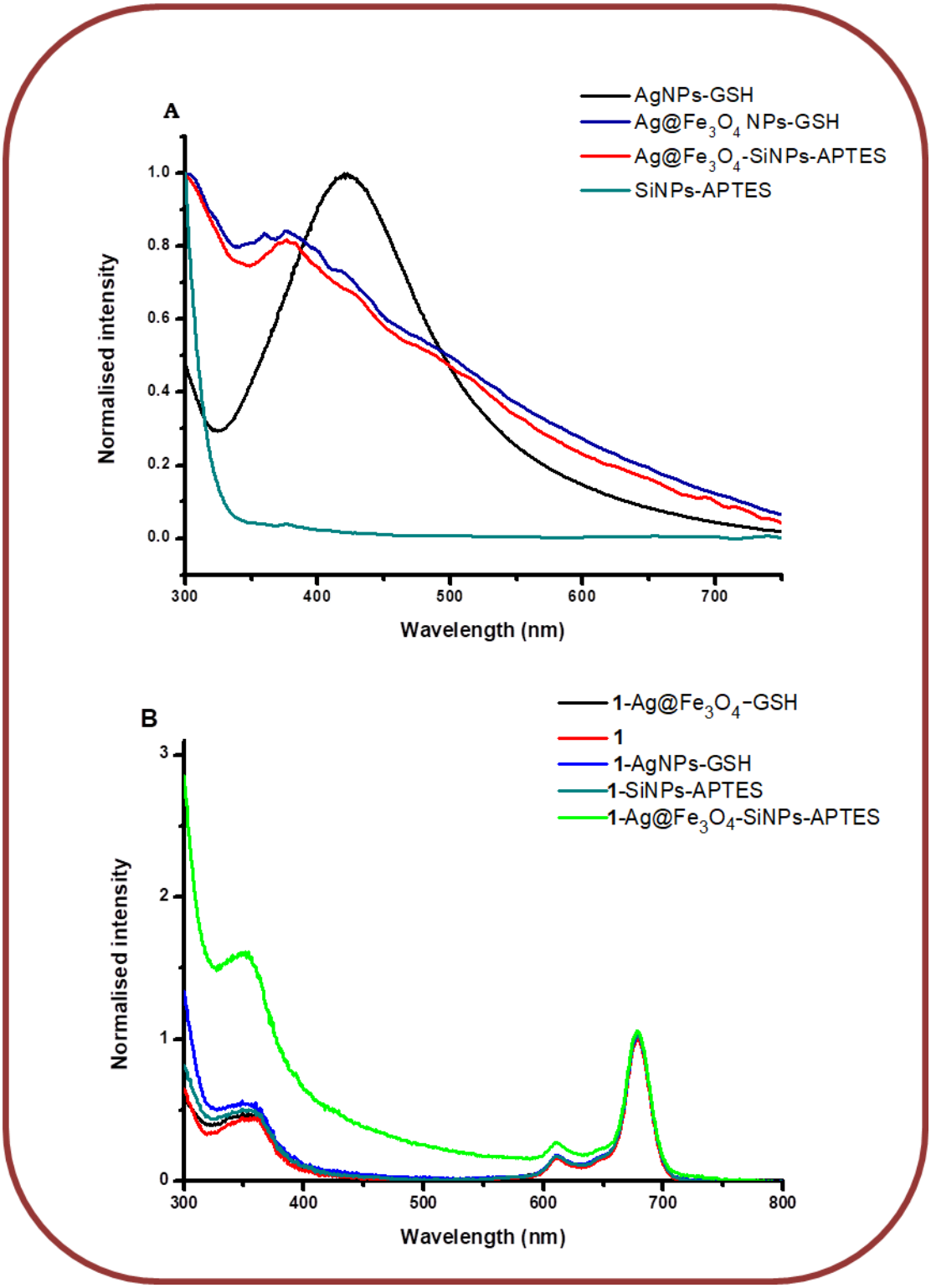

Fig. 3.4: Normalised UV-visible absorption spectra for AgNPs-GSH (in water), SiNPs-APTES, Ag@Fe_3O_4-SiNPs-APTES and Ag@Fe_3O_4NPs-GSH in ethanol (A) and their conjugates (B) with complex 1 in DMSO.

3.2.3 XRD.

The morphology and the sizes of the NPs and their conjugates with Pcs were assessed by X-ray diffractometer (**Fig. 3.5**). The broad pattern observed for complexes **1** and **2** (**Fig. 3.5**, using **1** as an example) are typical of phthalocyanines due to their amorphous nature [123]. SiNPs-APTES alone and all the conjugates containing SiNPs-APTES also showed amorphous nature (figures not shown). Fe_3O_4 alone are known [122] to have a face-centered cubic structure with diffraction peaks at 2θ = 30°, 36°, 43°, 54°, 57° and 63°, corresponding to plane at 220, 311, 400, 422, 511 and 440, respectively (figure not shown). The Bragg's reflections of pure crystalline silver are positioned at 2θ = 38.40° (111), 44.61° (200), 64.81° (220), 78.20° (311) and 82.10° (222), **Fig. 3.5**. The peaks present in Ag@Fe_3O_4–SiNPs-APTES and Ag@Fe_3O_4-GSH are a combination of the component peaks. The peaks for the NPs are present in the conjugates though weak. The sharp peaks could reflect crystallinity and increase in size.

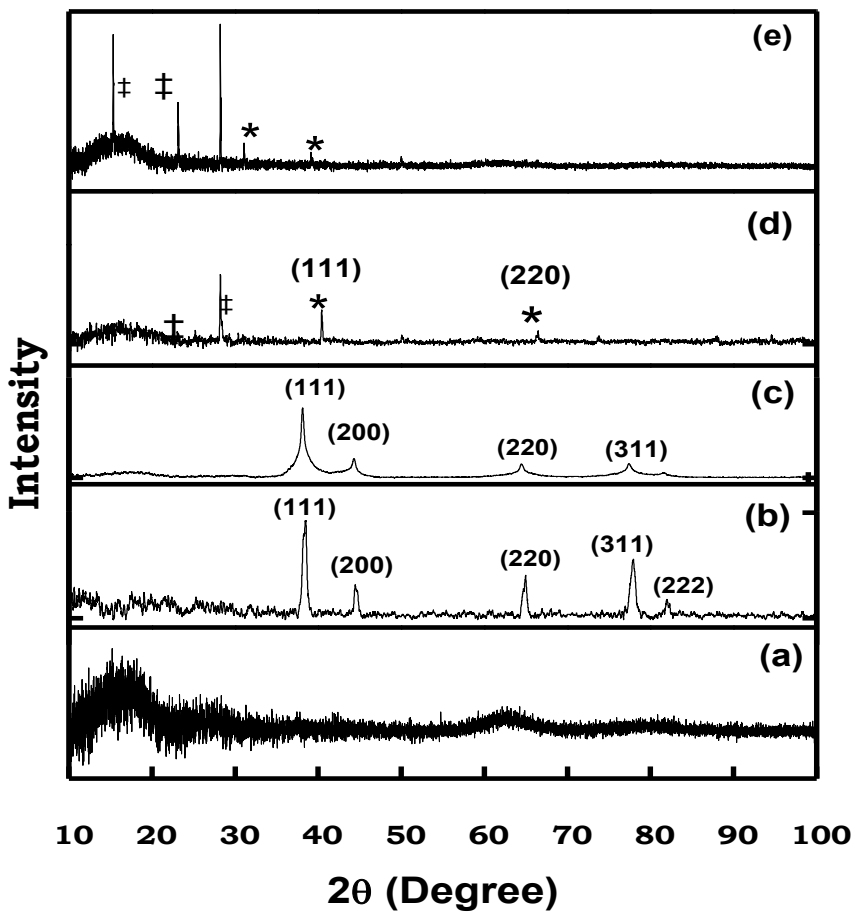

Fig. 3.5: XRD diffractograms of (a) complex 1, (b) AgNPs-GSH, (c) 1-AgNPs-GSH, (d) Ag@Fe_3O_4-SiNPs-APTES and (e) 1-Ag@Fe_3O_4-SiNPs-APTES with reflection peaks for Fe_3O_4 (‡) and Ag (*) where the former and latter are present in the composites (Ag@Fe_3O_4).

3.2.4 TEM and EDX analyses.

The transmission electron microscope (TEM) was used to assess the morphologies of AgNPs-GSH, SiNPs-APTES and Ag@Fe_3O_4–SiNPs-APTES as examples in **Fig. 3.6**. The TEM micrograph for AgNPs-GSH showed polydispersed particles with an average size of 17 nm, **Table 3.2**. SiNPs-APTES were also relatively polydispersed with an average size of 47 nm. Ag@Fe_3O_4-SiNPs-APTES showed considerable aggregation due to the

paramagnetic nature of iron. The sizes of Ag@Fe_3O_4–SiNPs-APTES and Ag@Fe_3O_4-GSH were estimated to be 22 nm and 21 nm, respectively, **Table 3.2**. Following conjugation of NPs to complexes **1** and **2**, extensive aggregation was observed in the TEM micrographs. Interactions between the Pcs on adjacent NPs via π-π stacking may occur leading to aggregation since MPcs are known to form the so-called H aggregates [124].

EDX was used to qualitatively determine the elemental composition of the NPs using Ag@Fe_3O_4–SiNPs-APTES and Ag@Fe_3O_4-GSH as examples in **Fig. 3.7.** Expected elements were observed in both cases, the presence of potassium (**Fig. 3.7A**) is due to the potassium hydroxide that was used during the modification of Ag@Fe_3O_4NPs surface with GSH, while the chlorine peak is a trace element of ferric chloride that is used in the synthesis of Fe_3O_4 magnetic nanoparticles. Additionally, the observed sulphur peak (**Fig. 3.7B**) is due to the ferrous sulphate used in the synthesis of Fe_3O_4 nanoparticles.

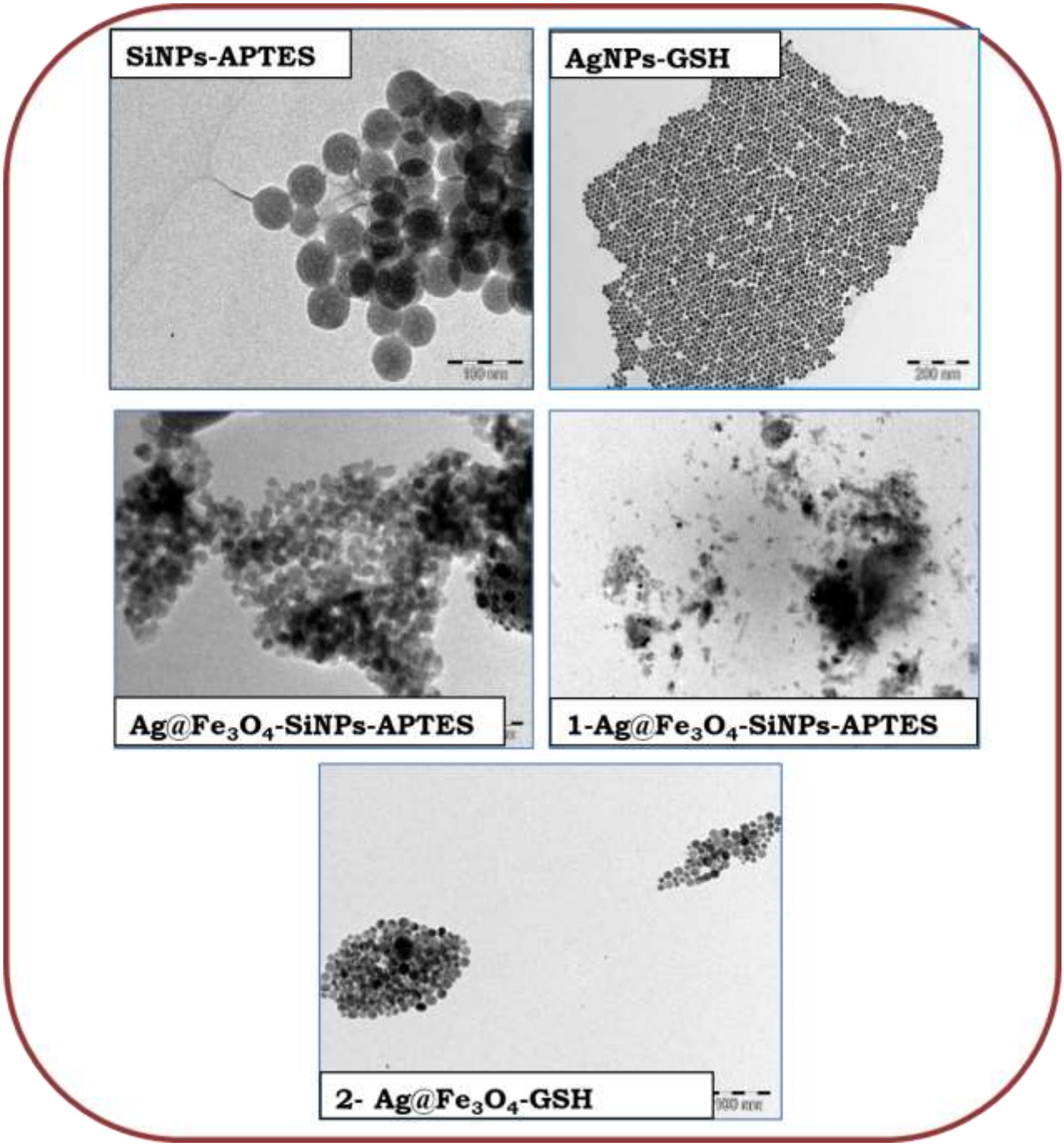

Fig. 3.6: TEM micrographs for SiNPs-APTES, AgNPs-GSH , Ag@Fe_3O_4-SiNPs-APTES , 1-Ag@Fe_3O_4-SiNPs-APTES and 2- Ag@Fe_3O_4-GSH.

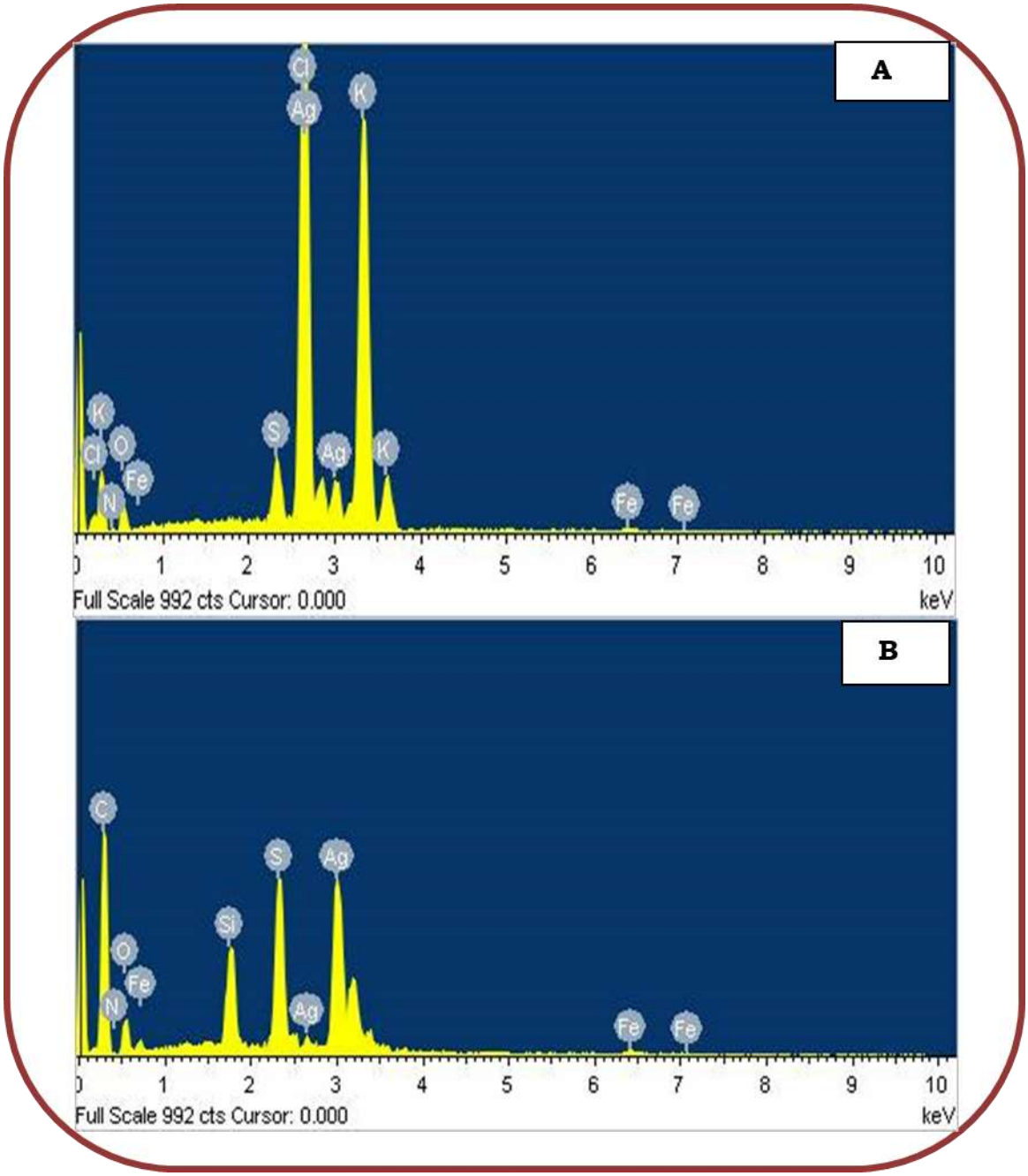

Fig. 3.7: EDX spectra of Ag@ Fe_3O_4-GSH (A) Ag@Fe_3O_4-SiNPs-APTES (B).

3.3 Ligand exchange of complexes 3-6 with OLA/OLM on Ag-Fe_3O_4 and Ag@Fe_3O_4 NPs.

The syntheses of OLA/OLM capped Ag-Fe_3O_4-dimer NPs and Ag@Fe_3O_4-core shell NPs was carried out as described in literature [107] and [65,108], respectively, and the NPs are represented in **Scheme 3.6**. The attachment of the phthalocyanines onto the surface of the nanoparticles was carried out using ligand exchange, where the loosely bound OLA/OLM ligands were partially replaced by Pcs that bind to the surface of nanoparticles **Scheme 3.6**. The nitrogen group on the Pc ring substituents were used to attach the phthalocyanine complexes onto the Ag part of the nanoparticles due to the affinity of silver for nitrogen atoms. It is possible that some OLA/OLM was not replaced as represented in **Scheme 3.6**. The nanoparticles and conjugates obtained were purified and characterized by UV-Vis, XRD and EDX spectroscopy and TEM.

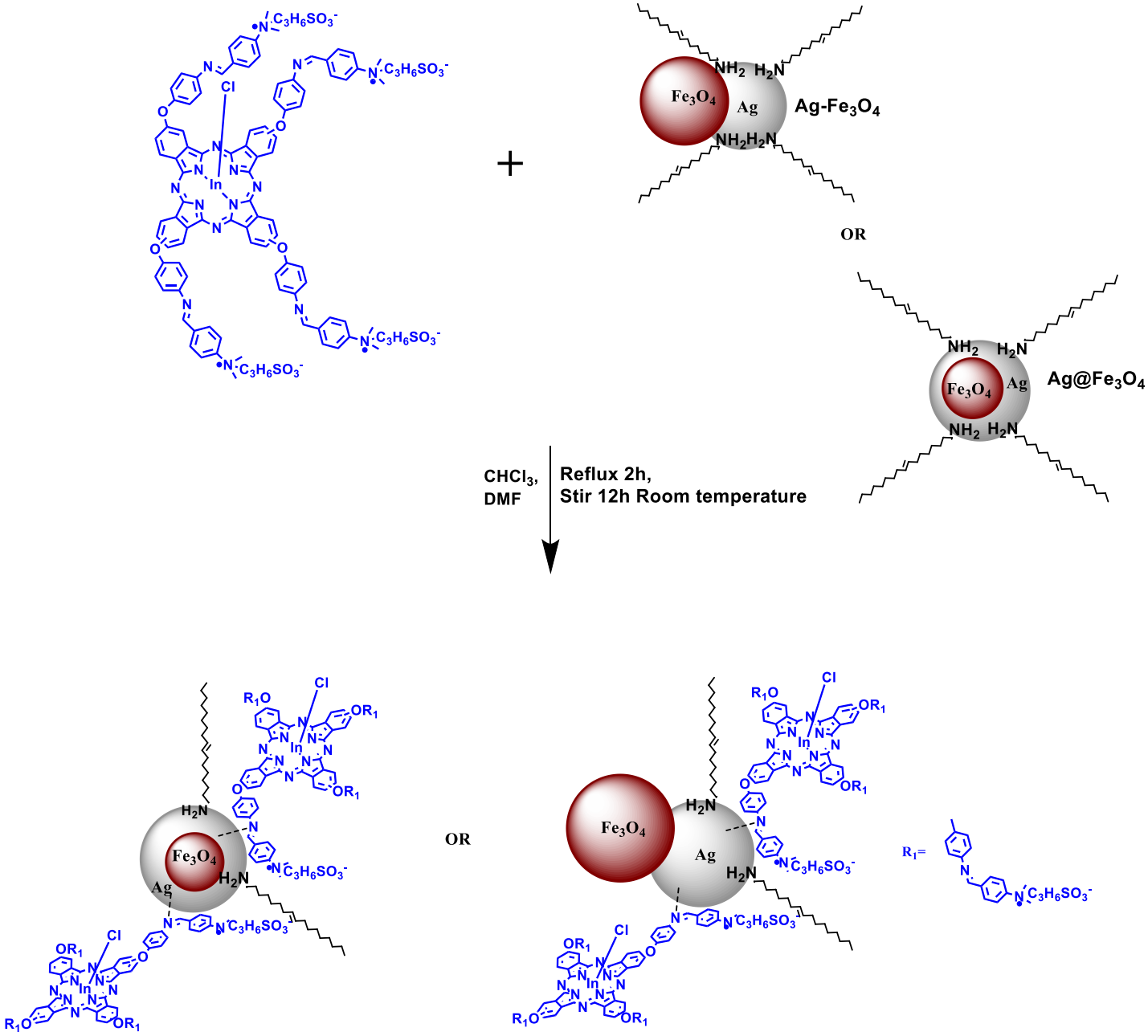

Scheme 3.6: Schematic illustration of synthetic route for complex 4 functionalized with to Ag-Fe_3O_4-dimers/ Ag-Fe_3O_4-core shell nanoparticles.

3.3.1 UV/Vis absorption spectra

Fig. 3.8A shows a UV–Vis spectrum of OLA/OLM capped Ag-Fe_3O_4 and Ag@Fe_3O_4-nanoparticles and their conjugates with complex **4** (as an example). The surface plasmon resonance (SPR) bands for the Ag-Fe_3O_4 OLA/OLM and Ag@Fe_3O_4 OLA/OLM NPs alone were observed at 426 and 421 nm, **Table 3.2** respectively. Upon conjugation the SPR peaks for **4**-Ag-Fe_3O_4-dimer NPs and **4**-Ag@Fe_3O_4-core shell NPs were not clearly defined, but there is an enhancement in absorption in the area of the SPR bands. There were no significant shifts in the Q bands of the phthalocyanines on linking to the NPs (**Table 3.1, Fig. 3.8B**), except for **6**-Ag-Fe_3O_4 and **3**-Ag-Fe_3O_4 where there are red and blue shifts, respectively.

The loading values were determined as stated above and are shown in **Table 3.1**. The highest loading was observed for **4** and the lowest for **5**, this is due to the availability of sulfur atoms present in complex **4**, both nitrogen and sulfur are able to bind with silver this causes an increased uptake of NPs. However this was not observed for complex **6**, which also has nitrogen and sulfur.

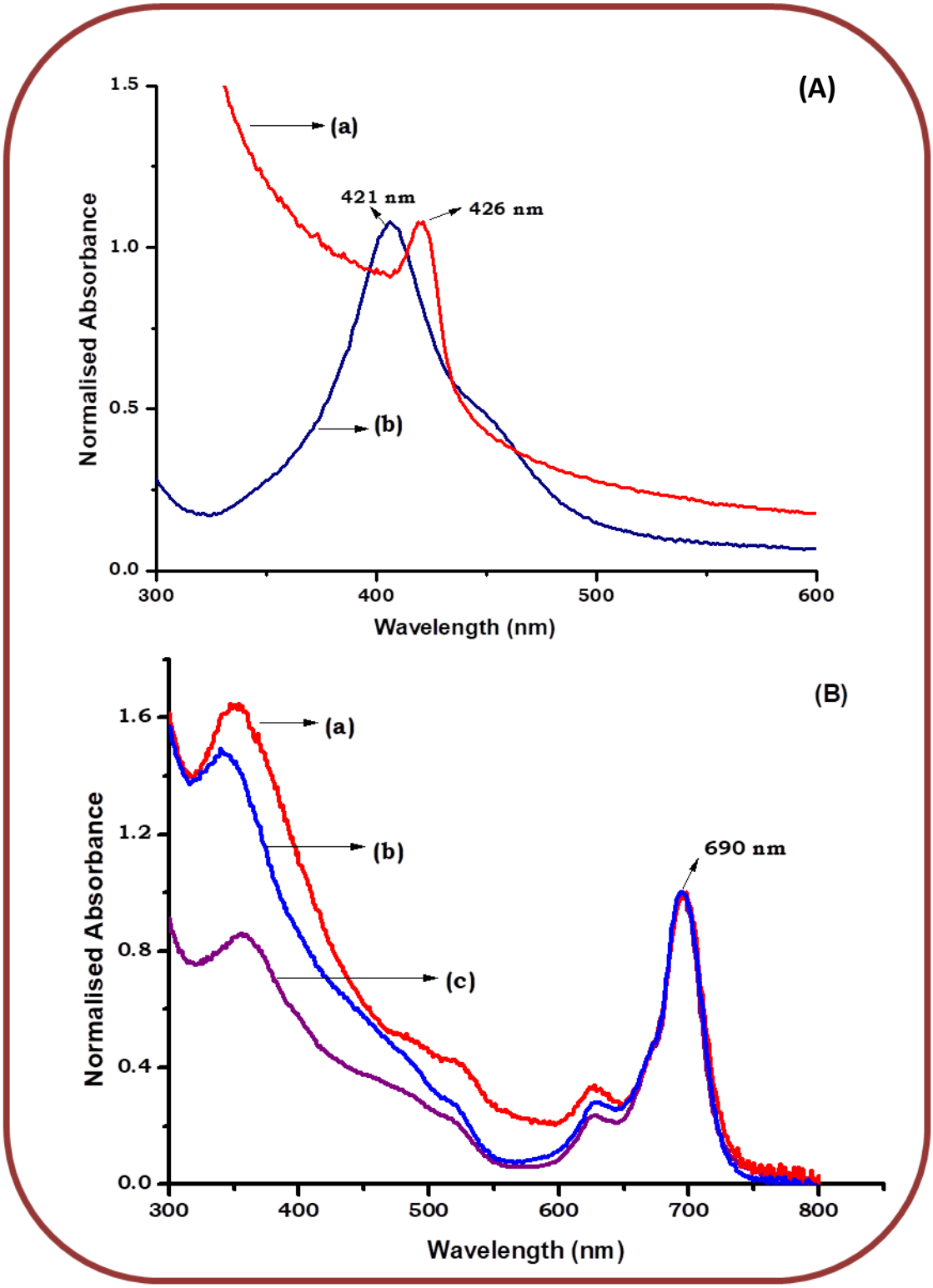

Fig. 3.8: Absorption spectra of (A) Ag-Fe_3O_4 OLA/OLM NPs (a) and Ag@Fe_3O_4 OLA/OLM NPs (b), and (B) 4-Ag-Fe_3O_4 NPs (a), 4-Ag@Fe_3O_4 NPs (b) and complex 4 (c). Normalized at 690 nm.

3.3.2 XRD studies.

The morphologies of Ag@Fe_3O_4 OLA/OLM, Ag-Fe_3O_4 OLA/OLM NPs and their conjugates (using **4** as an example) were assessed using X-ray diffraction (XRD), **Fig. 3.9**. The XRD diffraction patterns of the Ag@Fe_3O_4 OLA/OLM NPs showed well-defined crystalline peaks assigned to 111, 200, 220 and 311 planes ICSD (98487), PDF No(00-021-1080), at $2\theta = 38.2^{\circ}$, 44.4°, 64.7° and 77.3° for Ag only, respectively, **Fig. 3.9b**. These correspond to the face centered-cubic structure of metallic silver for Ag@Fe_3O_4 OLA/OLM NPs. Similar crystalline peaks were also assigned to the 111 and 200 planes for Ag-Fe_3O_4 OLA/OLM NPs but these were slightly shifted compared to the Ag@Fe_3O_4 OLA/OLM NPs crystalline planes at $2\theta = 39.1^{\circ}$ and 46.8° [125]. The peaks that are characteristic of silver assigned to 220 and 311 were not observed for Ag-Fe_3O_4 OLA/OLM NPs (**Fig. 3.9d**) and **4**-Ag-Fe_3O_4 OLA/OLM NPs (**Fig. 3.9e**), this is attributed to amorphous nature of the Fe_3O_4, that accounts for a larger surface of the Ag-Fe_3O_4NPs. The XRD diffraction pattern of complex **4** alone show broad peak between $2\theta = 12°$ to 28° in **Fig. 3.9a**, typical of the amorphous nature of Pcs [123,126]. Upon conjugation NPs were observed at 38.3°, 45.2°, 64.5° and 78.6° for **4**-Ag@Fe_3O_4 OLA/OLM NPs, **Fig. 3.9c**, and 40.5° and 47.8° for **4**-Ag-Fe_3O_4 OLA/OLM NPs, **Fig. 3.9e** which provides evidence for the presence of both nanoparticles and complex **4**.

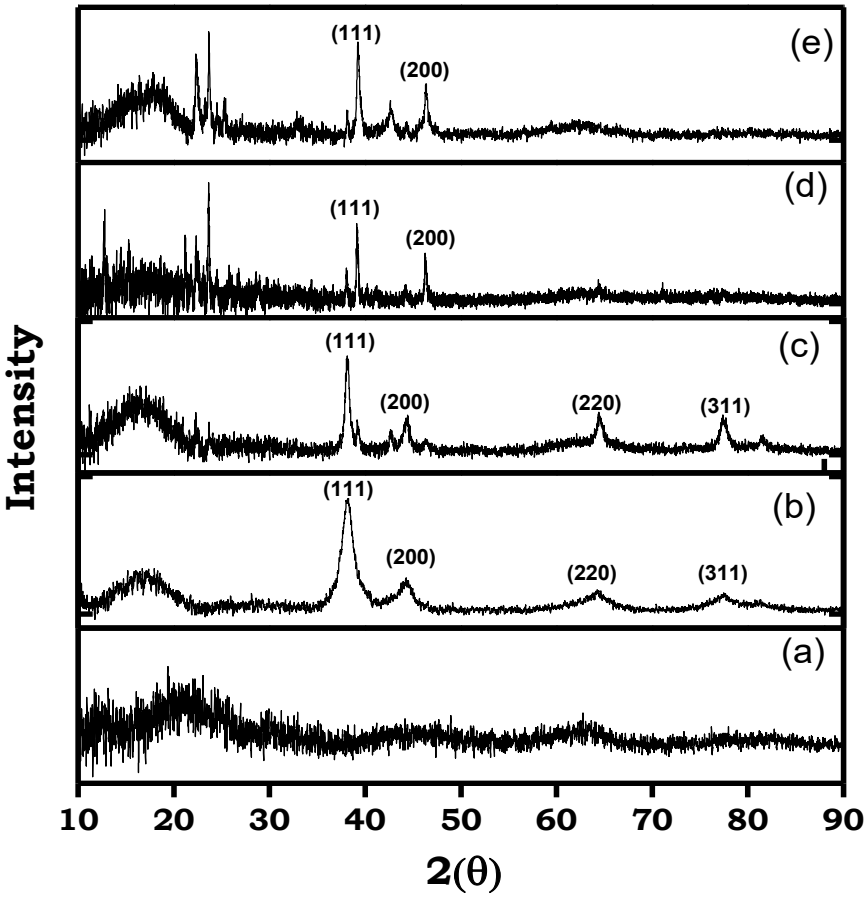

Fig. 3.9: XRD diffractograms of (a) complex **4**, (b) Ag@Fe_3O_4 OLA/OLM NPs, (c) **4**-Ag@Fe_3O_4 NPs, (d) Ag-Fe_3O_4 OLA/OLM NPs, (e) **4**-Ag-Fe_3O_4 NPs.

3.3.3 EDX and TEM images

Energy dispersive X-ray (EDX) spectra were used to qualitatively determine the elemental compositions of the Ag@Fe_3O_4NPs and all the expected elements from the nanoparticles were observed (**Fig. 3.10**). The transmission electron microscopy (TEM) was used to assess the morphologies of Ag-Fe_3O_4 OLA/OLM NPs, Ag@Fe_3O_4 OLA/OLM NPs in **Fig. 3.11**. The TEM micrographs of the Ag-Fe_3O_4NPs showed monodispersed dimer-like particles [127] with an average size distribution of 31 nm, **Table 3.2**. Upon conjugation to the MPcs, using complex **4** as an example, aggregation was observed in the TEM micrograph in **Fig. 3.11**. This can be attributed to the interactions between the Pcs on adjacent NPs via π-π stacking, leading to aggregation since MPcs are known to form the so-called H aggregates [124]. The Ag@Fe_3O_4NPs in **Fig. 3.11** showed monodispersed spherical particles with an average diameter of 9 nm, **Table 3.2** upon conjugation an increase in size of the nanoparticle to 16 nm and aggregation was observed.

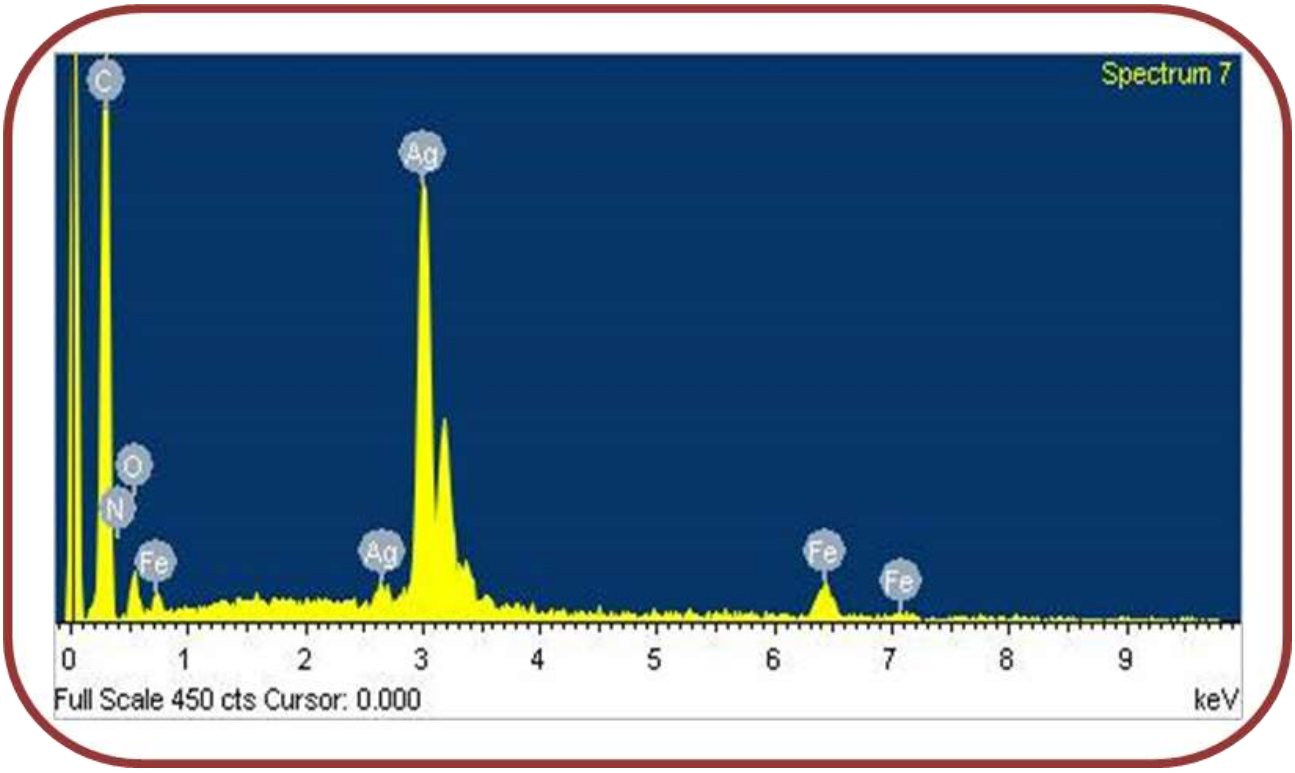

Fig. 3.10: EDX spectra of Ag@Fe_3O_4 OLA/OLM NPs.

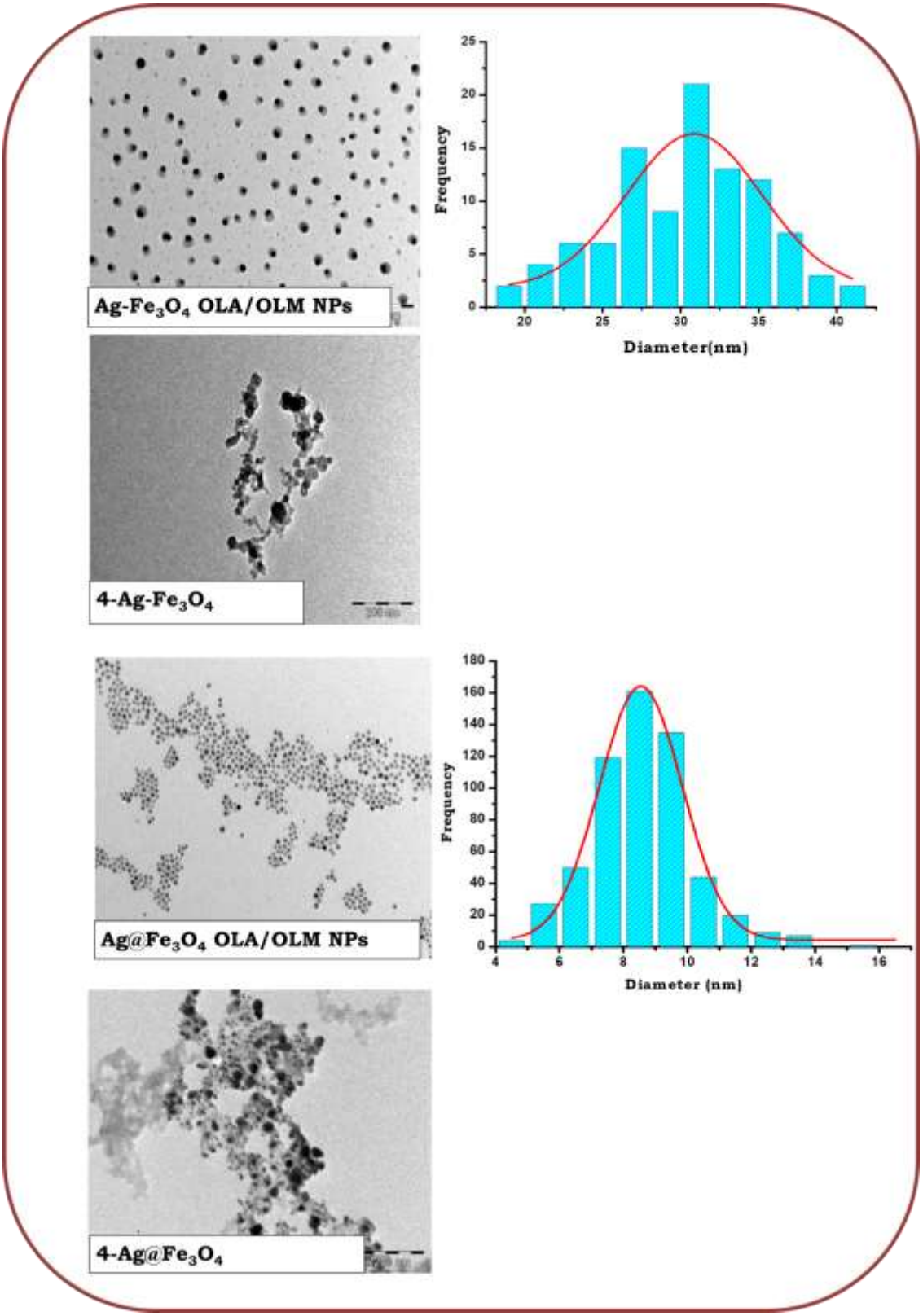

Fig. 3.11: TEM Micrographs of Ag-Fe_3O_4 OLA/OLM and Ag@Fe_3O_4 OLA/OLM NPs alone and after conjugation to complex 4.

3.4 Summary of chapter

Complexes **1** and **3**-**6** were synthesised and fully characterised using various techniques to determine structural composition of the metallophthalocyanines. The complexes with carboxylic groups were conjugated to nanomaterials that were functionalised with amino functionalised capping agents via amide bond. The conjugates of the symmetrical Pcs were linked to OLA/OLM capped NPs via chemisorption onto the surface of the nanoparticles. All the photosensitizers and their conjugates show monomeric absorbance behaviour in DMSO.

Chapter 4

Photophysico-chemical studies

In this chapter the photophysical and photochemical properties of the synthesised MPcs alone and in the presence of nanomaterial are discussed. It is expected that Pc-conjugates will show improved triplet state in comparison to their unconjugated Pc analogues, due to the heavy metals of the NPs in the former.

Table 4.1 Photophysical and Photochemical Studies of Phthalocyanines and their conjugates in DMSO.

MPc[a]	*loading (mg(Pc)/mg (conjugate))*	*Q band maxima*	Φ_F	$\tau_{F\ (ns)}$	Φ_T	τ_T (μs)	Φ_Δ
1	-	679	0.19	3.08	0.61	250	0.44
1-AgNPs-GSH	0.14	680	0.17	3.06	0.68	214	0.45
1-Ag@Fe_3O_4 NPs-GSH	0.11	679	0.03	2.84	0.72	240	0.42
1-SiNPs-APTES	0.13	679	0.17	2.85	0.66	278	0.41
1-Ag@Fe_3O_4-SiNPs-APTES	0.1	680	0.12	2.95	0.81	298	0.37
2	-	680	0.13	2.96	0.63	247	0.40
2- AgNPs-GSH	0.25	682	0.09	2.89	0.69	232	0.39
2- Ag@Fe_3O_4 NPs-GSH	0.17	681	0.11	2.87	0.78	241	0.38
2- SiNPs-APTES	0.09	681	0.10	2.93	0.67	226	0.43
2-Ag@Fe_3O_4-SiNPs-APTES	0.13	681	0.12	2.91	0.76	273	0.57
3		699	<0.01	<0.01	0.61	178	0.40
3-Ag@Fe_3O_4 NPs	0.31	697	<0.01	<0.01	0.88	151	0.59
3-Ag-Fe_3O_4 NPs	0.36	696	<0.01	<0.01	0.75	128	0.54
4		690	<0.01	<0.01	0.73	106	0.62
4-Ag@Fe_3O_4 NPs	0.67	690	<0.01	<0.01	0.81	171	0.68
4-Ag-Fe_3O_4 NPs	0.41	690	<0.01	<0.01	0.76	187	0.79

5		743	<0.01	<0.01	-a	-a	0.027
5-Ag@Fe_3O_4 NPs	0.20	744	<0.01	<0.01	-a	-a	0.13
5-Ag-Fe_3O_4 NPs	0.23	744	<0.01	<0.01	-a	-a	0.19
6		735	<0.01	<0.01	-a	-a	0.22
6-Ag@Fe_3O_4 NPs	0.32	735	<0.01	<0.01	-a	-a	0.26
6- Ag-Fe_3O_4 NPs	0.32	738	<0.01	<0.01	-a	-a	0.11

a-No signal

4.1 Fluorescence (Φ_F) quantum yields and lifetimes (τ_F).

Fluorescence quantum yields (Φ_F) were determined using equation **1.1** ZnPc in DMSO used as a standard with Φ_F = 0.20 [97]. The heavy atom effect of the nanoparticles promotes intersystem crossing to the triplet state by lowering the fluorescence quantum yield. Hence, all the Φ_F values for the conjugates were lower compared to the values obtained for complexes **1** and **2** alone. All the Φ_F values were less than 0.01 for complexes **3**-**6** and their conjugates due to the heavy atom effect of the indium central metal.

A typical fluorescence decay curve for conjugate **1**-Ag@Fe_3O_4 NPs-GSH is shown in **Fig. 4.1**. The τ_f values for the conjugates decreased as compared to the Pcs alone which is expected due to heavy atom effect, **Table 4.1**. The fluorescence lifetimes were also very low (< 0.01 ns) for **3**-**6** corresponding to low Φ_F values since the two are related.

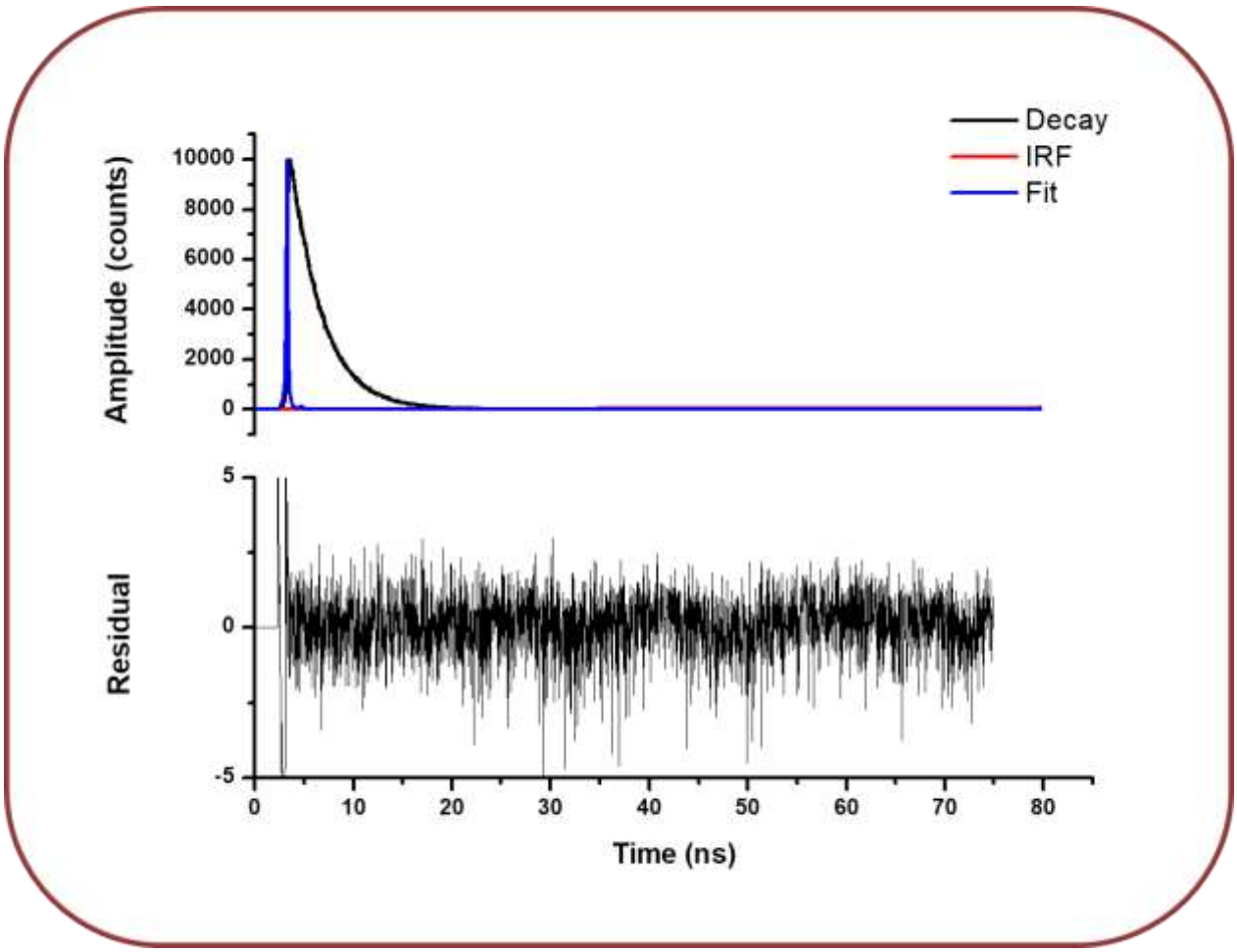

Fig. 4.1: Fluorescence of 1-Ag@Fe_3O_4-SiNPs-APTES.

4.2. Triplet quantum yields (Φ_T), lifetimes (τ_T).

Fig. 4.2 shows a typical transient curve for Pcs or Pcs conjugates using **4**-Ag@Fe_3O_4 NPs (as an example) with a triplet absorption maximum at 502 nm. The insert shows the triplet decay curve.

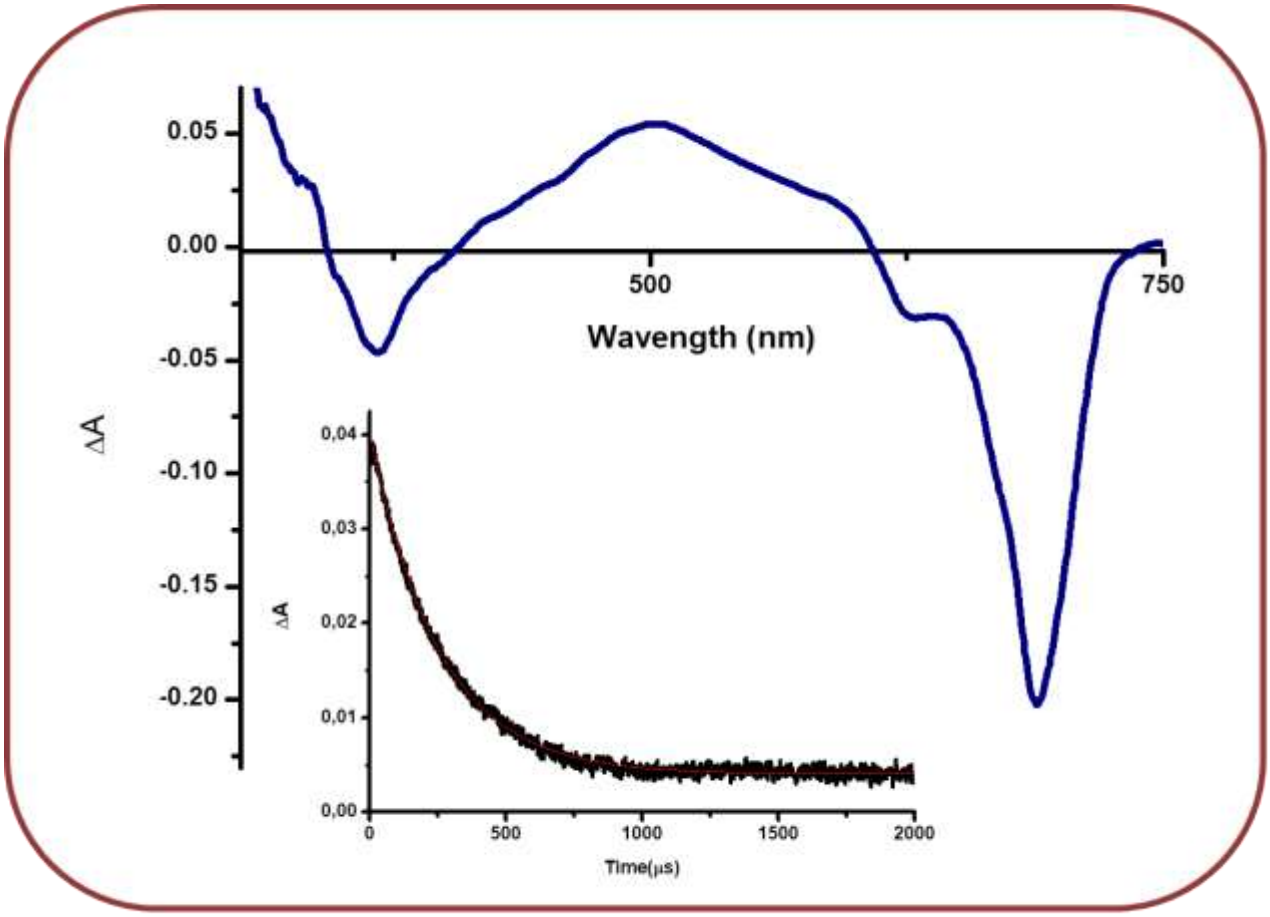

Fig. 4.2: Transient differential spectrum of 4-Ag@Fe_3O_4 NPs, excitation wavelength at 681 nm. Insert is the corresponding triplet decay curve.

The Φ_T was determined using equation **1.2**. The standard employed for the Φ_T determination was unsubstituted ZnPc in DMSO with Φ_T value of 0.65 [100]. The Φ_T values for ZnPc complexes **1** and **2** were relatively similar, hence no significant effect of the Pc ring substituent. Φ_T and Φ_F are

complementary processes, where the former is larger the latter should be smaller. There is an increase in Φ_T values where Φ_F values decreased for ZnPc complexes **1**, **2** and their conjugates, **Table 4.1**. Thus in the presence of NPs, Φ_T values increase since the NPs encourage intersystem crossing to the excited triplet state. In all the cases, single component NPs (**1**-SiNPs-APTES, **1**-AgNPs-GSH, **2**-SiNPs-APTES, and **2**-AgNPs-GSH) gave lower values as compared to the mixed composites but higher than the Pcs alone. This shows the importance of mixed NPs rather than individual ones for applications. A decrease in the Φ_T values has been reported for Pcs linked to MNPs and this was attributed to the effects of spacer length [66]. In this work, Φ_T values increase in all cases for MNPs containing conjugates, again showing the importance of mixed NPs conjugation. τ_T determined from the transient curve **Fig. 4.2**, generally decreased with increase in triplet quantum yields. The lengthening of the lifetimes with increase in triplet quantum yields in some cases could be due to the protection afforded to the Pc by the NPs.

Of the InPcs alone complex **4** gave a larger Φ_T than **3** and a corresponding low triplet lifetime. The larger Φ_T of the latter could be due to the presence of S (slightly heavier than O and N) which will add an additional heavy atom effect encouraging intersystem crossing to the triplet state. The triplet quantum yields and lifetimes for complexes **5**, **6** and their conjugates could not be determined due to the azomethine group being closer to the phthalocyanine macrocycle, this

is reported to quench the triplet state [128] resulting in weak signals for **5**, **6** and their conjugates.

4.3 Singlet oxygen (Φ_Δ) quantum yield.

Singlet oxygen quantum yield Φ_Δ of Pc complexes and their conjugates was determined using equation **1.4** using unsubstituted ZnPc as a standard Φ_Δ= 0.67 in DMSO [105]. Φ_Δ values were determined under ambient conditions using DPBF as a singlet oxygen quencher. The concentration of DPBF was lowered to ~ 3 × 10^{-5} mol dm^{-3} for all solutions, to avoid chain reactions. DPBF degradation was spectroscopically monitored at ~ 417 nm at predetermined time intervals, **Fig. 4.3**. The intensity of the Q band did not change during the irradiation, confirming the stability of the Pc while DPBF degraded with increasing illumination time indicating the production of singlet oxygen.

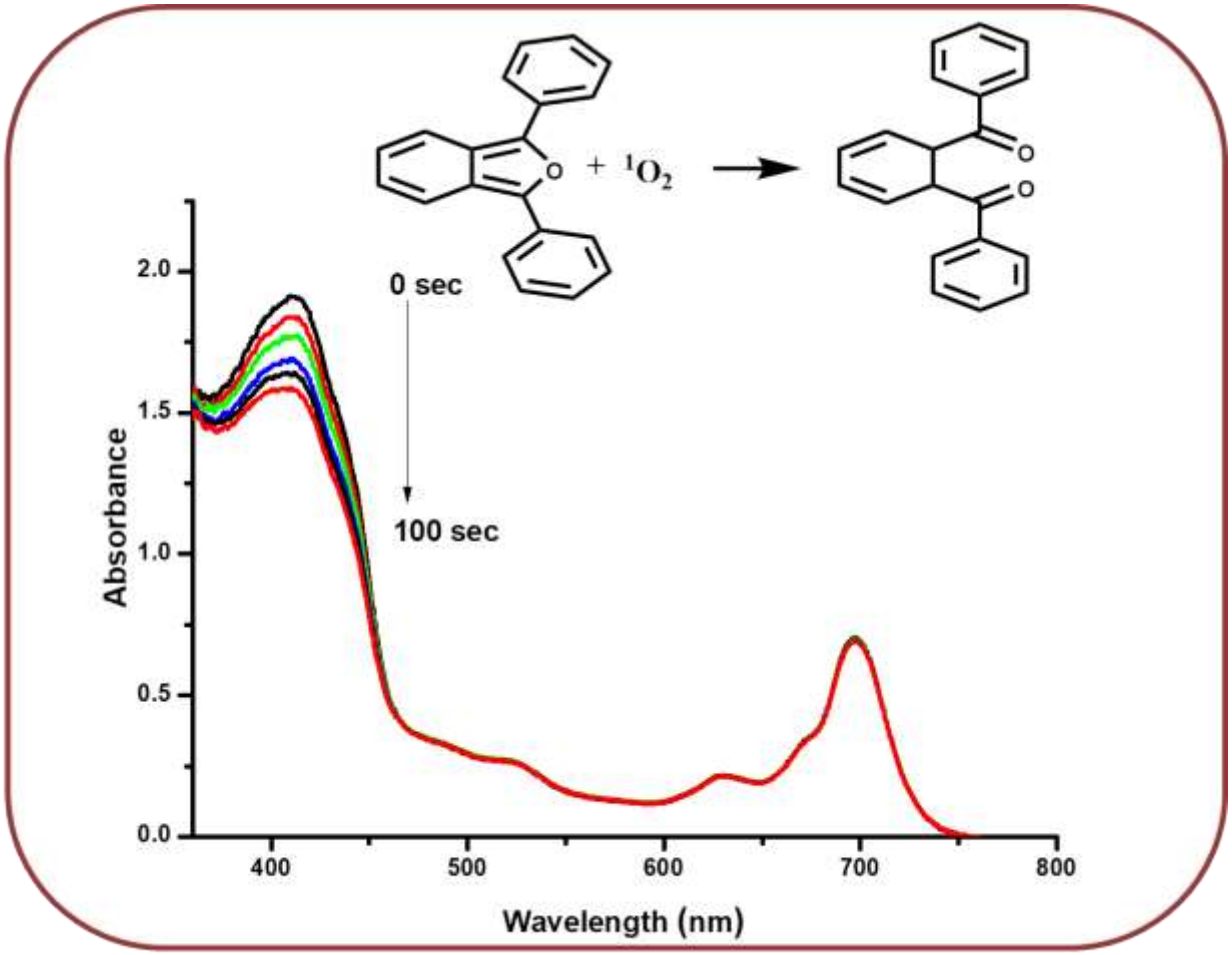

Fig. 4.3: Degradation of 1, 3-diphenylisobenzofuran (DPBF) in the presence of complex 4.

Φ_{Δ} values are expected to augment with increasing triplet quantum yields, since singlet oxygen is generated when ground state molecular oxygen interacts with the excited triplet state of phthalocyanine. However, this is not the case in **Table 4.1**. Complex **4** has the largest Φ_{Δ} corresponding to Φ_T. The Φ_{Δ} values obtained for **6** and **5**, are very low in **Table 4.1**, hence there was no triplet signal as explained above. Singlet oxygen quantum yields for complex **1** remained the same or decreased in the presence of the NPs. **2**-Ag@Fe_3O_4–SiNPs-APTES and **2**-SiNPs-APTES showed an increase in singlet oxygen quantum yield compared

to **2** alone. The rest of the conjugates of complex **2** showed insignificant change. There are increases in Φ_Δ values for **3**, **4** and **5** in the presence of NPs. For **6** there is an increase only for **6**-Ag@Fe_3O_4 NPs and not for **6**-Ag-Fe_3O_4 NPs. The increases are a result of the heavy atom effect of the NPs. The lack of increase in singlet oxygen quantum yield following conjugation could probably be due to the screening effect caused by the NPs, which could have prevented the interaction of the excited triplet state of the conjugates and the ground state molecular oxygen [129]. Even though the values decrease, the conjugates can still be used for PACT since complexes such as lutetium texaphyrin with a low singlet oxygen value of 0.11 have been employed for clinical application in PDT (similar in action to PACT) [130].

4.4 Summary of chapter

The photophysicochemical properties of metallophthalocyanine asymmetrical **1**, **2** and symmetrical **3**-**6** were studied alone and when conjugated to nanomaterials. There was improvement in the triplet quantum yield of the conjugates as compared to the metallophthalocyanines alone. However some of the conjugates did not show improvement in Φ_Δ compared to the metallocyanines alone, this is due to the screening effect caused by the NPs, which could have prevented the interaction of the excited triplet state of the conjugates and the ground state molecular oxygen.

Chapter 5
Photodynamic Antimicrobial Chemotherapy

5.1 Photodynamic Antimicrobial Chemotherapy.

Complex **4** and its conjugates were employed for the bacterial studies because of the high singlet oxygen quantum yields which is ideal for PACT. Charged photosensitisers are known to be more effective against bacteria inactivation [77,78] hence complex **4** and its conjugates are studied and for comparison purposes complex **3** and its conjugates were also studied even though there is no charge. The photodynamic antimicrobial chemotherapy of *E-coli* with complexes **3** and **4** in 5% DMSO/PBS was carried out at a constant concentration of 50 mg/L at varied irradiation time (see **Fig. 5.1A** and **5.1B**). The effect of 5% DMSO/PBS was studied as well (see **Fig. A6**), and there was no effect on percentage reduction of bacteria when irradiated. The log reduction values were determined using equation 5.1 and 5.2.

Cell studies definitions

$$\text{Percentage reduction: } \frac{(A-B) \times 100}{A} \qquad \textbf{(5.1)}$$

$$\text{Log reduction} = \log(A) - \log(B) \qquad \textbf{(5.2)}$$

Where A is the number of viable microorganisms before treatment and B is the number after treatment

Large percentage reduction indicates significant reduction in the bacterial growth which can be further shown with high log reduction value. Accepted log reduction values for applicability in PACT start from log reduction values >3 [131]. A log reduction of 1.64 (**Table 5.1**) was obtained after 120 min

irradiation for complex **4** in DMSO/PBS (and 1.52 in PBS only), this value was significantly higher when compared to the log reduction 0.42 of complex **3** in DMSO/PBS, this is probably due to the neutral nature and poor solubility of **3** in aqueous media. When comparing the log reductions of 8.31 for **4**-Ag-Fe_3O_4 NPs and 7.80 for **4**-Ag@Fe_3O_4 NPs to that of complex **4** alone shows the effect of charge and increase in Φ_Δ for the conjugates. However there was no a significant increase in log reduction values for the conjugates of complex **3**, (**Table 5.1**). **3**-Ag@Fe_3O_4 NPs had a log reduction value of 0.52 which is slightly higher when compared to **3**. The reason for this major difference in log reductions between the conjugates of complexes **3** and **4** is the result of the ability of complex **4** to electrostatically interact with the membrane of the bacteria cell wall due to its zwitter ionic nature. Once this happens the nanoparticles are able to break into the membrane which results in greater antibacterial activity, hence higher log reductions were obtained for the conjugates of complex **4**. **Fig 5.1B** shows that there was a slight increase in the inactivation of *E-coli* (in the dark) for **4**-Ag@Fe_3O_4 NPs and **4**-Ag-Fe_3O_4 NPs, compared to complex **4** alone.

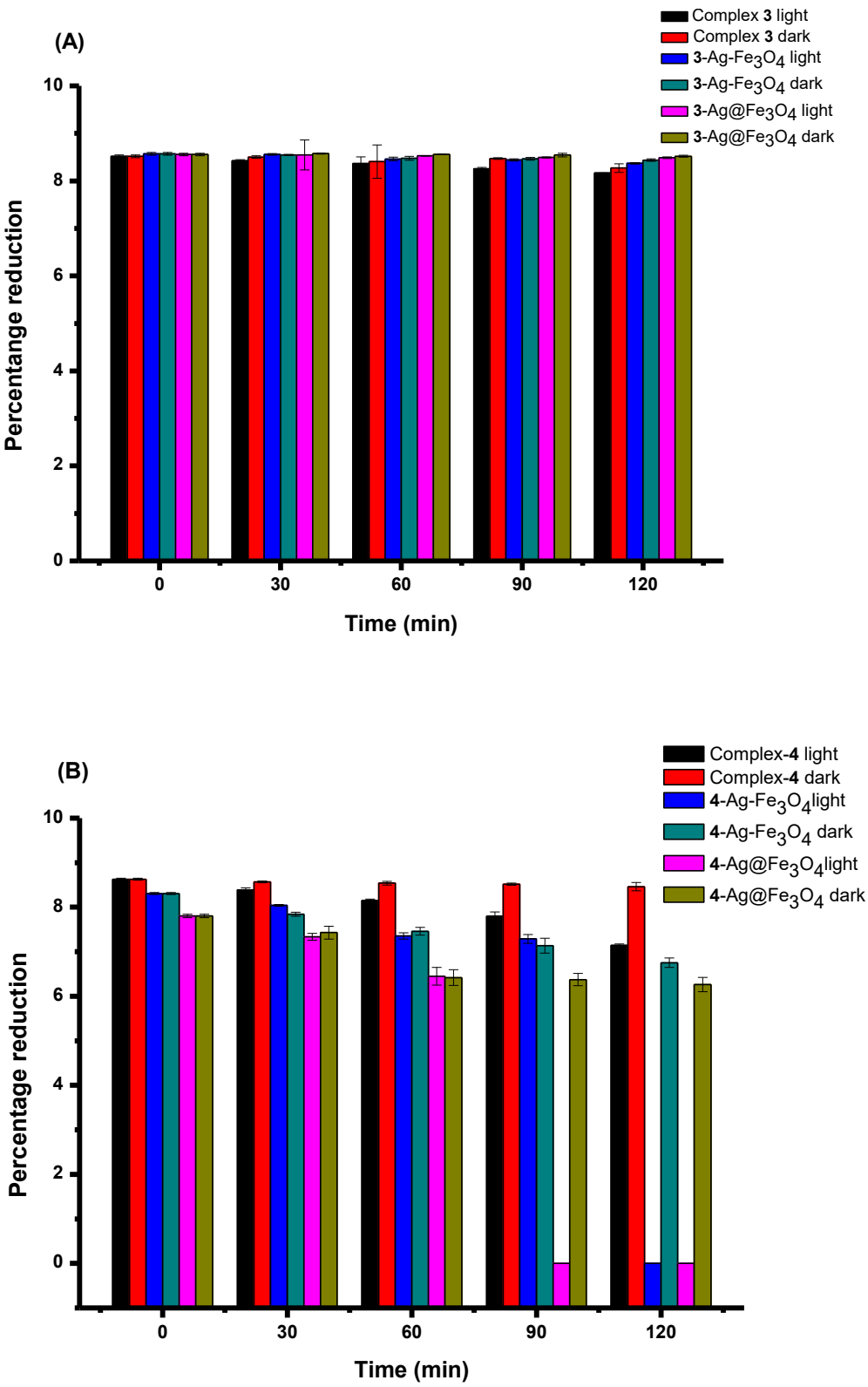

Fig. 5.1 Percentage reduction due to **3** (A) and **4** (B) alone and in the presence of NPs against *E. coli* in PBS/DMSO. Concentration = 50mg/L.

Table 5.1: Log reduction values for photoinactivation effect on E. coli at 50 mg/L at 120 min irradiation.

Complex	Solvent	Log reduction
Control	DMSO/PBS	0.11
4	PBS	1.52
4	DMSO/PBS	1.64
3	DMSO/PBS	0.42
3-Ag@Fe_3O_4	DMSO/PBS	0.52
3-Ag-Fe_3O_4	DMSO/PBS	0.13
4-Ag@Fe_3O_4	DMSO/PBS	7.80
4-Ag-Fe_3O_4	DMSO/PBS	8.31

5.2 Summary of chapter

Complex **4** and unquaternized derivative **3** when alone or linked to NPs were investigated. Complex **4** and its conjugates gave better singlet oxygen quantum yield values hence were used for PACT against gram negative (*E. coli*) and compared to complex **3**. Complex **4** and its conjugates, **4**-Ag@Fe_3O_4 NPs and **4**-Ag-Fe_3O_4 NPs gave higher log reduction 1.52, 7.80 and 8.31, respectively, due to their zwitterionic nature and high singlet oxygen quantum yield. Complex **3** and its conjugates **3**-Ag@Fe_3O_4 NPs and **3**-Ag-Fe_3O_4 NPs had low log reduction compared to **4** and its conjugates. These low log reductions were attributed to the lack of electrostatic interactions with the membrane of the bacteria cell wall. The results in this work show that the combined effects, the formation of singlet oxygen and the interaction with the membrane are of great significance in PACT.

Chapter 6
General conclusion

6.1 General conclusions

The syntheses and characterisation of asymmetric Zn mono caffeic acid tri–*tert*–butyl (**1**) and symmetrical tetrakis phenoxy *N,N*-dimethyl-4-(methylimino) indium (III) chloride (**3**), tetrakis phenoxy *N, N*-dimethyl-(3-sulfopropyl) ammonium) propyl]-4-(methylimino) indium (III) chloride (**4**), tetrakis *N,N*-dimethyl-4-(methylimino) indium(III) chloride (**5**) and tetrakis *N,N*-dimethyl-(3-sulfopropyl)ammonium) propyl]4-(methylimino) indium (III) chloride (**6**) phthalocyanines was successfully carried out. The effects of the different nanoparticles on the photophysical properties of metallophthalocyanines are studied. This work reports for the first time on the study of zwitterionic MPcs linked to silver-iron bimetallic nanoparticles. The morphology and sizes of the nanomaterials and their conjugates were determined using EDX, TEM and XRD. There was improvement in the triplet and singlet oxygen quantum yields of the conjugates as compared to the metallophthalocyanines alone in most cases. This work evaluates the photodynamic antimicrobial chemotherapy (using *E. coli*) using complexes **3** and **4** and their conjugates. The results in this work show that the combined effect (the formation of singlet oxygen and the interaction with the membrane) is of great significance in PACT.

6.2 Future work

The zwitterionic complex that is synthesised in this work shows great potential for photodynamic antimicrobial chemotherapy when linked with nanoparticles. Efforts will be made to synthesise both asymmetric and

symmetric zwitterionic phthalocyanines and link them to other nanomaterials.

References

[1] D.O. Oluwole, S.L. Manoto, R. Malabi, C. Maphanga, S. Ombinda-lemboumba, P. Mthunzikufa, T. Nyokong, Dye. Pigment. 150 (2018) 139–150.

[2] N. Masilela, T. Nyokong, J. Photochem. Photobiol. A Chem. 223 (2011) 124–131.

[3] S.M. Abdelghany, D. Schmid, J. Deacon, J. Jaworski, F. Fay, K.M. Mclaughlin, J.A. Gormley, J.F. Burrows, D.B. Longley, R.F. Donnelly, C.J. Scott, Biomacromolecules 14 (2013) 302–310.

[4] L. Lo, G.J. Hutchings, S. Cheng, C. Lee, C. Yang, F. Tseng, C. Mou, J. Mater. Chem. 19 (2009) 1193–1340.

[5] Y. Chin, S.H. Lim, Y. Zorlu, V. Ahsen, L.V. Kiew, L.Y. Chung, PLoS One 9 (2014) 1–11.

[6] H.K. Moon, M. Son, J.E. Park, S.M. Yoon, S.H. Lee, H.C. Choi, NPG Asia Mater. 4 (2012) doi:10.1038/am.2012.22 (1-8).

[7] R. Li, B. Liu, J. Gao, Cancer Lett. 386 (2017) 123–130.

[8] P. Sharma, S. Brown, G. Walter, S. Santra, B. Moudgil, Adv. Colloid Interface.Sci. 126 (2006) 471–485.

[9] C. Huang, H. Chang, Angew. Chemie - Int. Ed. 46 (2007) 6824–6828.

[10] O.L. Stroyuk, J. Theor. Exp. Chem. 41 (2014) 67–91.

[11] N.F. Steinmetz, Nanomed. Nanotechnol. 6 (2010) 634–641.

[12] M. Tintoré, S. Mazzini, L. Polito, M. Marelli, A. Latorre, Á. Somoza, A. Aviñó, C. Fàbrega, R. Eritja, Int. J. Mol. Sci. 16 (2015) 27625–27639.

[13] L.A. Lane, X. Qian, S. Nie, Chem. Rev. 115 (2015) 10489–10529.

[14] U. Drechsler, B. Erdogan, V.M. Rotello, Chem. Eur. J. 10 (2004) 5570–5579.

[15] M. Samim, C.K. Prashant, A.K. Dinda, A.N. Maitra, I. Arora, Int. J. Nanomedicine 6 (2011) 1825–1831.

[16] S.R. Mudshinge, A.B. Deore, S. Patil, C.M. Bhalgat, Saudi Pharm. J. 19 (2011) 129–141.

[17] G. Bisker, J. Dong, H.D. Park, N.M. Iverson, J. Ahn, J.T. Nelson, M.P. Landry, S. Kruss, M.S. Strano, Nat. Commun. 7 (2016) 10241–10255.

[18] Y. Tauran, A. Brioude, A.W. Coleman, M. Rhimi, B. Kim, Y. Tauran, A. Brioude, A.W. Coleman, World J. Biol. Chem. 4 (2013) 35–64.

[19] C.S. Mahon, C.J. Mcgurk, S.M.D. Watson, M.A. Fascione, C. Sakonsinsiri, W.B. Turnbull, D.A. Fulton, Angew. Chemie - Int. Ed. 56 (2017) 12913–12918.

[20] S. Xuan, F. Wang, J.M.Y. Lai, K.W.Y. Sham, Y.X.J. Wang, S.F. Lee, J.C. Yu, C.H.K. Cheng, K.C.F. Leung, ACS Appl. Mater. Interfaces 3 (2011) 237–244.

[21] L. Wei, J. Lu, H. Xu, A. Patel, Z.S. Chen, G. Chen, Drug Discov. Today

20 (2015) 595–601.

[22] R.A. Revia, M. Zhang, Mater. Today 19 (2016) 157–168.

[23] E. Calì, J. Qi, O. Preedy, S. Chen, D. Boldrin, W.R. Branford, L. Vandeperre, M.P. Ryan, J. Mater. Chem. A 6 (2018) 3063–3073.

[24] J. Kudr, Y. Haddad, L. Richtera, Z. Heger, M. Cernak, V. Adam, O. Zitka, Nanomaterials 7 (2017) doi:10.3390/nano7090243.

[25] J. Bhaumik, A.K. Mittal, A. Banerjee, Y. Chisti, U.C. Banerjee, Nano Res. 8 (2015) 1373–1394.

[26] J.W. Yoo, Arch. Pharm. Res. 35 (2012) DOI 10.1007/s12272-012-0100-4 (1-2).

[27] C.A. Kruger, H. Abrahamse, Molecules 23 (2018) doi:10.3390/molecules23102628 (4-21).

[28] E.P. Ortiz, J.H.R. Ruiz, E.A.H. Marquez, J.L. Esparza, A.D. Cornejo, J.C.C. Gonzales, L.F.E. Cristobal, S.Y.R. Lopez, J. Nanomater. 2017 (2017) doi.org/10.1155/2017/4752314 (1-9).

[29] I. Maliszewska, Z. Sadowski, J. Phys. 146 (2016) doi:10.1088/1742-6596/146/1/012024 (1-6).

[30] L.G. Thompson, W.J. Thomson, Prepr. Symp. 28 (1983) 220–227.

[31] M. Chang, W. Lin, W. Xiao, Y. Chen, Materials (Basel). 11 (2018) doi:10.3390/ma11050659 (1-8).

[32] U. Kurtan, A. Guner, M.D. Amir, A. Baykal, Bull. Mater. Sci. 40 (2017) 147–155.

[33] K. Hayashi, M. Nakamura, H. Miki, S. Ozaki, M. Abe, T. Matsumoto, T. Kori, K. Ishimura, Adv. Funct. Mater. 24 (2014) 503–513.

[34] K.K. Ng, G. Zheng, Chem. Rev. 115 (2015) 11012–11042.

[35] S. Tombe, W. Chidawanyika, E. Antunes, G. Priniotakis, P. Westbroek, T. Nyokong, J. Photochem. Photobiol. A Chem. 240 (2012) 50–58.

[36] J. Suchánek, K. Lang, V. Novakova, P. Zimcik, Z. Zelinger, P. Kubát, Photochem. Photobiol. Sci. 12 (2013) 743–750.

[37] S. Kwon, R.K. Singh, R.A. Perez, E.A.A. Neel, H.W. Kim, W. Chrzanowski, J. Tissue Eng. 4 (2013) DOI: 10.1177/2041731413503357 (1-18).

[38] M.N. Seleem, P. Munusamy, A. Ranjan, H. Alqublan, G. Pickrell, N. Sriranganathan, Antimicrob. Agents Chemother. 53 (2009) 4270–4274.

[39] Y. Castro, N.I. Vazquez, Z. Gonzalez, Bol. Soc. Esp. Ceram V. J. 56 (2017) 139–145.

[40] I.A. Rahman, P. Vejayakumaran, C.S. Sipaut, J. Ismail, C.K. Chee, Mater. Chem. Phys. 114 (2009) 328–332.

[41] J. Zhu, Z. Ko´nya, V.F. Puntes, I. Kiricsi, C. X. Miao,J. W. Ager, A. P.livisatos, G.A. Somorjai. Langmuir.19 (2003) 4396-4401.

[42] F. Caruso, M.Spasova, V. S. Maceira, L.M. Liz-Marzµn.Adv.Mater 13

(2001) 1090–1094.

[43] I. Roy, T.Y. Ohulchanskyy, H.E. Pudavar, E.J. Bergey, A.R. Oseroff, J. Morgan, T.J. Dougherty, P.N. Prasad, J. Am. Chem. Soc. 125 (2003) 7860–7865.

[44] N.Z. Knezevic, E. Ruiz-Hernandez, W.E. Hennink, M. Vallet-Regı, RSC Adv. 3 (2013) 9584–9593.

[45] R. Tietze, J. Zaloga, H. Unterweger, S. Lyer, R.P. Friedrich, C. Janko, M. Pöttler, S. Dürr, C. Alexiou, Biochem. Biophys. Res. Commun. 468 (2015) 463–470.

[46] J. Neamtu, N. Verga, Dig. J. Nanomater. Biostruct. 6 (2011) 969–978.

[47] E. Dube, D.O. Oluwole, T. Nyokong, J. Lumin. 190 (2017) 353–363.

[48] T. Nyokong, J. Pure Appl. Chem. 83 (2011) 1763–1779.

[49] G.T. Byrn, R.P. Linstead, A.R. Lowe, J. Chem. Soc. (1934) 1017–1022.

[50] P.A. Barret, C.E. Dent, R.P. Linstead, J. Chem. Soc. (1936) 1719–1736.

[51] E.N. Durantini, I. Scalise, Bioorg. Med. Chem. 13 (2005) 3037–3045.

[52] C.M.B. Carvalho, J.P.C. Tomé, M.A.F. Faustino, G.P.M.S. Maria, A.C. Tomé, J.A.S. Cavaleiro, L. Costa, E. Alves, J. Porphyr. Phthalocyanines 13 (2009) 574–577.

[53] V.N. Nemykin, S. V. Dudkin, F. Dumoulin, C. Hirel, A.G. Gürek, V. Ahsen, Arkivoc 2014 (2014) 142–204.

[54] D. Gu, Q. Chen, X. Tang, F. Gan, S. Shen, K. Liu, H. Xu, Opt. Commun. 121 (1995) 125–129.

[55] D.S. Cells, J. Cid, J. Yum, S. Jang, M.K. Nazeeruddin, E. Martínez-ferrero, E. Palomares, J. Ko, M. Grätzel, Angew. Chemie - Int. Ed. 119 (2007) 8510–8514.

[56] B.I. Kharisov, U.O. Me´ndez, J.L. Garza, J.R.A. Rodrı´guez, New J. Chem. 29 (2005) 686–692.

[57] K. Cheng, J.B. Lv, J.Z. Ma, J.H. Hu, C. Chen, K. Zeng, G. Yang, Express Polym. Lett. Polym. Lett. 11 (2017) 924–934.

[58] P. Humberstone, G.J. Clarkson, N.B. McKeown, K.E. Treacher, J. Mater. Chem. 6 (1996) 315–322.

[59] G.J. Clarkson, N.B. McKeown, K.E. Treacher, J. Chem. Soc. Perkin Trans. 1 (1995) 1817–1823.

[60] M. Drobizhev, N.S. Makarov, A. Rebane, H. Wolleb, H. Spahni, J. Lumin. 128 (2008) 217–222.

[61] N. Nombona, W. Chidawanyika, T. Nyokong, Polyhedron 30 (2011) 654–659.

[62] Y. Liu, X. Yu, D. Zhu, Thin Solid Films 244 (1994) 943–946.

[63] S. Peteni, T. Nyokong, Inorg. Chim. Acta 482 (2018) 431–437.

[64] G. Singh, P.K. Khatri, K. Ganguly, S.L. Jain, RSC Adv. 4 (2014) 29124–29130.

[65] O.M. Bankole, T. Nyokong, New J. Chem. 40 (2016) 10016–10027.

[66] O.L. Osifeko, I. Uddin, P.N. Mashazi, T. Nyokong, New J. Chem. 40 (2016) 2710–2721.

[67] P. Khoza, T. Nyokong, J. Mol. Catal. A. Chem. 395 (2014) 34–41.

[68] E. Dube, N. Nwaji, D.O. Oluwole, J. Mack, T. Nyokong, J. Photochem. Photobiol. A Chem. 349 (2017) 148–161.

[69] N. Nwaji, B. Jones, J. Mack, D.O. Oluwole, T. Nyokong, J. Photochem. Photobiol. A Chem. 346 (2017) 46–59.

[70] N. Rapulenyane, E. Antunes, T. Nyokong, New J. Chem. 37 (2013) 1216–1223.

[71] K. Sanusi, J.M. Stone, T. Nyokong, New J. Chem. 39 (2015) 1665–1677.

[72] S.V. Rao, P.T. Anusha, L. Giribabu, Pranama J. Phys. 75 (2010) 1017–1023.

[73] T. Maisch, R. Szeimies, C. Abels, Photochem. Photobiol. Sci. 3 (2004) 907–917.

[74] M.S. Baptista, M. Wainwright, Brazilian J. Med. Biol. Res. 44 (2011) 1–10.

[75] M. Wainwright, J. Antimicrob. Chemother. 42 (1998) 13–28.

[76] A.S. Garcez, M.S. Ribeiro, G.P. Tegos, S.C. Núñez, A.O.C. Jorge, M.R.

Hamblin, Lasers Surg. Med. 39 (2007) 59–66.

[77] V. Mantareva, V. Kussovski, I. Angelov, E. Borisova, L. Avramov, Bioorg. Med. Chem. 15 (2007) 4829–4835.

[78] V. Mantareva, I. Angelov, V. Kussovski, R. Dimitrov, L. Lapok, D. Wöhrle, Eur. J. Med. Chem. 46 (2011) 4430–4440.

[79] S. Huo, Y. Jiang, A. Gupta, Z. Jiang, R.F. Landis, S. Hou, X. Liang, V.M. Rotello, ACS Nano 10 (2016) 8732–8737.

[80] S. Çolak, M. Durmuş, S.Z. Yıldız, Dalt. Trans. 45 (2016) 10402–10410.

[81] G. Cheng, Z. Zhang, S. Chen, J.D. Bryers, S. Jiang, Biomaterials 28 (2007) 4192–4199.

[82] P. Matlaba, T. Nyokong, Polyhedron 21 (2002) 2463–2472.

[83] T.M. Mohan, B.N.Ã. Achar, J. Phys. Chem. Solids 67 (2006) 2282–2288.

[84] L. Edwards, D.H. Dolphin, J. Mol. Spectrosc. 35 (1970) 90–109.

[85] C.G. Claessens, U.W.E. Hahn, T. Torres, Chem. Rec. 8 (2010) 75–97.

[86] C.M. Cassidy, R.F. Donnelly, J.S. Elborn, N.D. Magee, M.M. Tunney, J. Photochem. Photobiol. B Biol. 106 (2012) 95–100.

[87] M.S. Costa, E. Munin, L.M. Giroldo, L. Proco, J. Photochem. Photobiol. B Biol. 88 (2007) 16–20.

[88] M. Li, B. Mai, A. Wang, Y. Gao, X. Wang, X. Liu, RSC Adv. 7 (2017)

40734–40744.

[89] M.R. Hamblin, T. Hasan, Photochem. Photobiol. Sci. 3 (2004) 436–450.

[90] J. Li, Y. Shim, Clin Endosc 46 (2013) 7–23.

[91] W. Christian, M. Grabolle, J. Pauli, M. Spieles, U. Resch-genger, Anal. Chem. 83 (2011) 3431–3439.

[92] A. Ogunsipe, T. Nyokong, J. Photochem. Photobiol. A Chem. 173 (2005) 211–220.

[93] W. Chidawanyika, T. Nyokong, New J. Chem. 31 (2007) 377–384.

[94] N. Kobayashi, H. Konami, J. Porphyr. Phthalocyanines 5 (2001) 233–255.

[95] Z. Watkins, J. Taylor, S. D'Souza, J. Britton, T. Nyokong, J. Fluoresc. 25 (2015) 1417–1429.

[96] A. Gorman, J. Killoran, C.O. Shea, T. Kenna, W.M. Gallagher, D.F.O. Shea, J. Am. Chem. Soc. 126 (2004) 10619–10631.

[97] A. Ogunsipe, J. Chen, T. Nyokong, New J. Chem. 28 (2004) 822–827.

[98] S. Reindl, A. Penzkofer, Chem. Phys. 213 (1996) 429–438.

[99] L. De Boni, E. Piovesan, L. Gaffo, C.R. Mendonc, J. Phys. Chem. Lett. 112 (2008) 6803–6807.

[100] C. Desforge, C. Thiec, E. Nucleates, I.R.D. Desicp, D. Scm, C. Ua, Y. Cedex, S. Gaspard, I. De Chimie, J. Phys. Chem. 93 (1989) 1226–1233.

[101] N.A. Kuznetsova, N.S. Gretsova, V.M. Derkacheva, L. Oleg, E.A. Lukyanets, J. Porphyr. Phthalocyanines 7 (2003) 147–154.

[102] P.R. Ogilby, C.S. Foote, J. Am. Chem. Soc (1983) 3423–3430.

[103] T. Durmus, Mahmut, Vefa, Ahsen, Nyokong, J. Photochem. Photobiol. A Chem. 186 (2007) 323–329.

[104] A. Sindelo, O.L. Osifeko, T. Nyokong, Inorg. Chim. Acta 476 (2018) 68–76.

[105] N.A. Kuznetsova, N.S. Gretsova, O.A. Yuzhakova, V.M. Negrimovskii, O.L. Kaliya, Russ. J. Gen. Chem. 71 (2001) 36–41.

[106] N. Rapulenyane, E. Antunes, N. Masilela, T. Nyokong, J. Photochem. Photobiol. A Chem. 250 (2012) 18–24.

[107] G. Lopes, M. Vargas, S.K. Sharma, F. Be, K.R. Pirota, M. Knobel, C. Rettori, R.D. Zysler, J. Phys. Chem. C 114 (2010) 10148–10152.

[108] Z. Xu, Y. Hou, S. Sun, J. Am. Chem. Soc. 28 (2007) 8698–8699.

[109] A. Taglietti, Y.A.D. Fernandez, E. Amato, L. Cucca, G. Dacarro, P. Grisoli, V. Necchi, P. Pallavicini, L. Pasotti, M. Patrini, D. Chimica, C. Generale, U. Pavia, F.A. Volta, U. Pavia, V. Bassi, Langmuir 28 (2012) 8140–8148.

[110] H. Mader, X. Li, S. Saleh, M. Link, P. Kele, O.S. Wolfbeis, Ann. N.Y. Acad. Sci. 1130 (2008) 218–223.

[111] K. Sanusi, E.K. Amuhaya, T. Nyokong, J. Phys. Chem. C 118 (2014)

7057–7069.

[112] J. Britton, E. Antunes, T. Nyokong, J. Photochem. Photobiol. A Chem. 210 (2010) 1–7.

[113] D.O. Oluwole, J. Britton, P. Mashazi, T. Nyokong, Synth. Met. 205 (2015) 212–221.

[114] D.O. Oluwole, T. Nyokong, J. Photochem. Photobiol. A Chem. 312 (2015) 34–44.

[115] G.K. Karaoglan, G. Gümrükçü, A. Koca, A. Gül, Dye. Pigment. 88 (2011) 247–256.

[116] M.A. Hassan, A.M. Omer, E. Abbas, W.M.A. Baset, T.M. Tamer, Sci. Rep. 8 (2018) DOI:10.1038/s41598-018-29650-w.

[117] O.L. Osifeko, M. Durmus, T. Nyokong, J. Photochem. Photobiol. A Chem. 301 (2015) 47–54.

[118] V. Kussovski, V. Mantareva, I. Angelov, P. Orozova, E. Borisova, L. Avramov, Microbiol. Lett. 294 (2009) 133–140.

[119] M. Durmus, T. Nyokong, Inorg. Chem. Commun. 10 (2007) 332–338.

[120] B.C. Smith, CRC Press New York (1998).

[121] S. Peng, J.M. Mcmahon, G.C. Schatz, S.K. Gray, Y. Sun, PNAS 107 (2010) 14530–14534.

[122] A. V Zasedatelev, T. V Dubinina, D.M. Krichevsky, V.I. Krasovskii, V.Y.

Gak, V.E. Pushkarev, L.G. Tomilova, A.A. Chistyakov, J. Phys. Chem.C 120 (2016) 1816–1823.

[123] A.W. Snow, J.R. Griffith, Macromolecules 17 (1984) 1614–1624.

[124] M.J. Stillman, T. Nyokong, Eds. C. C. Leznoff B. Lever, VHC, New York (1989) 133–290.

[125] M.A.M. Khan, S. Kumar, M. Ahamed, S.A. Alrokayan, M.S. Alsalhi, M. Alhoshan, A.S. Aldwayyan, Appl. Surf. Sci. 257 (2011) 10607–10612.

[126] R. Prabakaran, R. Kesavamoorthy, G.L.N. Reddy, Phys. Stat. Sol. 229 (2002) 1175–1186.

[127] M.E.F. Brollo, R. López-Ruiz, D. Muraca, S.J.A. Figueroa, K.R. Pirota, M. Knobel, Sci. Rep. 4 (2014) 6839–6843.

[128] X. Zhang, Y. Di, F. Zhang, J. Photochem. Photobiol. A Chem. 203 (2009) 216–221.

[129] E.I. Sagun, E.I. Zenkevich, V.N. Knyukshto, A.M. Shulga, D.A. Starukhin, C. Von Borczyskowski, Chem. Phys. 275 (2002) 211–230.

[130] R. Bonnett, Gordon Breach Sci. Publ. Amsterdam (2000).

[131] D.P. Stevens, A. Surapaneni, R. Thodupunuri, N.A.O. Connor, D. Smith, Water Res. 125 (2017) 501–511.

Appendices

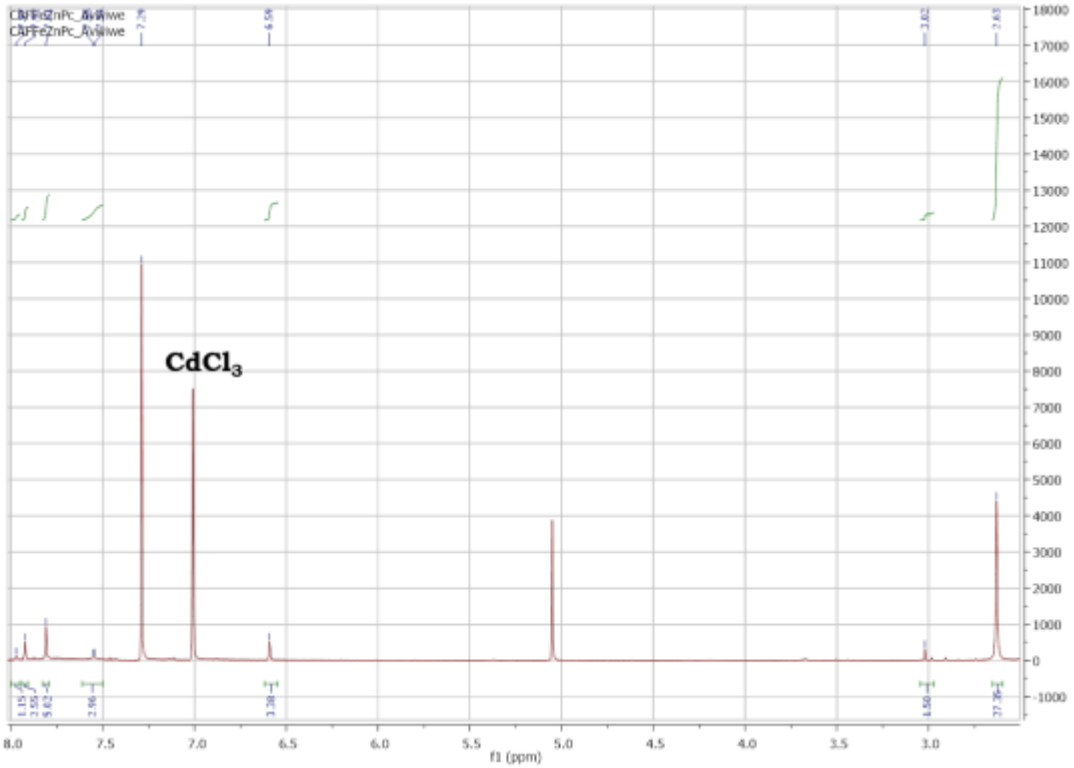

Figure A1: ^{1}H-NMR spectrum of complex-1 at 600MHz in $CDCl_3$.

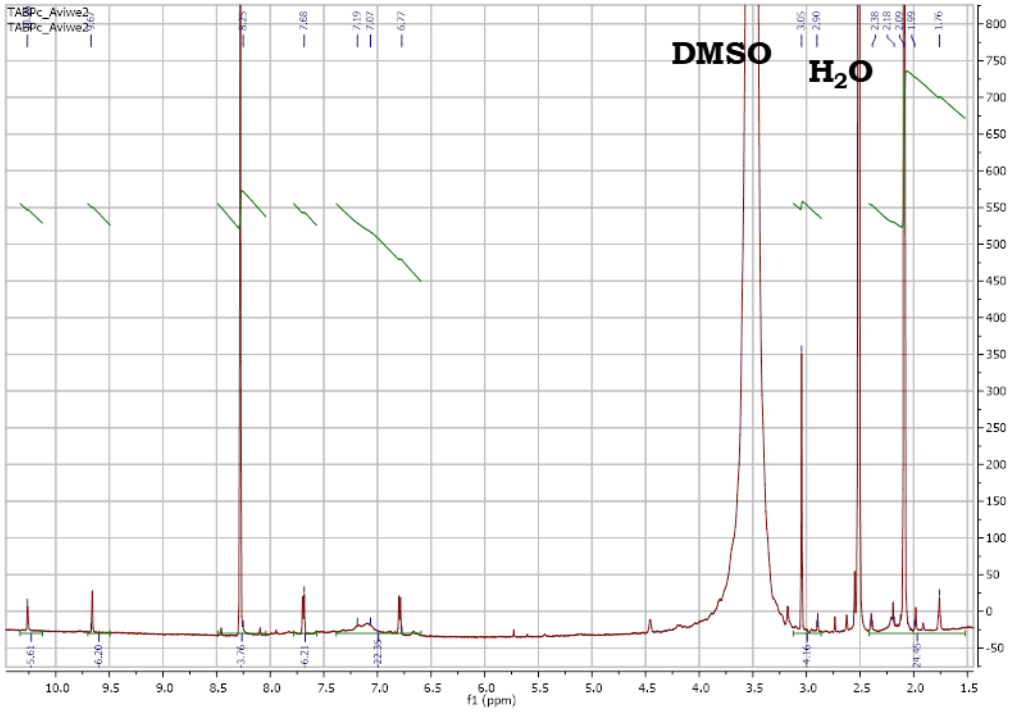

Figure A2: ^{1}H-NMR spectrum of complex-3 at 600MHz in DMSO-d$_6$.

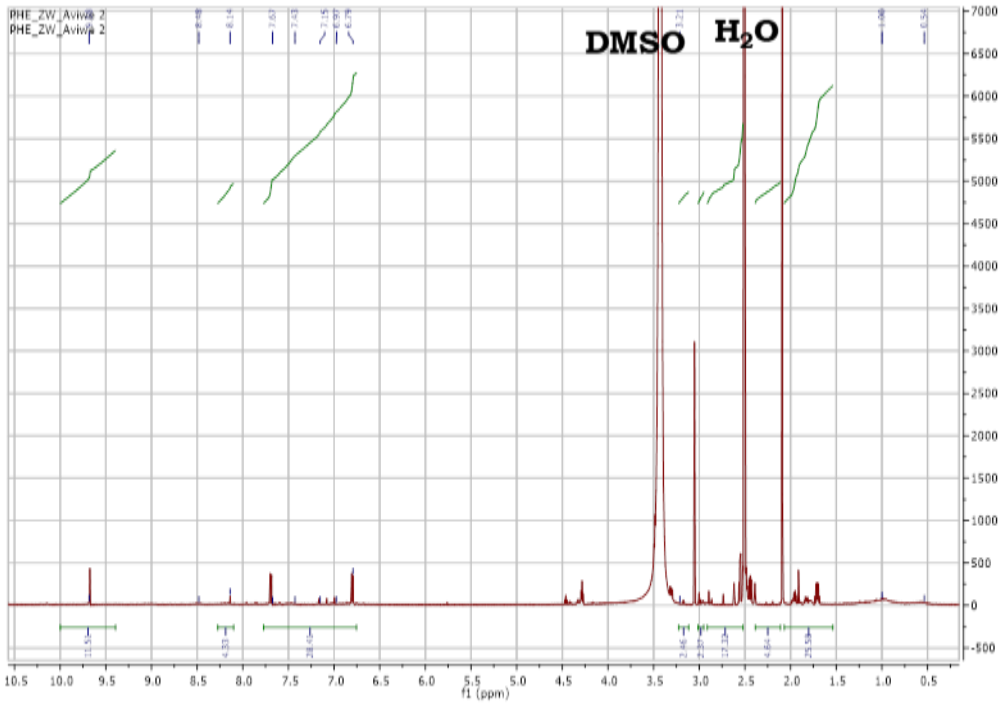

Figure A3: ^{1}H-NMR spectrum of complex-4 at 600MHz in DMSO-d$_6$.

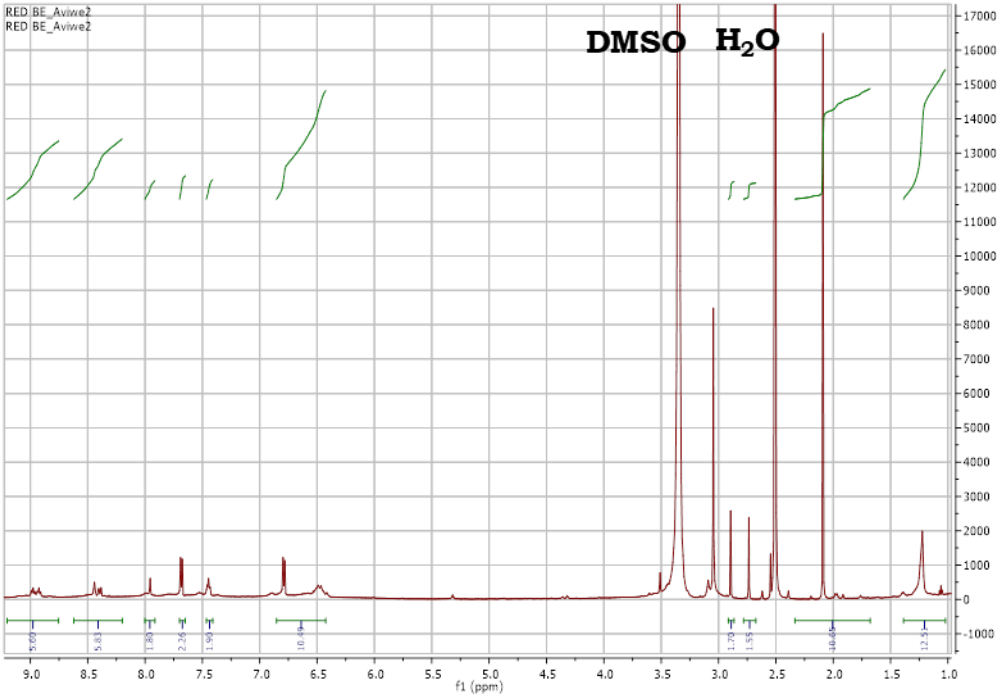

Figure A4: ^{1}H-NMR spectrum of complex-5 at 600MHz in DMSO-d_6

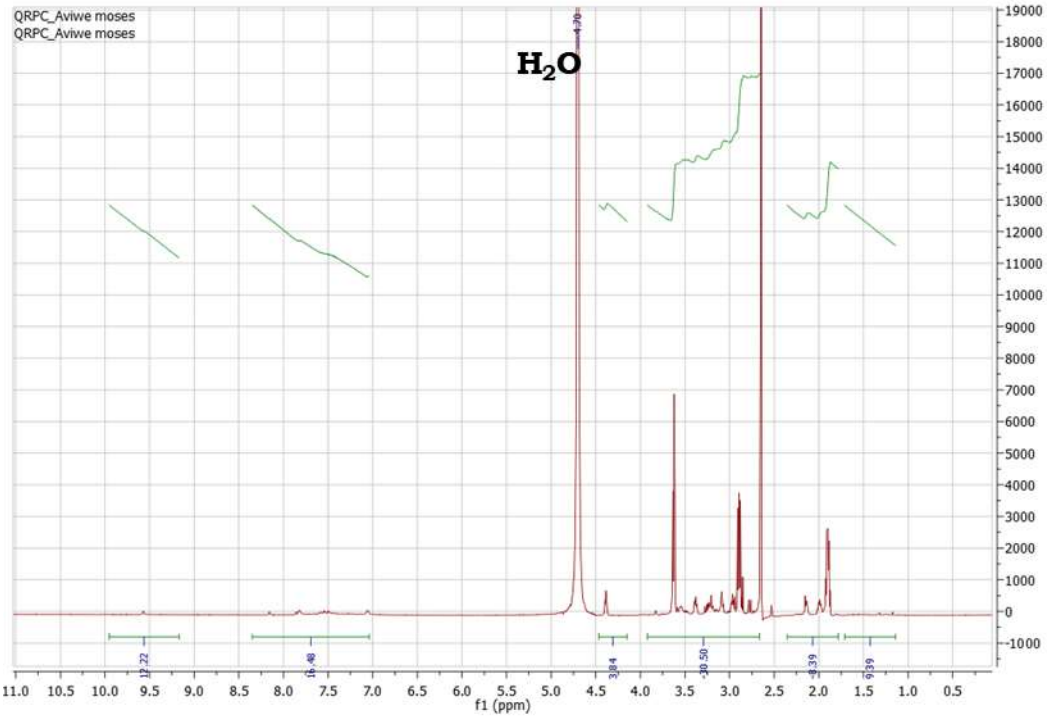

Figure A5: ^{1}H-NMR spectrum of complex-6 at 600MHz in D_2O.

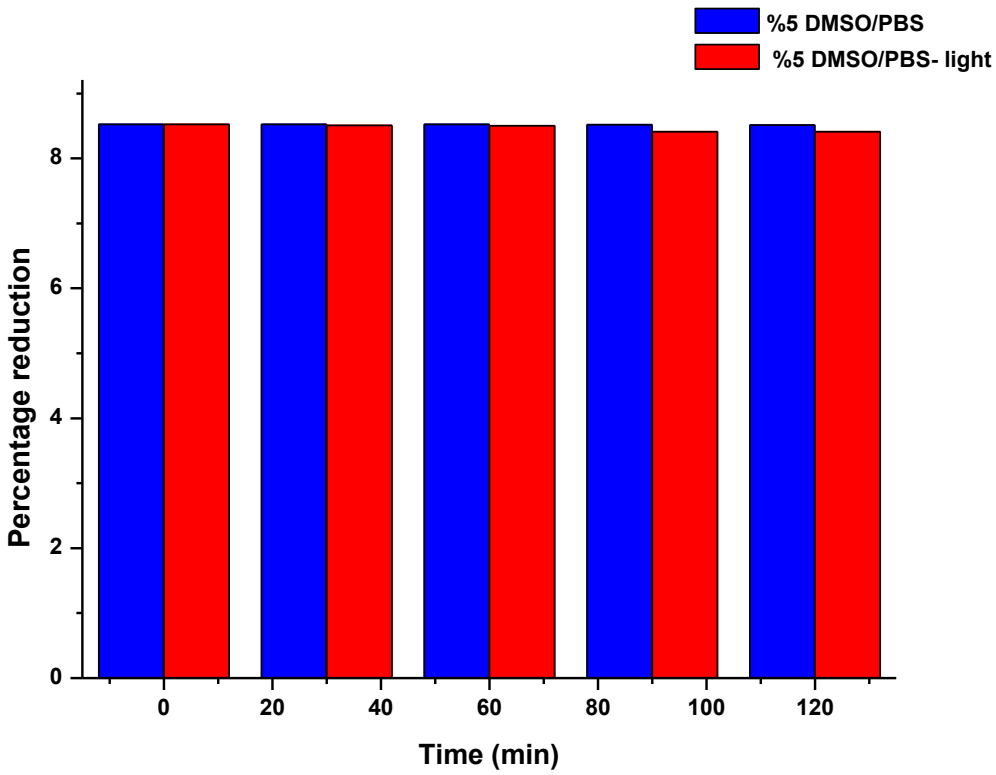

Figure A6: Percentage reduction due to 5% DMSO/PBS alone in the presence of *E. coli*